Università degli Studi di Pavia
Dottorato di Ricerca in Fisica – XXXI Ciclo

Development of an innovative photodetector for liquid argon applications: the SiPMs Single Channel Array

Tommaso Cervi

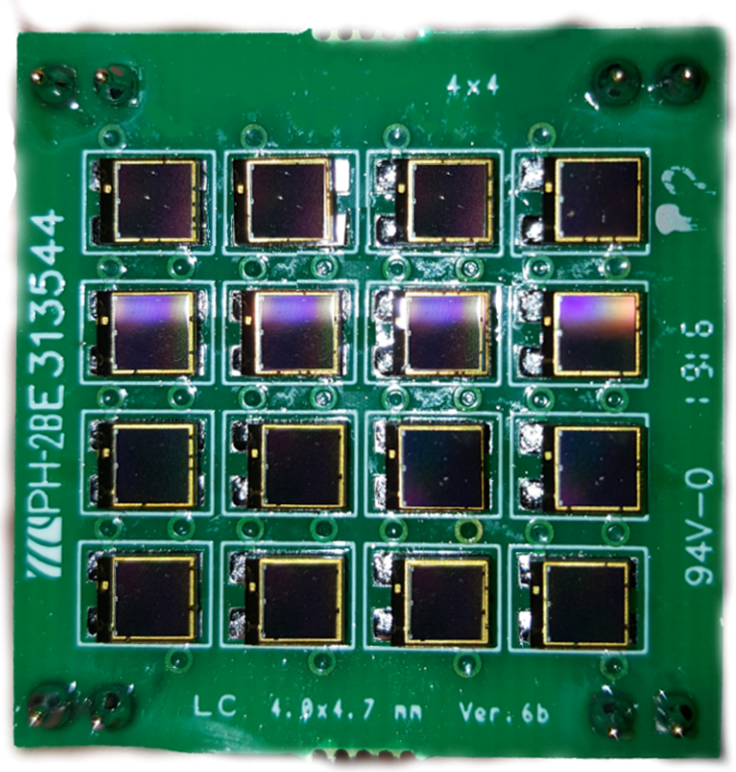

Tesi per il conseguimento del titolo

Full title:

Development of an innovative photodetector for liquid argon applications: the SiPMs Single Channel Array

Short title for the side if necessary:

Development of an innovative photodetector for liquid argon applications: the SiPMs Single Channel Array

Tommaso Cervi

2019

UNIVERSITY OF PAVIA
Department of Physics

Graduate course in Physics

Development of an innovative photodetector for liquid argon applications: the SiPMs Single Channel Array

Doctoral Thesis of

Dott. Tommaso Cervi

Supervisor: Prof. A. Menegolli

Dottorato di Ricerca in Fisica XXXI Ciclo

Contents

Table of contents **iv**

List of Figures **v**

Introduction **1**

1 Liquid Argon Time Projection chambers for neutrino experiments **1**
1.1 Neutrino physics 1
1.2 History of LAr-TPCs 3
1.3 LAr-TPC operational principles 5
1.3.1 Liquid argon properties 6
1.3.2 Ionization in liquid argon 7
1.3.3 Light production in liquid argon 9
1.4 A LAr-TPC photon detection system: the ICARUS T600 case . 11
1.4.1 Wavelength shifter deposition 13
1.4.2 PMT performance in LAr 16
1.4.3 Trigger and data acquisition system 17
1.5 Future projects 19
1.5.1 The DUNE experiment 20

2 Silicon Photomultipliers **25**
2.1 SiPM working principles 25
2.1.1 A bit of history 25
2.1.2 Semiconductor photodetectors 27
2.1.3 Avalanche photodiodes 30
2.2 SiPM characteristics and performance 34
2.2.1 Breakdown voltage 34
2.2.2 Pulse shape 34
2.2.3 Gain 37
2.2.4 Photon detection efficiency 37
2.2.5 Noise 37

3 SiPM performances as a function of temperature **41**
3.1 Experimental apparatus 41
3.1.1 The cold head 41
3.1.2 The VUV absolute Quantum Efficiency measurement system 46
3.2 Test as a function of temperature 49
3.2.1 Breakdown voltage and quenching resistance as a function of temperature 49
3.2.2 Gain as a function of temperature 52
3.2.3 Noise 57
3.3 Other tests 61
3.3.1 Quantum efficiency in VUV 61
3.3.2 Radiation hardness 63
3.4 Summary of the results 67

4 SiPM array with common bias and readout **69**
4.1 Realization of SiPM test-array 69
4.1.1 Electrical configurations 70
4.2 Tests on performance 71
4.2.1 Preliminary test 72
4.3 First test in LAr-TPC 73
4.3.1 Experimental apparatus 73
4.3.2 Data taking and results 77
4.4 Increases of active surface and time features 82
4.4.1 The hybrid circuit 83
4.5 Additional test in liquid argon 87
4.5.1 Time features 87
4.5.2 Comparison between the SiPMs arrays and the ICARUS PMTs 88
4.5.3 Data taking and results 89

Conclusions **93**

Bibliography **97**

List of Figures

1.1 Illustration of the ICARUS T600 detector placed into the hall-B of the Laboratori Nazionali del Gran Sasso. 4
1.2 Track reconstruction in LAr-TPCs: electrons produced during the interaction generate an inducted signal on the first wires planes and are collected by the last plane. 5
1.3 Relation between Argon luminescence and collected charge. In the upper panel (a) the luminescence intensity L and the fraction of collected charge Q as function of the applied electric field are shown: the 100 values represent, respectively, the total light collected at zero field and the initially produced charge Q_0. In the lower panel (b) the linear relation between the detected light intensity and the lost charge $Q_0 - Q$ is shown, as function of the applied field. 8
1.4 Scintillation light intensity as a function of wavelenght (left) and emission time (right). 10
1.5 Scheme of the placement of the different detectors at Fermilab for the SBN experiment. 12
1.6 PMTs are usually placed behind the wires planes. 13
1.7 Scheme of the ICARUS LAr-TPC PMTs deployment. For each TPC there are 90 8-in. PMTs. 13
1.8 Photo and scheme of the Hamamatsu R5912-mod. 15
1.9 Mechanical scheme of the evaporation system used for the ICARUS PMTs. 16
1.10 Gain measurements of different PMT models as a function of the bias voltage both at 300 K and 77 K. 17
1.11 Linearity of R5912 (top-left), R5912-02 (top-right) and 9357 KFLB (bottom) at room and at cryogenic temperature. 18
1.12 Dark count spectra for R5912 (top-left), R5912-02 (top-right) and ETL 9357 KFLB (bottom) at room and at cryogenic temperature. 18
1.13 Scheme of the far detector for the DUNE experiment. 21
1.14 Scheme of the ProtoDune LAr-TPC. 22

2.1 The first two silicon single photon detectors. Left is the planar type from Haitz and right the reach through type made by McIntyre [58]. 26
2.2 Structure of the detector developed in Japan in 1972. 26
2.3 Fermi energy level for p-type and n-type dopings. 28
2.4 Scheme of a photoconductor. 28
2.5 Scheme of the energy levels variations due to different dopings. . 29
2.6 Scheme of a pn structure for recombination. See text for details. 29
2.7 P-i-n structure of a photodiode. 30
2.8 Working principles of an avalanche photodiode. 31
2.9 Current density of an avalanche photodiode for electrons (a) and for both electrons and holes (b). 32
2.10 Gain of an avalanche photodiode as a function of depth for different value of the hole-electron density ratio. 33
2.11 Equivalent circuits of a SiPM. On the left, the APDs with the relative quenching resistors are shown. On the right a detailed view of the equivalent circuit of the APD is shown. 35
2.12 Detailed view of the equivalent circuit of a SiPM. 35
2.13 The three components of the PDE are shown: the quantum efficiency (a), the fill factor (b) and the P_{01} probability (c). See text for more details. 38

3.1 Photo of the cold head system placed at the INFN and University of Pavia laboratory. 42
3.2 Sketch of the cold head apparatus. Power supplies, data acquisition system and pulse generator are shown. 43
3.3 Photo of the final part of the cold head with the SiPM placement. In this case, an AdvanSiD $3 \times 3\ mm^2$ NUV is placed in a dedicated support (socket). Two screws allow to keep the device under test in the correct position. 44
3.4 Detailed view of the inner part of the system. The temperature sensors, the SiPM, the pre-amplificator and the copper cap needed to place the optical fiber in front of the SiPM active surface are shown. 45
3.5 Sketch of the apparatus vacuum system. 45
3.6 Scheme of the monochromator apparatus. In red the light trajectory from the lamp to the device under test or the reference photodiode is shown. 46
3.7 Spectrum of the intensity of the Deuterium lamp as a function of wavelength. 48
3.8 Current as a function of wavelength for the reference photodiode. The red line is a polynomial fit. 48
3.9 APD cells gain as a function of bias voltage at different temperatures for an AdvanSiD NUV SiPM model. 50

3.10 Breakdown voltage as a function of temperature for the Hamamatsu s13360 SiPM ($1 \times 1\ mm^2$). 51
3.11 Breakdown voltages as a function of temperature for the Hamamatsu s12572 (red) and AdvanSiD NUV (black) SiPMs models. Both these devices have an active area of $3 \times 3\ mm^2$. 51
3.12 I-V curve of a Hmamatsu s12572-050P at room temperature acquired with direct bias to measure the quenching resistance. . 53
3.13 Quenching resistance as a function of temperature for an Hmamatsu s12572-050P. 53
3.14 Charge spectrum obtained with the AdvanSiD ASD-NUV3S-P SiPM model of $3 \times 3\ mm^2$ of active area, with about 10 thousand recorded waveform at $T = 300\ K$. 54
3.15 Gain ratios of different SiPM models as a function of overvoltage. 56
3.16 Gain measured for different SiPM models as a function of overvoltage. All these results are compatibles with the data sheets specifications. 57
3.17 Scheme of p-on-n (left) and n-on-p (right) layers for a SiPM. . . 58
3.18 Scatter plot of the pulse amplitude as a function its distance from the preceding event at 7.2V over-voltage [69]. 59
3.19 Waveforms of a SiPM model recorded at the same overvoltage ($V_{ov} = 5\ V$) at different temperatures: 300 K (a) and 120 K (b). 60
3.20 Dark count rates for different SiPM models as a function of overvoltage at 300 K (a) and at 87 K (b). 62
3.21 Photo of the knudsen cell of the evaporation system. 63
3.22 Photo of the SM1 facility. 64
3.23 Scheme of the placement of each fuel element into the SM1 facility. 65
3.24 The neutron spectra expected from Monte Carlo simulations in different configurations, thermal and fast, at channel A into the SM1 facility. 65
3.25 I-V curves for three different SiPM models at different radiation exposition time. 66
3.26 Breakdown voltage (left) and quenching resistance (right) as a function of exposition time for different SiPM models. 67
3.27 Dark count rates for different SiPM models as a function of exposition time at three different value of overvoltage. 68

4.1 Scheme of two possible electrical configurations of the SiPMs array: the 1s16p (a) and 4s4p (b). 71
4.2 Photo of the SiPMs array after the TPB evaporation session on the active surfaces. 74
4.3 Photos of the experimental apparatus at CERN (a) and the detailed view of the 50 liters LAr-TPC (b). 75
4.4 Scheme of the LAr-TPC with a detailed view of the wires planes and the photodetectors. 75

4.5 Photo of the photodetectors into the LAr-TPC at CERN. the six SiPMs arrays and the PMT are in the final position. 76
4.6 Scheme of the trigger system used for the tests with the 50 liters LAr-TPC at CERN. 76
4.7 Recorded waveforms for the Hamamatsu SiPMs arrays in series and in parallel, the PMT signal and the relative muon track recorded by the wires system. 78
4.8 Recorded waveforms for the Hamamatsu SiPMs arrays in series and in parallel, the PMT signal and the relative muon track recorded by the wires system in case of very high signals due to a triggered shower. 79
4.9 Recorded waveforms for the different SiPMs arrays in parallel configuration and the relative muon track recorded by the wires system. 79
4.10 Detailed view of the waveforms for the AdvanSiD NUV SiPMs arrays in different configurations and the reference PMT. 80
4.11 Detailed view of the waveforms for the AdvanSiD RGB SiPMs arrays in different configurations and the reference PMT. 81
4.12 Detailed view of the waveforms for the Hamamatsu SiPMs arrays in different configurations and the reference PMT. 81
4.13 Experimental apparatus for the measurement of the time features of SiPMs arrays. 82
4.14 Leading edge of different arrays in different configurations as a function of overvoltage. 84
4.15 Amplitude of different arrays in different configurations as a function of overvoltage. 84
4.16 Hybrid circuit to connect four devices. 86
4.17 Detailed view of the hybrid circuit in case of bias (a) and signal (b). 86
4.18 Photo of the SiPMs array placement around the hole in which the PMT active surface will be placed. 88
4.19 Photo and drawing of one of the two identical modules composed by a SiPMs array and a PMT, for the test in LAr at CERN. . . 89
4.20 Drawing of the experimental setup for the test in LAr at CERN. 90
4.21 Comparison between the signals recorded with the PMT and the SiPMs array. 92
4.22 SiPMs array and PMT amplitude ratios for the top module (a) and the bottom module(b), calculated event by event. Gaussian fits are shown with the red lines. 92
4.23 SiPMs array and PMT leading edges ratio of the two modules The red line a gaussian and exponential fit is shown. 93

Introduction

In the past twenty years, experiments with solar, atmospheric, accelerator and reactor neutrinos have established a consistent paradigm consisting of three neutrino flavors resulting from the mixing of three mass eigenstates. However, many open questions in the field of neutrino mixing and oscillations are outlined. In particular, in recent years, a number of anomalies were observed, which indicate the possibility of non-standard oscillations models, implying the existence of at least a fourth neutrino state, called sterile neutrino because it does not interact via any fundamental interactions of the Standard Model. In this thesis the research and development of an innovative photodetection system to detect the scintillation light produced by (neutrino) interactions into liquid argon Time Projection Chambers (LAr-TPCs) is presented. Chapter 1 is dedicated to the presentation of LAr-TPC detectors powerful tools to detect neutrino interactions, illustrating the ICARUS detector involved into the SBN program at Fermilab and shortly describing the future experiments for LAr-TPCs as the Deep Underground Neutrino Experiment (DUNE). The LAr-TPCs are detectors which allows to reconstruct the tridimensional trajectory of the charged particles crossing the active volume with high spacial resolution. Furthermore, the light emitted during the interaction can be used for trigger purpose and to measure the absolute time of the event. I focus the attention on this part of the detector highlighting the advantages and the disadvantages of the actual used technology: a large area cryogenic photomultiplier tube (PMT). In chapter 2 I will introduce the physics of a semiconductor-based photodetector, the silicon photomultiplier (SiPM), which can replace the PMT in LAr-TPCs. This idea comes from the fact that PMTs cannot work under strong magnetic fields. On the contrary, SiPMs are not affected and have performance very similar to the PMTs. Furthermore, their working voltage is much lower with respect to the PMT one. The working principles and the main features of these device is presented. The next two chapters are dedicated to my Ph.D. project, as described in the following. The basic idea is to replace PMTs with SiPMs. The main problem is that the active areas of commercial SiPMs are very small, of the order of few mm^2, to be compared with that of the PMTs, of the order of few hundreds cm^2. My Ph.D. project

is oriented to study a way to increase as much as possible the total active area with the smallest, as possible, increase of the readout channels, preserving the excellent timing features of a standard PMT. In chapter 3 the study of different SiPM model as a function of temperature is presented. In the first part of this chapter the experimental apparatus I built up to characterize different SiPMs is presented. After that, I describe how I recorded and how I acquired data to evaluate the main features of each model, explaining the differences and underlying the most important characteristics for SiPM use in liquid argon. In chapter 4 the main part of my research is presented: the realization of the first single readout channel array realized with commercial SiPMs. In this chapter I will try to explain the main problems I found during the studies and how I solved them together with the last series of measurements performed at CERN and described at the end of the chapter.

Chapter 1

Liquid Argon Time Projection chambers for neutrino experiments

The Liquid Argon Time Projection chamber (LAr-TPC) is a detector that allows to reconstruct the three-dimensional trajectory of a charge particle crossing the active volume, to measure its energy and to determine the time in which the event occurs, all of them with high space and time resolutions. So, the LAr-TPC can be thought of as an electronic bubble chamber. To achieve this goal, a LAr-TPC is composed by few layers of multi-wires proportional chambers oriented at different angles, a drift chamber and a scintillation light photodetection system. All these components will be described in the following sections. This detector is usually employed in neutrino and rare events physics experiments because it allows to obtain huge active volume that increases the interaction probability. Furthermore, the liquid argon plays both the role of passive and active medium.

1.1 Neutrino physics

In the Standard Model of Glashow [1], Weinberg [2] and Salam [3], neutrinos are massless, and described by left-handed Weyl spinors. The non existence of right-handed neutrino fields is assumed: they are necessary in order to generate Dirac neutrino masses, with the same Higgs mechanism that generates the Dirac masses of quarks and charged leptons. Three generations of neutrino are assumed, one for each corresponding charged lepton, as part of the lepton doublets. From experiments a strange neutrinos behavior has been revealed: they seem to change their flavor from creation to revelation [4]. This characteristic can be explained with the mechanism of neutrino oscillations, first proposed by Pontecorvo in 1958 [5]; this mechanism supposes massive neutrinos, being so a theory beyond the standard model. In the standard theory of neutrino oscillations [6–10], a neutrino with flavor α is described by the flavor state

$$|\nu_\alpha\rangle = \sum_k U_{k\alpha}|\nu_k\rangle \tag{1.1}$$

where $|\nu_k\rangle$ are the mass eigenstates, while $U_{k\alpha}$ is an unitary matrix, which describes the neutrino mixing. The massive neutrino states $|\nu_k\rangle$ are eigenstates of the Hamiltonian,

$$\mathcal{H}|k\rangle = E_k|\nu_k\rangle, \tag{1.2}$$

with energy eigenvalues

$$E_k = \sqrt{\mathbf{p}^2 + m_k^2}. \tag{1.3}$$

The Schrödingen equation implies that the massive neutrino states evolve in time as plane waves. Let's consider now a beam composed of neutrinos of a well-defined flavor α. In the following the three momentum $\mathbf{p}$ of the different components in the beam will be assumed the same; differences in energy will derive from the masses differences. The neutrino, created with the flavor α at time $t = 0$, is described by equation 1.1. After a time t, the evolution of the initial beam gives

$$|\nu_\alpha(t)\rangle = \sum_k U_{k\alpha} e^{-iE_k t}|\nu_k\rangle \tag{1.4}$$

Since all E_k are not equal if the masses are not, equation 1.4 represents a different superimposition of the physical eigenstates ν_k compared to equation 1.1. In general, this state has not only the properties of a ν_α , but also of other flavor states. Starting from these equations it is possible to find the transition probability between two different flavor neutrinos. The theoretical procedure can be found, for example, in [11, 12]. Defining $P_{\nu_\alpha \to \nu_\beta}$ as the transition probability of ν_α in ν_β neutrino flavors:

$$P_{\nu_\alpha \to \nu_\beta}(L, E) = \sum_{j,k} U_\alpha^* U_{\beta j} U_{\alpha k} U_{\beta k}^* exp\Big(- i \frac{\Delta m_{jk}^2 L}{2E} \Big). \tag{1.5}$$

Here, L is the distance between the detector and the neutrino source of energy E. So, fixing the distance and the energy, it is possible to measure the square mass difference of the two states ($\Delta m_{jk}^2 = m_j^2 - m_k^2$). The quantities $|L_{kj}|$:

$$|L_{kj}| \equiv \frac{4\pi E}{\Delta m_{jk}^2} \tag{1.6}$$

are called oscillation lengths; they give a distance scale over which the oscillation effects can be appreciable. It has to be noticed that if the distance x is an integral multiple of all L_{kj}, then $P_{\nu_\alpha \to \nu_\beta} = \delta_{\alpha\beta}$, as in the original beam. But at distances where this condition is not satisfied, non trivial effects can be seen. In the simplest assumption of an oscillation between two neutrinos only, the matrix U takes a particularly simple form:

$$\begin{pmatrix} \cos\theta & \sin\theta \\ -\sin\theta & \cos\theta \end{pmatrix}, \qquad \text{with } \theta \in [0; \pi/2]. \tag{1.7}$$

Equation 1.5 now reduced to:

$$P_{conv}(x) = \sin^2 2\theta \sin^2 \Big(\frac{1.27\Delta m^2}{E} x \Big), \tag{1.8}$$

$$P_{surv}(x) = 1 - \sin^2 2\theta \sin^2 \Big(\frac{1.27\Delta m^2}{E} x\Big), \tag{1.9}$$

where the numerical constant 1.27 applies if $\Delta m^2 = |m_1^2 - m_2^2|$ is expressed in $(eV/c^2)^2$, while the distance from the neutrino source x is expressed in meters and the energy E in MeV. The subscripts *conv* and *surv* on the left sides of these equations denote the conversion and the survival probabilities of a particular neutrino flavor. The experimental data thus restrict Δm^2 as a function of $\sin^2 2\theta$ from the limits of the observed probabilities. In the case of three neutrinos, instead, the mixing matrix became more complex, with three mixing angle and a phase. Its most common parametrization is:

$$U = \begin{pmatrix} 1 & 0 & 0 \\ 0 & c_{23} & s_{23} \\ 0 & -s_{23} & c_{23} \end{pmatrix} = \begin{pmatrix} c_{13} & 0 & s_{13}e^{-i\delta} \\ 0 & 1 & 0 \\ -s_{13}e^{i\delta} & 0 & c_{13} \end{pmatrix} = \begin{pmatrix} c_{12} & s_{12} & 0 \\ -s_{12} & c_{12} & 0 \\ 0 & 0 & 1 \end{pmatrix} \tag{1.10}$$

where $c_{jk} = cos(\theta_{jk})$ and $s_{jk} = sin(\theta_{jk})$. This form of the matrix turns out to be very useful when considering experimental data, since the first matrix contains the parameters relevant for atmospheric and accelerator neutrino oscillations, the second one contains the parameters accessible to short distance reactor experiments and the CP violating phase δ, while the third matrix depends upon the parameters involved in solar neutrino oscillations. The exposed theory is valid for neutrinos traveling in vacuum. When neutrinos propagate in matter, as for solar neutrino inside the Sun, oscillations are modified by the coherent interactions with the medium, which produce effective potentials that are different for different neutrino flavors [13, 14]. Neutrino oscillations in matter, as neutrino oscillations in vacuum, depend again on the differences of the squared neutrino masses, not on the absolute value of neutrino masses, with an effective mixing angle in matter θ_M.

1.2 History of LAr-TPCs

Liquid argon TPCs were first proposed by Carlo Rubbia [15] in 1977 as a new method to observe and reconstruct the tracks of charged particles in large volume detectors. He proposed to use a liquefied noble gas because it does not attach electrons and hence it permits long drifts. A drawback of noble gases is that they require to be cooled at very low temperature to be liquefied. In particular, C. Rubbia proposed to use argon because of its properties:

- quite high density (1.4 g/cm^3);
- high electron mobility;
- it is cheaper with respect to other noble gases;
- it is easy to obtain and to purify;

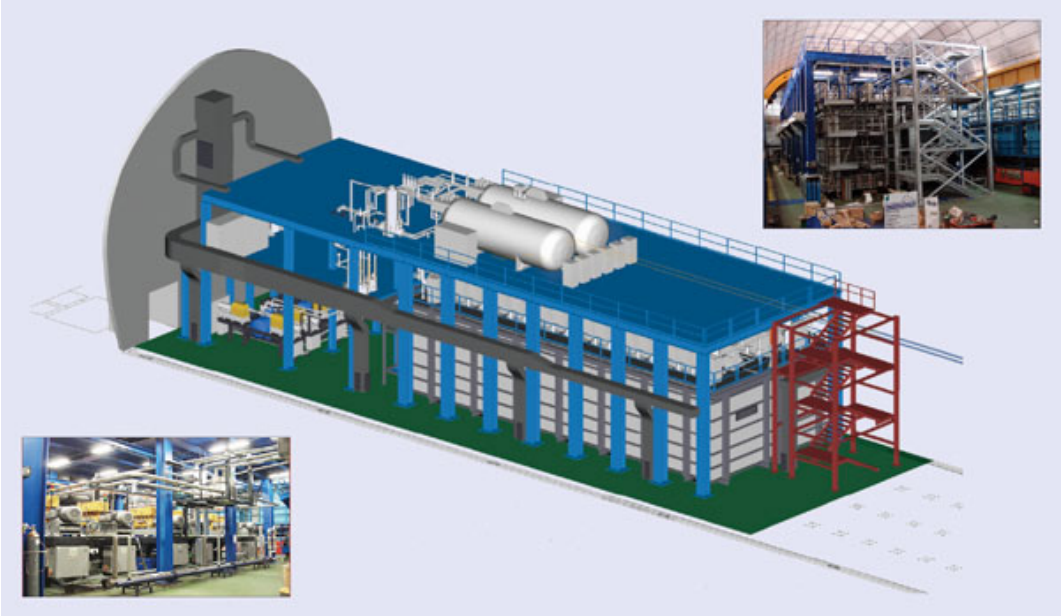

Figure 1.1: Illustration of the ICARUS T600 detector placed into the hall-B of the Laboratori Nazionali del Gran Sasso.

- its boiling point is at 87 K (at $p = 1\ atm$) and can be liquefied with liquid nitrogen.

The first LAr-TPC ever realized was set up by the ICARUS (Imaging Cosmic And Rare Underground Signals) collaboration [16–19]. After few years of R&D studies with prototypes of growing mass developed both in laboratory and with industry involvement, the collaboration built the biggest LAr-TPC, a detector filled with almost 760 tons of liquid argon, with an active volume of 476 tons. This detector, called ICARUS T600 operated with a remarkable detection efficiency from October 2010 to December 2012, accomplishing a three years physics program. It was placed in the Hall B of the Laboratori Nazionali del Gran Sasso (LNGS), 1400 m (3800 m.w.e) deep and 730 km far from the source of the CNGS (CERN Neutrinos to Gran Sasso) beam, an almost pure ν_μ beam (figure 1.1 [20]). It collected almost 3000 neutrino events and lots of additional data coming from cosmic rays, atmospheric neutrinos and proton decay. From the technological point of view, the T600 run was a complete success, featuring a smooth operation, high live time, and high reliability. The T600 decommissioning process started in June 2013; after the emptying and warming-up phase, the cryostats were opened, to recover the internal TPC detectors and the cryogenic plant and electronics to be reused in future projects. The two T300 modules were moved to CERN, where a complete overhauling (CERN WA104 project) was completed in 2017, preserving most of the existing operational equipment, while upgrading some components with up-to-date technology in view of the T600 future non-underground operation at FNAL in the SBN project. Meanwhile, several groups around the world begun to study

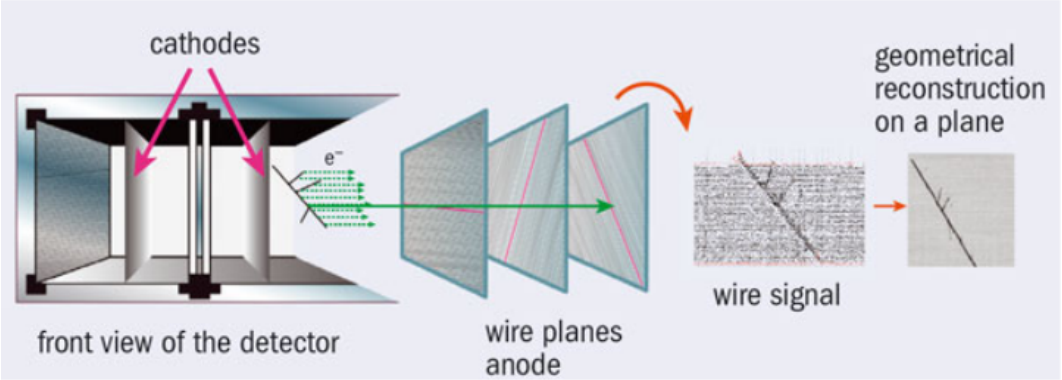

Figure 1.2: Track reconstruction in LAr-TPCs: electrons produced during the interaction generate an inducted signal on the first wires planes and are collected by the last plane.

this technology for future experiments. One of the most promising project is the Deep Underground Neutrino Experiment (DUNE), a long baseline experiment in which the neutrino beam will be produced at FNAL and detected 1300 km far, at the Stanford Underground Research Facility (SURF), South Dakota (USA). The planned far detector will be filed with 37 kton of liquid argon.

1.3 LAr-TPC operational principles

The LAr-TPC technology (figure 1.2) is very promising for use in both neutrino experiments and dark matter experiments thanks to its capability to measure the neutrinos mixing parameters through the study of neutrino oscillations. A minimum ionizing charged particle passing through the liquid argon produces 85 thousand electrons for every centimeter traversed. Those electrons are drifted in a uniform electric field toward a readout that records their drift current. Since the electric field is uniform, the electrons proceeds at constant velocity, allowing one to determine the location in the drift direction at which the ionization occurred with exceptional resolution. This resolution provides neutrino experiments with the ability to digitally record bubble chamber-like images of the neutrino interactions, allowing researchers to distinguish between different interaction processes with good certainty. Particles crossing the active volume produce electron/ion pairs drifting in opposite directions following the electric field. The work dW done by the uniform electric field E to move the charge is:

$$dw = eE(v^+ + v^-)dt = V_0 i_0 dt \tag{1.11}$$

where e is the electron charge, $v^\pm$ are the ion and electron velocities and i_0 is the readout current equal to:

$$i_0 = \frac{e(v^+ + v^-)}{d} \tag{1.12}$$

with d the anode-cathode distance. Since the electron mobility $\mu = v/E$ is orders of magnitude bigger then the ions one, the previous equation 1.12 can be approximated as:

$$i_0 \sim \frac{ev^-}{d} \tag{1.13}$$

and the signal is dominated by electrons. The charge that cam be collected for an electron/ion pair produced at a coordinate x is:

$$Q^-(x) = \int_0^\infty i_0 dt = e\frac{v^-}{d}\frac{d-x}{v^-} = e\frac{d-x}{d} \tag{1.14}$$

$$Q^+(x) = e\frac{x}{d} \tag{1.15}$$

with $Q^+ + Q^- = e$ the elementary charge produced during the interaction. Beside the charge production, also light is emitted isotropically and a photon detection system, usually placed behind the anode, can detect it. This light is useful for triggering purpose and to determine the absolute time of the event (t_0) thanks to the higher velocity of photons with respect to the electrons.

1.3.1 Liquid argon properties

Liquid argon, as other light noble gases, is an optimal material to be used in TPCs thanks to its physical properties. As demonstrated in the first test by the ICARUS collaboration in 1993 [21], liquefied noble gases can be used as targets for particle interactions, for a number of reasons. For instance, they produce scintillation light. For this reason both excitation and ionization due to an impinging particle can be measured: this allows to collect a great deal of information, which helps defining the nature of projectile as well as the interaction characteristics and geometry. As can be seen in table 1.1, where the physical properties of noble gases are compared, xenon appears to be the best solution, but for several reasons argon is preferable: for instance it is easier to get from atmosphere and it is cheaper with respect the others; furthermore, thanks to technological developments it is possible to storage large quantities with very high level of purification, i.e. very low impurity levels. All these properties implies that liquid argon detectors can be easy scaled to very large masses (ktons) with respect to the other materials. Despite this, argon has a significant inconvenience, that is the presence of a radioactive isotope, ^{39}Ar, in the gas derived from atmosphere. This isotope produces a significant background by decaying β^-, with an energy endpoint of 565 keV and an half-life around 269 years. The nuclide ^{39}Ar has a measured activity of (1.01 ± 0.08) Bq per kg of natural Ar, corresponding to a concentration of $(8.0 \pm 0.6) \times 10^{-16} g(^{39}Ar)/g(^{nat}Ar)$ [22]. The beta spectrum of ^{39}Ar can be recorded and characterized by a detector with a sufficiently low energy threshold. Though it can be a very intense source of noise, it can subtracted from the data when performing calibrations with external sources. On the other hand during physics runs, ^{39}Ar-driven events can be recognized as background and

Table 1.1: Some physical parameters of some liquefied noble gases. Here, d is the density, λ is the radiation length, t_b is the boiling point temperature and μ is the electron mobility.

	d (g/cm^3)	dE/dx (cm)	λ (cm)	t_b (K)	μ (cm/Vs)
LAr	1.394	2.10	14.0	87.3	500
LKr	2.410	3.00	4.85	120	1200
LXe	3.057	3.79	2.77	166	2200

rejected, thanks to the properties of scintillation in Argon. Another important distinction between argon and xenon is that the two liquids behave differently with respect to light production. Xenon has two scintillation light components as Argon, but their relative intensity presents small variations for distinct interacting particles. On the other hand liquid Argon shows very different light signals for electron and nuclear recoils, which translates in a unique way to perform particle discrimination, with respect to Xenon.

1.3.2 Ionization in liquid argon

Ionization in Liquid Argon is heavily dependent on the nature of the interacting particle. This affects both the effective charge separation and the subsequent process of recombination, which depends on the density of ionization centers. Moreover scintillation is partly due to recombination itself, so that also the measured light yield is related to the nature of the ionizing particle. With the application of an electric field, it is possible to collect the produced charge (ionization electrons) and study the charge/light ratio and/or energy deposition, to determine the particle nature and its kinematic properties. Through the Birk's Law, originally introduced to describe quenching effects for scintillation, it is possible to express the charge collected on the electrodes (Q) as a function of the ionization charge (Q_0) and the electric field (E):

$$Q = \frac{Q_0}{1 + \frac{k}{E}} \tag{1.16}$$

where k is the recombination coefficient that has to be measured experimentally. In liquid argon $k = 560\ V/cm$ and it is verified by the ICARUS collaboration during the tests with the 3-tons prototype and the first technical run of the T600 detector. In figure 1.3 the charge and light components as a function of the electric field is shown. In particular, in the upper part of the figure it is possible to see that, for an electric field of 500 V/cm both the collected charge and the light are the 50% of the total. Ionization yield is also dependent on the particle energy and on how it is dissipated into the medium [23]. The energy deposition per unit of path (dE/dx) for a relativistic particle, which is the most frequent case for a LAr-TPC, can be found with the *Bethe-Block formula*. Considering β factor lower than 0.1 there is no an unified theory on

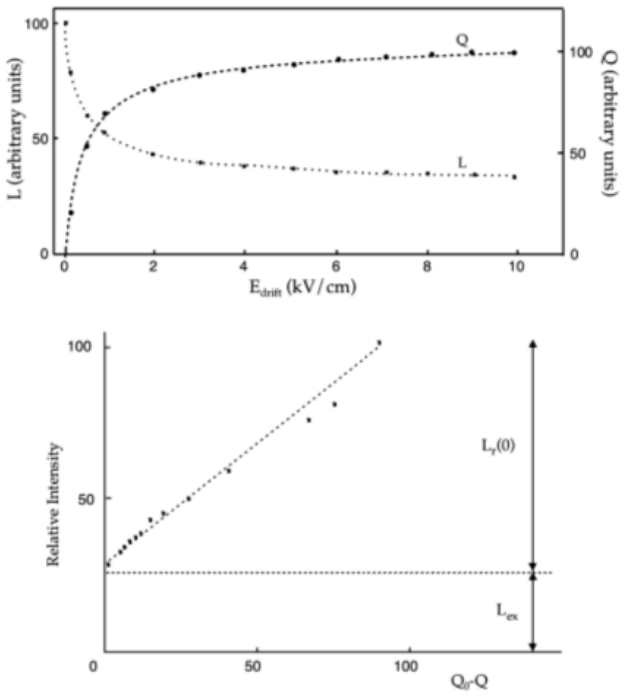

Figure 1.3: Relation between Argon luminescence and collected charge. In the upper panel (a) the luminescence intensity L and the fraction of collected charge Q as function of the applied electric field are shown: the 100 values represent, respectively, the total light collected at zero field and the initially produced charge Q_0. In the lower panel (b) the linear relation between the detected light intensity and the lost charge $Q_0 - Q$ is shown, as function of the applied field.

energy transfer in collisions. It is thought that in this range ionizing particles can capture almost-free electrons, effectively shielding their own charge and thus decreasing their ionization efficiency. If $0.01 < \beta < 0.1$ several empirical formulas are used to correct the Bethe-Bloch formula. For even lower β, inelastic collisions with electrons almost reduce to zero, while energy is transferred to the medium via direct interaction with atoms. This energy transfer mechanism significantly lowers ionization efficiency; the process in this region was successfully described by Lindhard's theory [24, 25].

1.3.3 Light production in liquid argon

An interaction in argon produces both atomic excitation and ionization, leading to a narrow band 128 nm luminescence emission [26–28]. As experimentally measured the scintillation light exhibits two different components: the so-called recombination luminescence and self-trapped exciton luminescence (excitation luminescence). The recombination luminescence, L_r, in the VUV range, originates from the following processes [29]

$$Ar^+ + Ar \rightarrow Ar_2^+ \tag{1.17}$$
$$e^-_{hot} + \text{collisions} \rightarrow e^-_{th} \tag{1.18}$$
$$Ar_2^+ + e^-_{th} \rightarrow Ar^{**} + Ar \tag{1.19}$$
$$Ar^{**} \rightarrow Ar^* + \text{heat (n.r.t.)} \tag{1.20}$$
$$Ar^* + Ar \rightarrow Ar_2^+ \tag{1.21}$$
$$Ar_2^* \rightarrow Ar + Ar + h\nu(\text{VUV}). \tag{1.22}$$

This process is characterized by the presence of free electron/ion pairs. Here, Ar is the argon atom in the ground state, Ar^+ and Ar_2^* are the ionized atom and molecule (dimer) respectively, Ar^* and Ar_2^* are the excited atom and molecule respectively, Ar^{**} the highly excited atom, e_{hot} and e_{th} are sub-excitation and thermal electrons respectively. In equation 1.20 "n.r.t." means "non radiative transition". On the other hand the excitation luminescence, L_{ex}, produced by the simpler process [29]

$$Ar^+ + Ar \rightarrow Ar_2^* \tag{1.23}$$
$$Ar_2^* \rightarrow Ar + Ar + h\nu(\text{VUV}), \tag{1.24}$$

is prompted by the presence of the excited argon atom. Both processes, ending up with the same radiative reaction, induce the emission of a 128 nm VUV photon ($E \simeq 9.7\ eV$), 5 nm FWHM. Scintillation light, coming from the recombination of electron-ion pairs, is inversely proportional to the strength of the electric field applied to the detector active volume. As a consequence, free-electron yield rises with the field value while photon yield decreases. In both cases saturation occurs, for minimum ionizing particles, at $E_{drift} > 10\ kV/cm$. For instance, at the nominal drift field applied in the ICARUS T600 detector of $E_{drift} = 0.5\ kV/cm$, approximately the same amount of photons (~ 4000

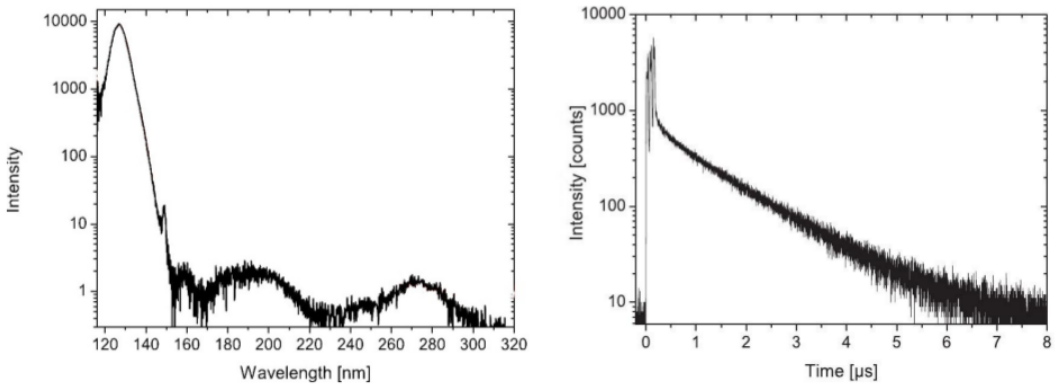

Figure 1.4: Scintillation light intensity as a function of wavelenght (left) and emission time (right).

γ/mm) and free electrons ($\sim$ 5000 ion-electron pairs per mm) are produced for minimum ionizing particles [30]. Both the light components, from recombination (L_r) and excitation (L_{ex}), are characterized by a double time emission scale: measurements at different field conditions show that both excitation and recombination luminescence have two different components, one *fast* component with a decay time $\tau_f \simeq 6\ ns$, and a *slow* component with $\tau_s \simeq 1.5\ \mu s$ (figure 1.4 [26]). This feature, common to many scintillating materials, can be attributed, in this case, to the fact that Ar_2^*, before decaying to the fundamental dissociate state $^1\Sigma_g^+$, can be formed in three different states: two singlets ($^1\Sigma_u^+$ and $^1\Sigma_u^-$) and one triplet ($^3\Sigma_u^+$) state [31]. While the second singlet state cannot decay radiatively due to parity conservation, the other two can. Although the triplet-to-ground state transition should be in principle forbidden by the selection rule $\Delta S = 0$, thus resulting in two different decay constants, the latter much larger than the former. This quite large difference is unique in argon among other noble gases. The relative intensity of the two components, fast (c_f) and slow (c_s), depends on the dE/dx of the interacting particle, ranging from $c_f : c_s = 1 : 3$ in case of m.i.p. up to $c_f : c_s = 3 : 1$ in case of high ionizing particle, such as α particles, allowing in some particular cases a discrimination among them [32]. This isotropic light signal propagates with negligible attenuation throughout LAr volume. Indeed, LAr is fully transparent to its own scintillation light, with measured attenuation length in excess of several meters and Rayleigh scattering length of $\sim 90\ cm$. Because their short wavelength, the scintillation photons are absorbed by all the detector material without reflection, leaving time and amplitude information unaffected during the photon path to the light detectors. So they keep information about the time of generation, i.e. the ionizing particle interaction time and the time evolution of the interaction event in LAr.

1.4 A LAr-TPC photon detection system: the ICARUS T600 case

The Imaging Cosmic And Rare Underground Signal (ICARUS) detector is, nowadays, the biggest LAr-TPC ever involved in neutrino oscillations research. It consists of two identical modules filled by about 380 tons of liquid argon each (they are commonly called *T300 modules*). Each module consists of two LAr-TPCs placed with a common cathode in the middle. The pre-assembly of the modules was performed in Pavia, Italy, in 1999. In 2001 the first T300 was ready for the first test run at sea-level. For three months it collected several cosmic rays events that highlighted the main features of the detector [33]. After the tests, in 2004, the two T300 modules were moved to the underground laboratories of *Laboratori Nazionali del Gran Sasso* (LNGS), Italy, and placed in the Hall B into a common thermal insulation plant to form the so-called *T600 detector*. From 2010 up to October 2012 the ICARUS T600 experiment operated with remarkable detection efficiency during the exposition on the CERN to Gran Sasso (CNGS) neutrino beam. The T600 detector decommissioning process started in June 2013 and in December 2014 it was moved at CERN for a complete refurbishing in view of the future shallow underground operation at Fermilab National Laboratories (FNAL), Batavia, United State of America, in the framework of the SBN (Short Baseline neutrino) program (figure 1.5). SBN program scientific goal is a 5-sigma analysis of the possible sterile neutrino existence in the parameter space suggested by LSND. The LSND experiment stands perhaps as the first possible evidence of new physics, beyond the Standard Model, showing an excess ν_e signal indicative of the existence of one or more sterile neutrinos. The nature of the signal is however limited to a rate, with some energy information [34–37]. Other experiments, such as the MiniBooNE experiment did not see a direct evidence in ν_e appearance, though a low energy excess in their data could potentially accommodate the existence of sterile neutrinos. Their antineutrino data, though statistically limited, appear instead to show consistency with the original LSND signal [38–40]. The latest results from a re-analysis of the neutrino reactor data, which reflects a rate dependence as well, appear consistent with this sterile oscillation picture. Finally, calibration data from Gallex and Sage also suggest a deficit which hints at the existence of sterile neutrinos [41–47]. The SBN program is proposed to include three LAr-TPC detectors located on-axis in the Booster Neutrino Beam (BNB). The near one (LAr1-ND) will be located at 110 m from the BNB target while the MicroBooNE apparatus will be located at 470 m. The far detector will be the improved ICARUS-T600, located at 600 m from the BNB target. The different locations have been chosen to optimize sensitivity to neutrino oscillations and to minimize the impact of flux systematic uncertainties [48]. Concerning the photon detection, the system used at LNGS by the ICARUS detector has been improved during the refurbishing, replacing the 74 cryogenic PMTs model Electron Tubes Ltd 9357FLA of 8

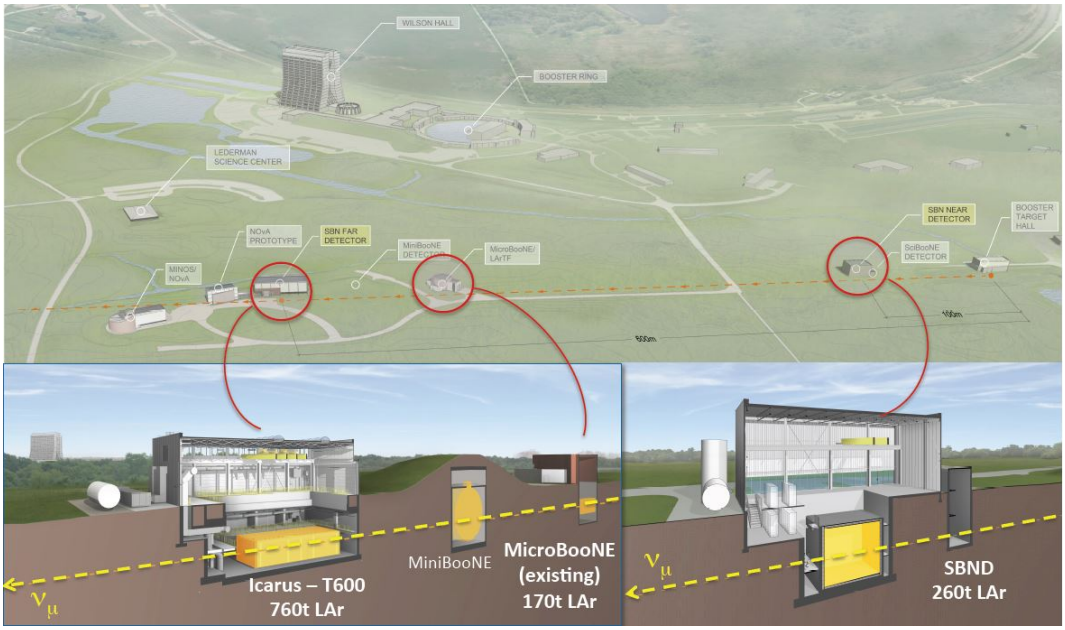

Figure 1.5: Scheme of the placement of the different detectors at Fermilab for the SBN experiment.

inches diameter and 12 dynodes (no more commercially available), with 360 Hamamatsu R5912-mod cryogenic PMTs of 8 inches windows diameter and 10 dynodes multiplication stages. The main reason to increase the number of PMTs is that at FNAL the ICARUS T600 detector will be placed only few meters below the surface and lots of cosmic rays events are expected. The Photon Detection system in the new configuration allows to reject all these events and recognize the signals associated to the neutrino beams. In the next paragraphs the performance of these PMTs and the readout electronics will be presented to underline the difficulties to manage as well as possible a large number of PMTs for triggering and t_0 measurements.

Photon detection system

Usually, LAr-TPC anode is composed by at least two parallel multi-wires planes placed at different orientation. For instance, the ICARUS T600 TPCs are made of three wires planes, arranged 3 mm apart, at 0° and ±60° with respect to the horizontal line. The wires have a diameter of 150 μm and a relative distance of 3 mm. This configuration, as well as ensuring an optimal reconstruction of each track crossing the active volume, also provide a large transparency to the scintillation light. So, the PMTs are normally placed behind the third wires plane (figure 1.6). In the new configuration, the ICARUS light detection system has 90 PMTs for each TPC placed as shown in figure 1.7, directly immersed in liquid argon. The layout comes from Monte Carlo simulations and the PMTs model was chosen considering the performance in

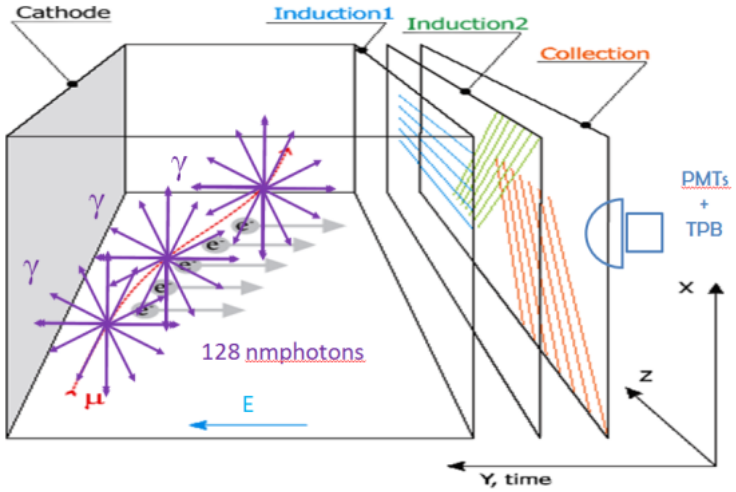

Figure 1.6: PMTs are usually placed behind the wires planes.

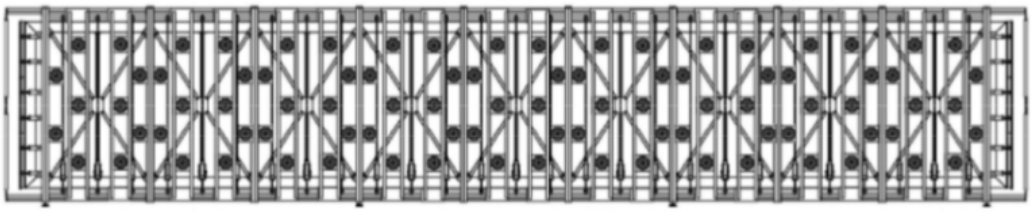

Figure 1.7: Scheme of the ICARUS LAr-TPC PMTs deployment. For each TPC there are 90 8-in. PMTs.

liquid argon, in particular for what concern the gain, the quantum efficiency, temporal response and the signal linearity [49]. Some considerations have to be taken into account, such as the temperature of liquid argon (87 K) that requires a Bialkali photochatode deposited on a platinum under-layer in order to avoid electrical discharges and dispersions, and a material to adapt the wavelength of LAr scintillation light to the peak of sensitivity of the PMT. Since the PMT window is not transparent to the VUV light emitted in argon, the most common solution is to use a *wavelength shifter*. For the ICARUS PMTs a deposition of wavelength shifter directly on the glass window has been adopted.

1.4.1 Wavelength shifter deposition

The PMT photocathode is sensitive to visible light with the sensitivity peak around λ = 400-450 nm, whereas the LAr emits light in the VUV region at $\lambda = 128\ nm$. At this wavelength, PMT sensitivity is almost null and the device becomes useless. The most efficient way to detect scintillation light in LAr is to convert the VUV light to visible light using materials that absorb high energy photons (VUV region) and re-emit them at lower energy (visible wavelengths). In this section I will expose the properties of the most common wavelength

shifter used for high energy physics experiments and the techniques adopted by the ICARUS group to coat the PMT photochatodes. At the end of the section the results obtained comparing different wavelength shifters in some test I carried out during my Ph.D. thesis work will be presented. Some aromatic organic compounds emits fluorescence light when their II-orbital electrons are excited, either by ionizing particles or ultra violet radiation [50]. Electrons excited to the vibrational states of the first excited state (S_1) relax within few picoseconds to the lowest lying level of S_1, before decaying to the ground state with the radiation of a photon at the compound characteristic emission wavelength. In plastic scintillators, the binder in which the wavelength shifter is dissolved must have a II-electron structure and absorbs the incident energy. If the concentration of the wavelength shifting solute is high enough, this energy is transferred by non radiative dipole-dipole interactions to its excited levels, producing fluorescence. The transfer is efficient if there is good overlap between the binder emission spectrum and the absorption spectrum of the solute. Energy transfer to further solutes is possible, allowing the final light to be shifted to even longer wavelengths. Usually the wavelength shifter can be applied directly to the crystal faces, target vessel wall, front face of a light guide or photo-sensitive part of a photodetector. One of the most used compound to shift VUV light to visible wavelength is the 1,1,4,4-tetraphenyl-1,3-butadiene (TPB). This is an organic chemical compound whose chemical formula is

$$(C_6H_5)_2C = CHCH = C(C_6H_5)_2.$$

TPB absorbs light across a broad wavelength range from high ultraviolet up to its emission peak, which lies at $\lambda = 425 \pm 50\ nm$. Since liquid argon emits light at $\lambda = 128\ nm$ (see section 1.3.3) and the peak of sensitivity of PMTs (such as the other photodetectors) is around 430 nm, TPB is a good candidate as wavelength shifter. By visual inspection it appears composed by white and yellow-white needles. Furthermore it is soluble in Toluene and can be evaporated to cover the device. To take advantage from this last physical property, heating a small quantity of TPB it is possible to reach its evaporation point, around 220 $°C$ avoiding to burn it. In this way, it is possible to obtain a uniform deposition to ensure the best performance. To achieve the best coating results in terms of uniformity of the deposition, efficiency in terms of wasting material and time needed to complete the process, the ICARUS collaboration develop a a dedicated procedure [51, 52] that is described below. This is an important step and it requires special attention because the quantum efficiency of the photodetector depends on the efficiency of the TPB that this is strongly dependent on the thickness of the TPB deposited [53–55].

TPB evaporation system

The ICARUS PMTs are, as already mentioned above, the Hamamatsu R5912-MOD with a photosensitive window diameter of 8 inches. However, this surface

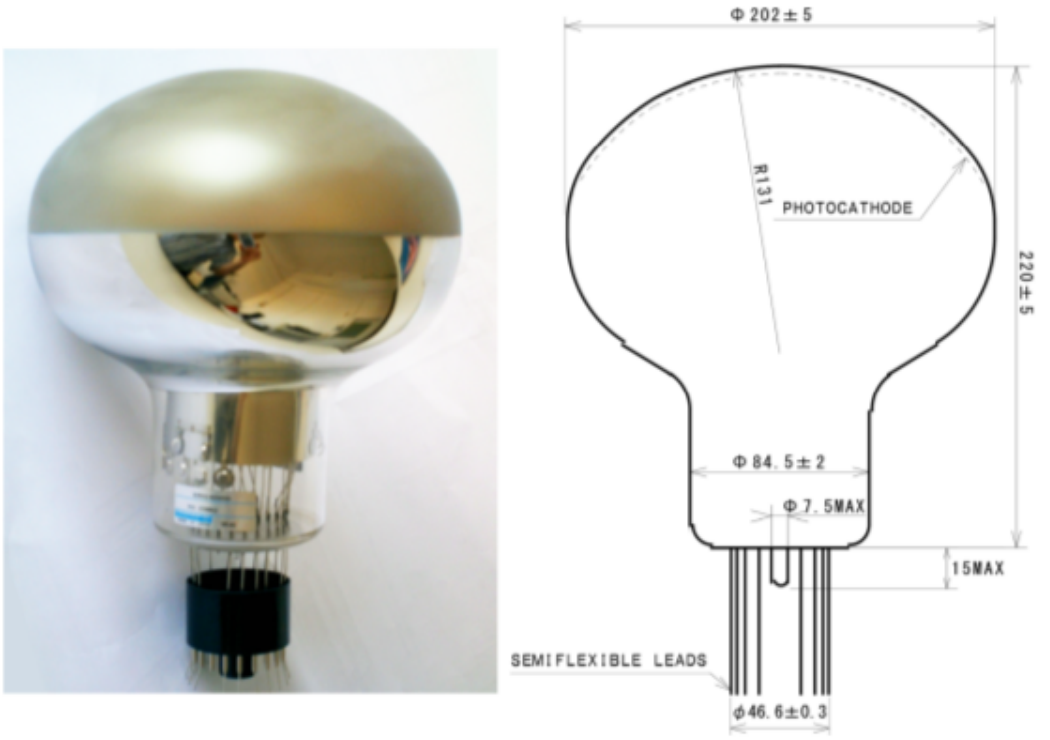

Figure 1.8: Photo and scheme of the Hamamatsu R5912-mod.

has a convex shape as visible in figure 1.8. So, considering the convexity of the surface on which the WLS must be deposited, a standard chamber simply made by an evaporation cell with the PMT over it, cannot guarantee a uniform deposition because of its shape, especially on the edges of the photodetector. For this reason, the ICARUS collaboration decided to install a motorized rotating feed-through on the top of a vacuum chamber, on which the PMT is mounted at an angle of 40° with respect to the cover. Below the PMT, a Knudsen cell is mounted. The PMT tilt angle and the distance from the Knudsen guarantee, considering the device rotation, a geometrical uniformity of the expected evaporation process between center and border of the window surface. In figure 1.9, the complete system is shown. Evaporation is carried out following a protocol that guarantees a high optical yield and uniformity. Even though the treatment can be performed on one device at a time, the procedure takes only 3 hours. When the pressure inside the vacuum chamber is of the order of 10^6 $mbar$, the motor starts to rotate slowly, at 10 turns/min, and the temperature regulator is set to 220 $°C$. When the temperature reaches 190 $°C$, the shutter over the Knudsen cell is opened, letting the material to reach the PMT by evaporation. Thanks to this technique, each PMT could be covered with an uniform layer of TPB that guarantees a quantum efficiency of 12 ± 1 %.

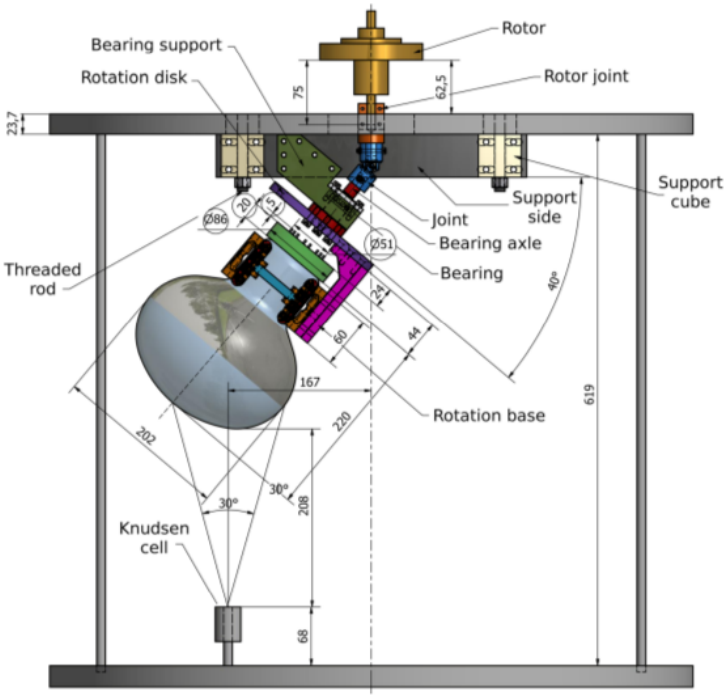

Figure 1.9: Mechanical scheme of the evaporation system used for the ICARUS PMTs.

1.4.2 PMT performance in LAr

The performance of some PMTs at cryogenic temperatures have been performed from several groups during the last years. We tested some PMTs with similar performance to choose which one has to be used for the SBN experiment. The main features we considered are the gain, the quantum efficiency, the linearity and the capability to recognize the single photon interaction, the so called Single Electron Response (SER) and the dark noise rate. All the measurements are performed both at room and cryogenic temperature to compare the behavior as a function of the temperature. Furthermore, for practical reasons the characterization at low temperature are usually performed in liquid Nitrogen ($T = 77K$) instead of liquid argon. PMTs under analysis have a 8 inches diameter sand-blasted window made of borosilicate glass and a bialkali photo-cathode (K_2CsSb) with platinum undercoating, in order to restore the photocathode conductivity at low temperature. In particular I present here the results of 3 PMT models: the Hamamatsu R5912 Mod and R5912-02 Mod PMTs that have 10 and 14 dynodes respectively, and the ETL 9357 KFLB with 12 multiplication stages. All the PMTs were illuminated with the same laser source at $\lambda = 405\ nm$ and with the same electronic chain to characterize the devices in terms of gain and photocathode uniformity. To measure the quantum efficiency we used a deuterium lamp source into a vacuum chamber optically connected to a VUV monochromator. The gain of a PMT decrease with the temperature as shown in figure 1.10 of about 35% for the Hamamatsu

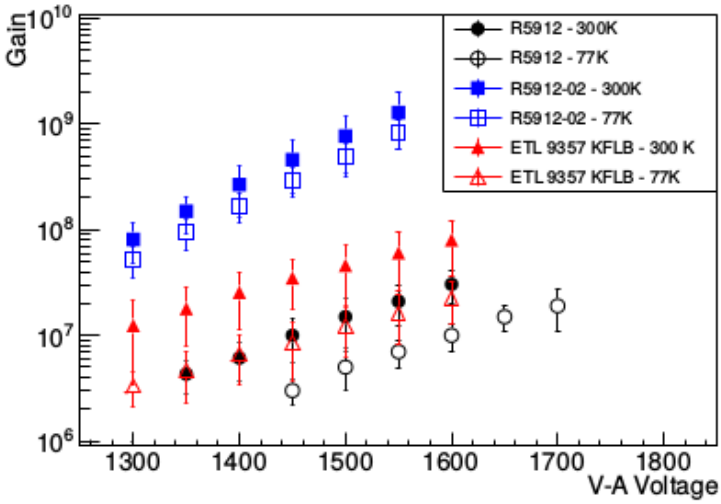

Figure 1.10: Gain measurements of different PMT models as a function of the bias voltage both at 300 K and 77 K.

R5912-02 Mod model, and of about 70% for the other two models. Even if the gain of the Hamamatsu R5912 is the lowest with respect to the others, due to the different number of dynodes, the linearity of this device as a function of the number of photons has the best result. In figure 1.11 the gain as a function of the number of photons for each device both at room and cryogenic temperature is shown. The PMTs dark count rate was measured with a different discrimination threshold that was gradually increased from 1 to 255 mV, with 1 mV steps. As shown in figure 1.12 the rate decreases with increasing the threshold but, more important, it increases with decreasing temperature: this effect is referred as Non-Thermal Dark Rate. The source of this emission is found in the photo-cathode, but its nature and features are not yet understood [56,57]. It could be ascribed to a decrease of the lattice-energy of the cathode material at low temperature, resulting in an increase of the electron escape probability.

1.4.3 Trigger and data acquisition system

The ICARUS T600 detector is being installed at FNAL after an extensive overhauling to be exposed to neutrino Booster (BNB) and NuMI beams in the framework of the SBN program for the ultimate search of sterile neutrinos. At the nominal BNB intensity of $5 \cdot 10^{12}$ pot/spill extracted in about 1.6 μs time window with a standard 4 Hz repetition rate, $\sim$ 1 neutrino interaction every 180 spills is expected to occur in the T600 detector with vertex in the LAr-TPCs. A similar event rate, one every 210 spills, will come from beam-associated events, essentially from the muon beam halo and from interaction in the material surrounding the T600. The dominant event rate, 1 over 55 spills, is expected from cosmic rays inside the spill. It follows that 1 event over 35 spills, i.e. 1 event every 8.8 s is foreseen in the T600 LAr-TPC at the standard 4 Hz

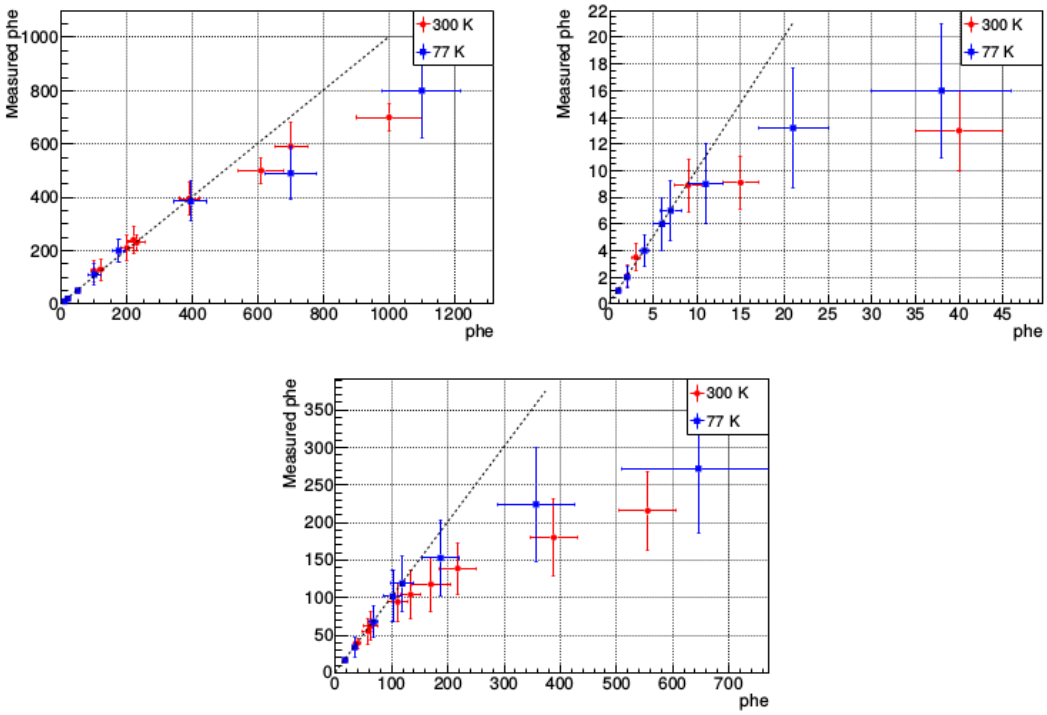

Figure 1.11: Linearity of R5912 (top-left), R5912-02 (top-right) and 9357 KFLB (bottom) at room and at cryogenic temperature.

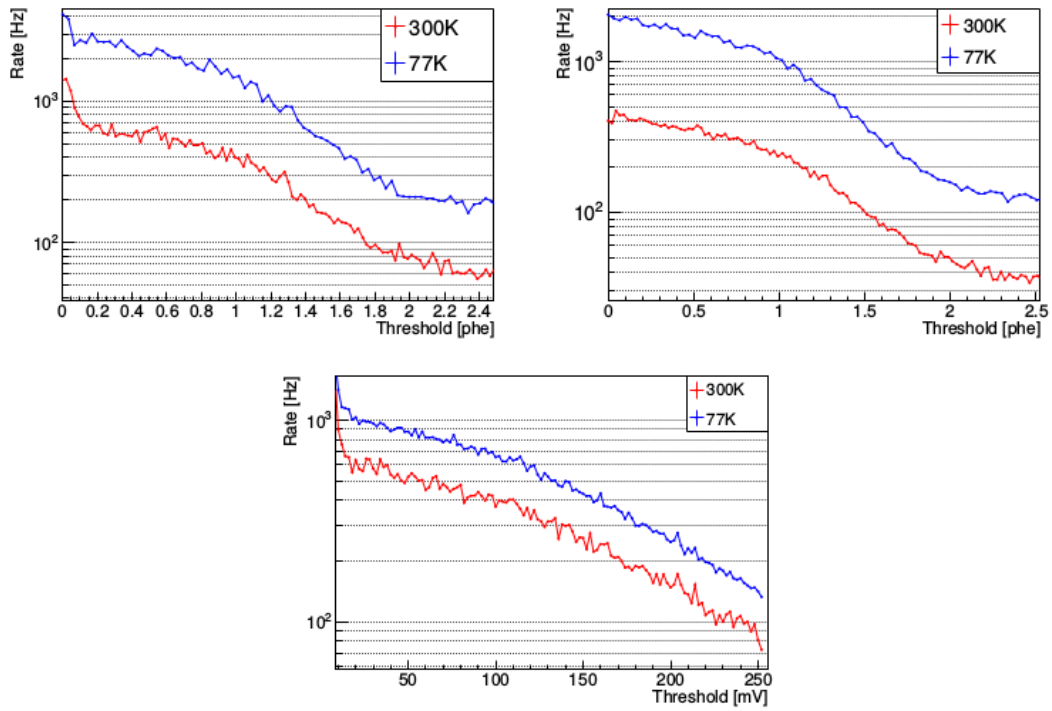

Figure 1.12: Dark count spectra for R5912 (top-left), R5912-02 (top-right) and ETL 9357 KFLB (bottom) at room and at cryogenic temperature.

repetition rate of the Booster Neutrino Beamline. The designed trigger system would select the genuine neutrino interactions while rejecting background and noise. For this purpose a staged level can be adopted, aiming at progressively reducing the amount of data from the front-end buffers to the off-line storage. The trigger system of the ICARUS-T600 detector will exploit the coincidence of the prompt signals from the scintillation light in the LAr-TPC, recorded by the PMT system, with a beam gate window generated in correspondence to the expected arrival time of neutrinos in the T600 from an "early warning" information on the proton spill extraction of BNB and NuMI beams. At a higher level, a successive time comparison of the scintillation light signal and the Resistive Wall Monitors signal located along the beamline, would allow a rejection of fake triggers by exploiting the fine structure of the bunched beam. Collected events can be further thinned out using the signals from the Cosmic Ray Tagger (CRT) to identify cosmic particles entering the detector. A $\sim$1-2 ns time resolution of PMT and CRT systems, as well as a synchronization among all the sub-detector units at the same level, are required to these purposes. The 360 PMT signals will be recorded with a series of high resolution digitizers and synchronized with the beam gate. The fired PMTs generate a trigger signal that can be propagated through all the detectors. At this point it is evident that the choice to have a relative low number of large area photodetectors is an advantage from the point of view of data acquisition and trigger signal generation. Furthermore, higher the number of devices immersed in liquid argon, higher the number of feed-through for bias and readout purposes. The best solution comes from a good ratio between the spatial resolution of the photodetector (proportional to the active area of the device) and the readout channels.

1.5 Future projects

Beside the already mentioned SBN program in which the ICARUS T600 detector is involved, there are other planned experiments based on the LAr-TPC detection technique. The goal of these experiments is to find the best way to increase the active mass up to few tens of ktons of liquid argon and to improve the performance of the actual LAr-TPC in terms of sensitivity, reconstruction capability, readout electronics and so on. The *Deep Underground Neutrino Experiments (DUNE)* is a neutrino research program based on very huge mass LAr-TPCs planned for the next years. Nowadays, there are some groups involved in the so called *protoDUNE* program, a smaller test-version of the DUNE detector. In this section I will describe shortly the DUNE experiment and the status of the protoDUNE program.

1.5.1 The DUNE experiment

The DUNE experiment is a *long baseline neutrino oscillations* experiment based on LAr-TPCs detectors dedicated to the study of neutrinos properties. In particular the main goals of the program are:

- to carry out a comprehensive investigation of neutrino oscillations to test CP violation in the lepton sector, to determine the ordering of the neutrino masses and to test the three-neutrino paradigm;
- to perform a broad set of neutrino scattering measurements with the near detector;
- to exploit the large, high-resolution, underground far detector for non-accelerator physics topics including atmospheric neutrino measurements, searches for nucleon decay, and measurement of astrophysical neutrinos especially those from a core-collapse supernova.

For the first phase of the project, a neutrino beam of energy between 60 and 120 GeV and power of about 1.2 MW produced by the NuMI neutrino beam at Fermilab will be detected by one near high resolution LAr-TPC detector and one far 10 ktons fiducial mass LAr-TPC detector placed in the Sanford Underground Research Facility (SURF) at 1300 km far from FNAL. During a second phase an increase of the beam power at least to 2.4 MW and the increase of the fiducial mass of the far detector up to 40 ktons of liquid argon will be expected.

The near detector

The near detector will be placed at about 500 meters from the the neutrino beam production point. To achieve the precision required to make a significant advance in the measurement of neutrino oscillation parameters over current experiments and to reach the desired 5σ sensitivity to CP violation, a highly-capable, high-precision near detector is required to measure the not-oscillated flux spectrum to a few percent for all neutrino species in the beam $(\nu_e, \bar{\nu}_e, \nu_\mu, \bar{\nu_\mu})$ and to precisely measure neutrino cross sections necessary to interpret the far detector signal and backgrounds. This requires a high resolution, magnetized near neutrino detector for identifying and measuring electrons and muons with high efficiency. To measure both the small ν_e and $\bar{\nu}_e$contamination in the beam with high precision, the detector would need to be able to distinguish e^+ from e^-. Additionally, using a target nucleus similar to the far detector would allow cancellation of systematic errors and inclusion of other target nuclei would provide constraints for accurate modeling of nuclear effects.

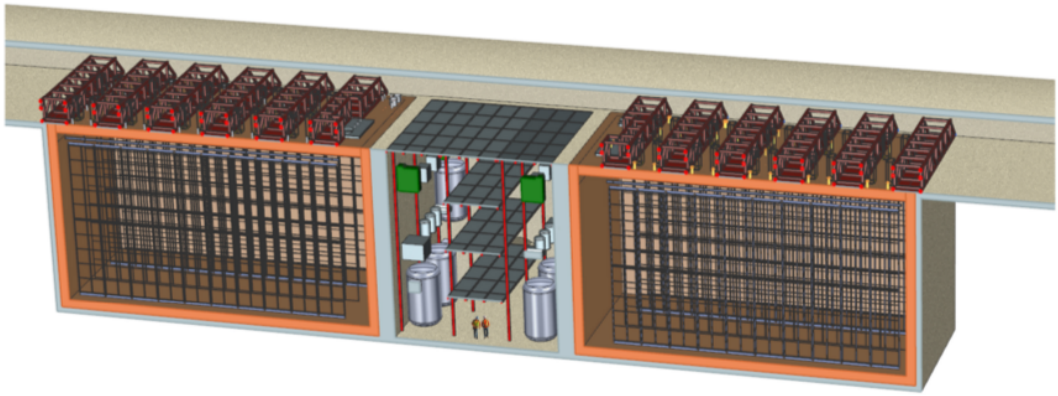

Figure 1.13: Scheme of the far detector for the DUNE experiment.

The far detector

The far detector (figure 1.13), as already mentioned will be composed of very huge mass LAr-TPCs with a fiducial mass of about 40 ktons in the final configuration. This enormous quantity of liquid argon and the very big size of the drift region of each TPC (of the order of 5 meters, for a drift time of about 2.2 ms) require special attention on reliability and technological developments that are still under study. However, beside the wires planes for the charge collection of particles crossing the active volume that will be similar to those used by the ICARUS T600, the photon detection system is still an open item. In fact, there are different possibility that can be considered. The most interesting is the possibility to replace the large area PMTs with devices with similar performance but insensitive to the magnetic field. This is especially true also for the near detector. This possibility represent the basis of my Ph.D. research work and that will be exposed in detail in the next chapters.

The protoDUNE proect

Nowadays, some experimental groups are working on prototypes of the DUNE far detector. Usually these experiments are called protoDUNE and they are characterized by different field of studies. For what concern the scope of this thesis, I will focus the discussion of the so called protoDUNE-SP, a single phase LAr-TPC of about 770 tons of liquid argon, realized at CERN in the framework of the Neutrino Platform activities, that starts operations this year. This detector represent the biggest LAr-TPC ever realized and it is shown in figure 1.14. The detector elements, consisting of the TPC, the cold electronics, and the photon detection system, are housed in a cryostat that contains the LAr target material. The cryostat, a free-standing steel-framed vessel with an insulated double membrane, is based on the technology used for liquefied natural gas storage and transport. A cryogenics system maintains the LAr at a stable temperature of about 89 K and at the required purity level through a closed-loop process that recovers the evaporated argon, recondenses and filters it, and

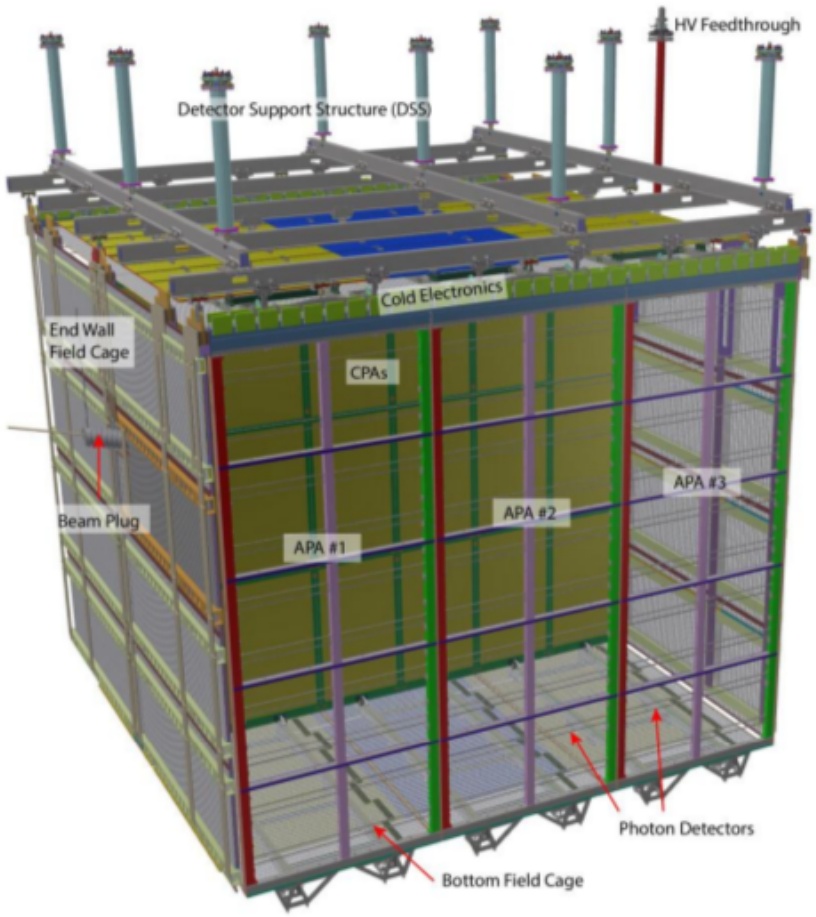

Figure 1.14: Scheme of the ProtoDune LAr-TPC.

returns it to the cryostat. For what concern the photon detection system, there are some different setups under test, but all of them have one common feature: the photodetector. Instead of classical PMTs, the protoDUNE-SF experiment is using silicon photomultipliers (SiPMs), semiconductor-based photodetectors characterized by high gain and low bias voltage. Since my Ph.D. program is based on research and development of SiPM at cryogenic temperature for application in liquid argon, the chapter 2 is dedicated to the description of these devices and the chapters 3 and 4 are dedicated to the description of my research.

Feedback

In this chapter some of the main features of LAr-TPCs have been described. Nowadays large area PMTs are used to detect the scintillation light. There are several PMT models of different shapes and different sizes but the working principle is the same and can be summarized in four steps:

1. photons are converted in electrons through photoelectric effect on the photocathode;

2. an electric field accelerates the generated photoelectrons and focus them on the first electrode, called *dynode*;

3. thanks to the capability of each dynode to emit secondary electrons, a multiplication of the order of 10^6 can be reached through a dynodic chain;

4. at the end of the multiplication chain an anode collect the electric signal which can be analyzed.

Especially for big active surfaces that can be obtained with PMTs, these devices are commonly used also in huge mass detectors, but they also have some defects. First of all, because of the big size, a strong magnetic field can destroy the multiplication efficiency and make the PMTs unusable. Then, they require high bias voltage to reach gain of the order of 10^6 or 10^7, for example, the Hamamatsu R5912 8 in. PMTs which are used in ICARUS T600 detector have a working voltage of about $V \sim 1300\ V$. In the last years, thanks to the diffusion of semiconductor-based photodetectors with high gain, the *Silicon PhotoMultipliers - SiPMs* (sometimes called SiliconPMs or MPPCs - Multi-Pixel Photon Counters), several groups starts to study a solution to replace the PMTs system with a SiPMs system. A SiPM has the advantages to be insensible to magnetic fields because of its compact structure and its working voltage is much lower than the PMT one (around few tens volts). Moreover, because of the semiconductor structure, it has an higher noise rate in comparison with the PMT one and its active surface is smaller than few cm^2. To compensate these disadvantages, several alternatives are under study, such as:

- coupling SiPMs with optical fibers;
- coupling SiPMs with scintillator bars (or a mix of scintillator and optical fibers);
- use SiPMs arrays;
- ...

In the next chapter the main properties and the main features of SiPMs will be described in details.

Chapter 2

Silicon Photomultipliers

In the 1960's a semiconductor-based photodetector with very high internal gain has been developed. This device can detect single photons like a PMT and people began to call it Silicon PhotoMultiplier (SiPM).

A SiPM is a matrix of small avalanche photodiode cells operating a few Volts above the breakdown (GM-APD). In this condition the avalanche produced by ionization is self-sustaining (like in a Geiger counters) and the output signal is independent of the number of electrons which have initiated the Geiger breakdown. This happens because the electric field in the avalanche region is high enough to generate secondary avalanches triggered by holes and (secondary) photons. To turn off the multiplication a quenching resistor must be added in series.

2.1 SiPM working principles

2.1.1 A bit of history

Research on solid state single photon detectors begun in the 60s in the RCA company by Mc Intyre and in the Shockley research laboratory by Haitz, that studied and developed different structures for their devices (figure 2.1). In Japan another model with an horizontal development of the avalanche, was presented in 1972 (figure 2.2).

Improving the technology it was possible to observe the single photon response. The quenching of the breakdown was made passively and it is so still today. Meanwhile, devices with an active quenching was developed to increase the counting rate by a factor 10 [59].

In 1987 the Rockwell International Science Center, Stapelbroek et al. developed the Solid State PhotoMultiplier (SSPM). This is an APD with very high donor concentration. Later this device was modified to be less sensitive to infrared light and is now called Visible Light Photon Counter (VLPC). The small band gap forces an operation at very low temperatures of few Kelvin.

In 1990 in Russia a metal resistor semiconductor avalanche photodiode was invented [60, 61]. Connecting several Geiger Avalanche Photodiodes in

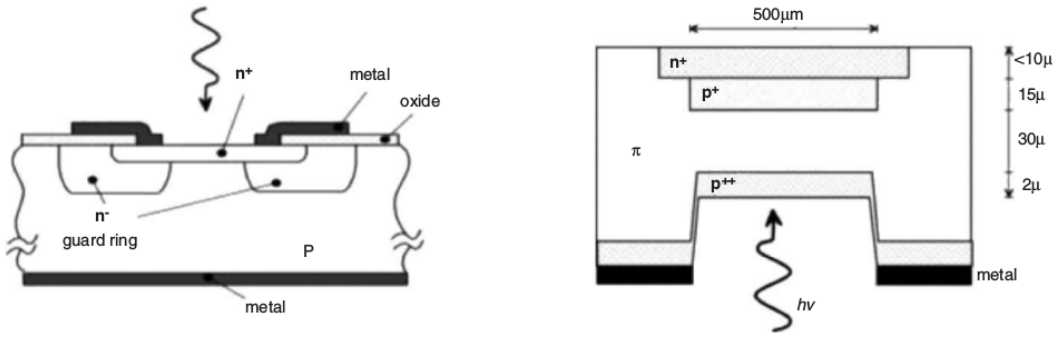

Figure 2.1: The first two silicon single photon detectors. Left is the planar type from Haitz and right the reach through type made by McIntyre [58].

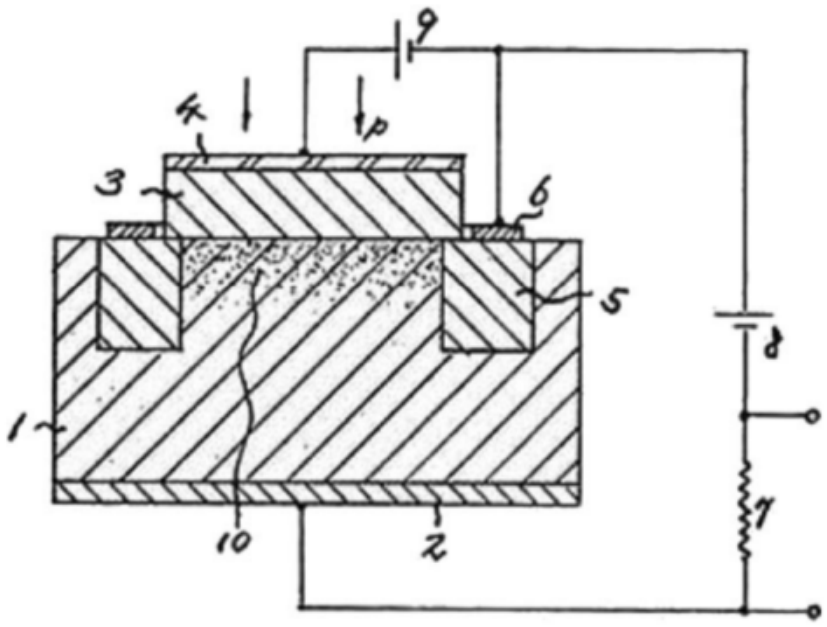

Figure 2.2: Structure of the detector developed in Japan in 1972.

parallel with a quenching resistor in series to each one, a device called Silicon PhotoMultiplier (SiPM) is obtained.

2.1.2 Semiconductor photodetectors

To understand how a Silicon PhotoMultiplier works it is necessary to learn some steps: from the electron-hole pair production to the multiplication process, from the pulse shape formation to the noise signals [62].

A semiconductor is a material with an energy band gap equal to or less than 6 eV. The valence band, associated to the molecular bond, contains the ground state electrons of the atoms; in the conduction band there are excited electrons that can interact with the lattice. Between the two bands there is a forbidden band usually called *bandgap*.

With several techniques it is possible to add into the crystal some impurities that can change the electrical properties of the material. Let's considering the case of silicon that is a tetravalent semiconductor, i.e. with four covalent bonds. Replacing some of them with atoms of the 5^{th} group, like phosphorus or arsenic, let's obtain an excess of electrons (*donors*) that can pass in the conduction band through a thermal excitation as free electrons. In this case, because of the excess of negative charge, the semiconductor is called *n-type*. On the contrary, if the impurities are atoms of the 3^{rd} or 2^{nd} groups (*acceptors*) there is a defect of electrons that is equivalent to an excess of positive charge (that are usually defined as *holes*) and the semiconductor is of *p-type*.

The chemical potential, or the Fermi energy level, of a semiconductor is in the middle of the bandgap. With a n-type doping the Fermi level become closer and closer to the conduction band proportionally to the doping concentration, until the two bands reach the same energy. In this case there is the so called Mott transition and the semiconductor will behave as a metal. On the contrary with a p-type doping the Fermi level become closer to the valence band (figure 2.3).

The simplest semiconductor photodetector is the *photoconductor* (figure 2.4) that is a semiconductor with ohmic contacts at the ends. Applying a bias voltage (V_B) between the electrodes a bias current (I_B) is generated and added to the photocurrent I_{PH} generated by photons that crossed the active volume. Connecting two different doped semiconductors together, a *pn* junction is formed. Around the junction the positive and the negative carriers are concentrated. This is the basis of a *pn* photodiode.

As for a capacitor, there are negative donors (p-region) and positive acceptors (n-region) without free carriers between them. In this region, the *space charge region*, there is an electric field that changes the energy barrier between the regions (figure 2.5). The width of the space charge region decreases with the doping doses while the height of the barrier increases with the doses.

Because of the electric field in that region, the electron-hole pairs cannot recombine (figure 2.6, region 1) and generate a photocurrent that flows in opposite direction with respect the bias voltage (for instance from n to p for

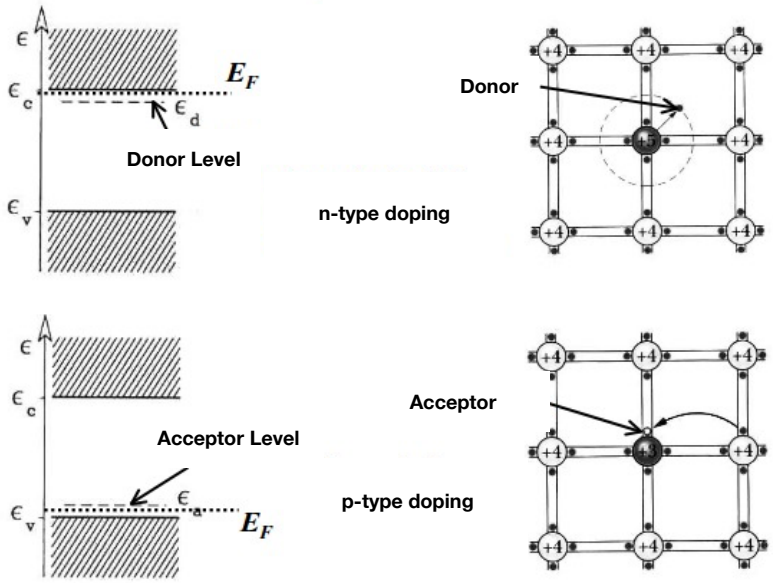

Figure 2.3: Fermi energy level for p-type and n-type dopings.

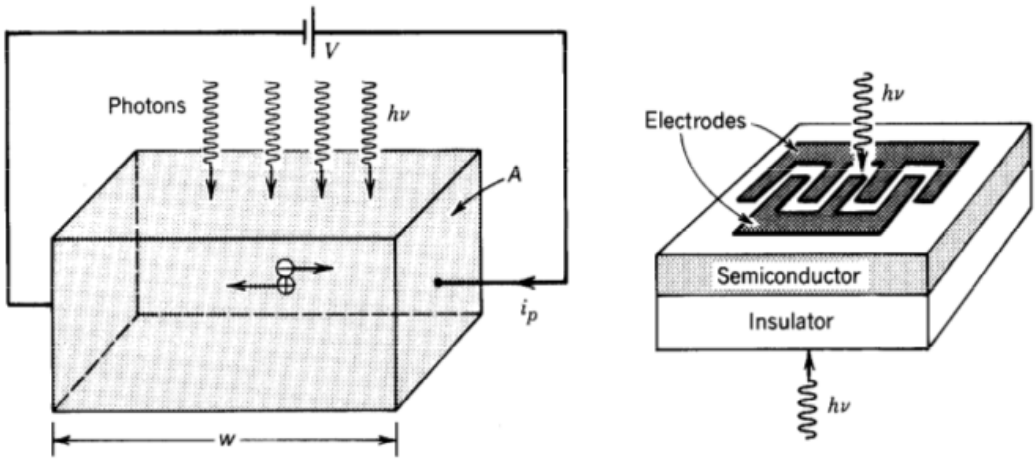

Figure 2.4: Scheme of a photoconductor.

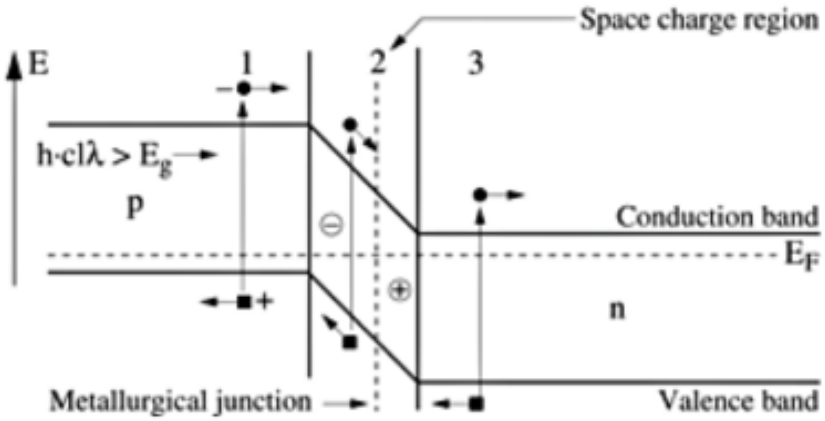

Figure 2.5: Scheme of the energy levels variations due to different dopings.

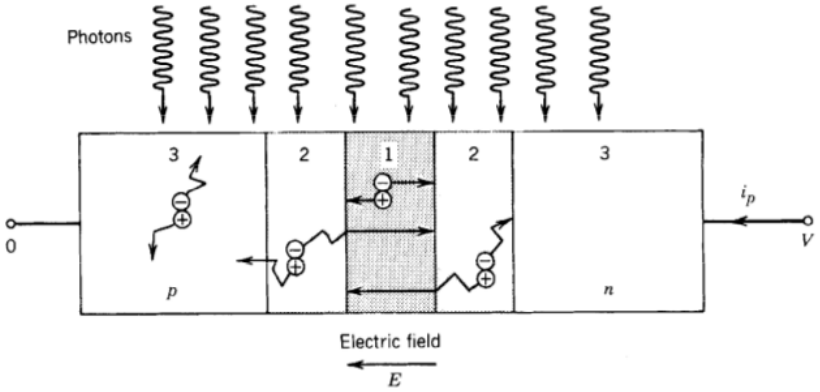

Figure 2.6: Scheme of a pn structure for recombination. See text for details.

electrons). Applying an external potential $V_p - V_n < 0$, an electric field is generated and an increases of the barrier highness and of the space charge region width occur. Furthermore, for a better separation efficiency it is necessary to have a large region in which the *eh* pairs can be produced, to increase the number of carriers, and a good doping level to have an electric field around the junction strong enough to separate the pairs [63].

One of the most used method is to introduce an *intrinsic* layer of semiconductor material, intentionally not doped, between the n and p layers to build the so called *p-i-n* photodiode (figure 2.7).

The *p-i-n* structure offers several advantages:

- increasing the width of the depletion region increases the area available for capturing light;
- increasing the width of the depletion region reduces the junction capacitance and thereby the RC time constant. However the transit time increases with the width of the depletion region;
- reducing the ratio between the diffusion length and the drift length of

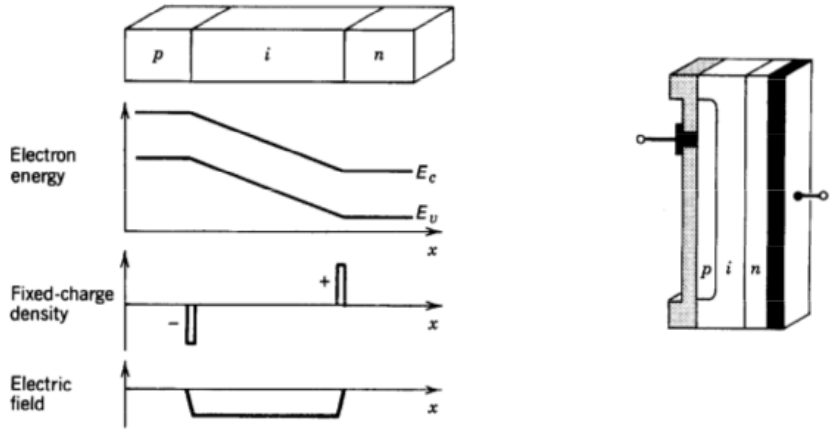

Figure 2.7: P-i-n structure of a photodiode.

the device results in a greater proportion of the generated current being carried by the faster drift process.

Furthermore, if the electric field into the space charge region is strong enough, the carriers interacting with the lattice can generate a secondary ionization of atoms and so, secondary carriers. The consequence of this effect is that the number of carriers generated by a photon is bigger than one, so the device acquires an internal gain.

2.1.3 Avalanche photodiodes

An avalanche photodiode (APD) operates converting each photon in a cascade of moving carriers. The device is a strongly reverse-biased photodiode in which the junction electric field is large. The carriers therefore accelerate acquiring enough energy to excite new carriers by the process of impact ionization.

The working principle is quite easy to understand and it is summarized by the following bullets:

- a photon is absorbed (figure 2.8 point 1), creating an eh pair; an electron in the conduction band and an hole in the valence band;
- electron accelerates under the effect of strong electric field, thereby increasing its energy with respect to the bottom of the conduction band;
- the random collisions with the lattice reduce the acquired energy, but the electron can acquires an energy larger then the gap energy and generates a second eh pair (figure 2.8 point 2);
- each of the two electrons are accelerated by the electric field and can generate other ionizations;
- the entire process can be performed also by holes that can generate secondary ionizations (figure 2.8 point 3).

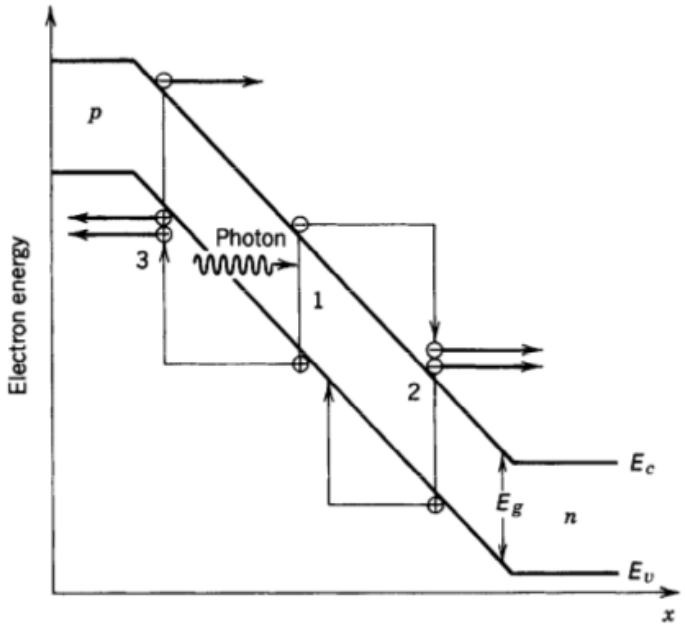

Figure 2.8: Working principles of an avalanche photodiode.

The *ionization coefficients* α_e and α_h represent the ionization probabilities per unit of length; so, the inverse coefficients $1/\alpha$ are the the average distances between consecutive ionizations. The ionization coefficients increase with the electric field, since it provides the acceleration, and decrease with the temperature. In fact, increasing temperature causes an increases in the frequency of collisions, decreasing the free main path.

An important parameter can be defined as the ratio between the ionization coefficients:

$$\mathfrak{h} = \frac{\alpha_h}{\alpha_e}. \tag{2.1}$$

When $\mathfrak{h} \ll 1$ the avalanche is dominated by electrons that moving from the p side to the n side (from left to right in figure 2.8). Similarly to what happens for electrons, happens for holes if $\mathfrak{h} \gg 1$, with the carriers that moving from the n side to the p side.

However, a different case is when $\mathfrak{h} \approx 1$. In this case electrons and holes both ionize appreciably so, for instance, those holes create electrons moving in opposite directions that can generate further holes, in a possibly unending circulation. Although this feedback process increases the gain of the device it is nevertheless undesirable for several reasons:

- it is time consuming and therefore reduces the device bandwidth;
- it is random and therefore increases the device noise;
- it can be unstable, thereby causing avalanche breakdown.

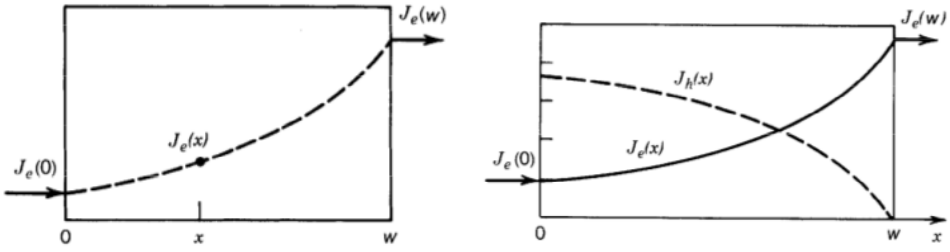

Figure 2.9: Current density of an avalanche photodiode for electrons (a) and for both electrons and holes (b).

It is therefore desirable to fabricate APDs from materials that permit only one type of carrier (either electrons or holes) to generate the avalanche. If electrons have the higher ionization coefficient, for example, optimal behavior is achieved by injecting the electron of a photo-carrier pair at the p edge of the depletion layer and by using a material whose value of $\mathfrak{h}$ is as low as possible. If holes are injected, the hole of a photocarrier pair should be injected at the n edge of the depletion layer and $\mathfrak{h}$ should be as large as possible. The ideal case of single-carrier multiplication is achieved when $\mathfrak{h} = 0$ or $\mathfrak{h} = \infty$.

Gain of APDs

Lets start considering the simpler case in which all the carriers are electrons so, $\mathfrak{h} = 0$. Introducing the electric current density carried by electrons $J_e(x)$ at location x, the increase of J_e within a distance dx is (figure 2.9 a):

$$dJ_e(x) = \alpha_e J_e(x) dx \tag{2.2}$$

where we considered α constant. Integrating the equation 2.2 we obtain:

$$J_e(x) = J_e(0) exp(\alpha_e x); \tag{2.3}$$

defining the gain G as the increment of the current density:

$$G = \frac{J_e(x)}{J_e(0)} = exp(\alpha_e w) \tag{2.4}$$

where w is the width of the multiplication region.

The double-carrier multiplication problem requires knowledge of both the electron current density $J_e(x)$ and the hole current density $J_h(x)$. It is assumed that only electrons are injected into the multiplication region. Since hole ionizations also produce electrons, however, the growth of $J_e(x)$ is governed by the differential equation:

$$\frac{J_e(x)}{dx} = \alpha_e J_e(x) dx + \alpha_h J_h(x) dx. \tag{2.5}$$

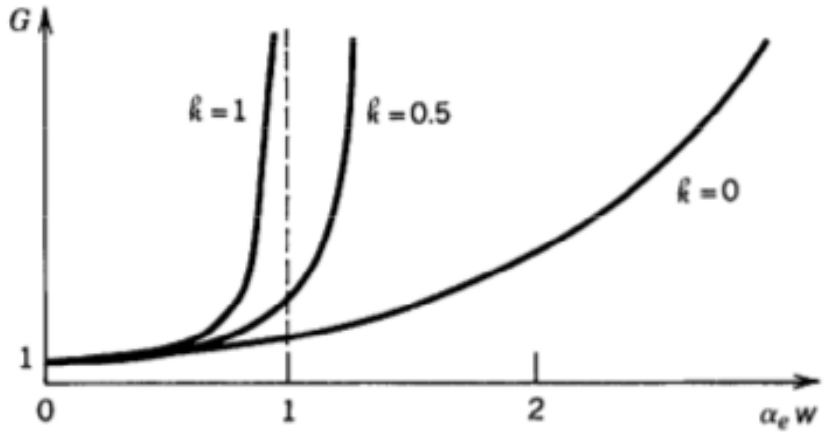

Figure 2.10: Gain of an avalanche photodiode as a function of depth for different value of the hole-electron density ratio.

As a result of charge neutrality,

$$\frac{dJ_e(x)}{dx} = -\frac{dJ_h(x)}{dx},$$

so that the sum $J_e(x) + J_h(x)$ must remain constant for all x under steady-state conditions. Furthermore, since it is assumed that no holes are injected at $x = w$, $J_h(w) = 0$ (figure 2.9 b) so

$$J_e(x) + J_h(x) = J_e(w). \tag{2.6}$$

Combining this equation with equation 2.5 we obtain:

$$\frac{dJ_e}{dx} = (\alpha_e - \alpha_h)J_e(x) + \alpha_h J_e(w) \tag{2.7}$$

that can be solved to obtain the gain:

$$G = \frac{\alpha_e - \alpha_h}{\alpha_e exp[-(\alpha_e - \alpha_h)w] - \alpha_h} \tag{2.8}$$

from which:

$$G = \frac{1 - \mathfrak{h}}{exp[-(1 - \mathfrak{h})\alpha_e w] - \mathfrak{h}}. \tag{2.9}$$

This equation show the gain behavior as a function of $\mathfrak{h} = \alpha_h/\alpha_e$. In the case of $\mathfrak{h} = 0$ the equation 2.4 is obtained. If $\mathfrak{h} = \infty$, $G = 1$ (remember that we are considering the case of an electron injected into the multiplication region). For $\mathfrak{h} = 1$ the gain has to be obtained directly from equation 2.7. Different cases are shown in figure 2.10.

2.2 SiPM characteristics and performance

As described in the previous section silicon photomultipliers work with different physics principles with respect the photomultiplier tubes. This solution offers some advantages, such as the insensitivity to strong magnetic field, but also some disadvantages, like the higher noise rate. Anyway, for some applications, from medical application to high energy physics experiments, SiPMs are replacing the PMTs.

In this section I will discuss all the main characteristics and performance of SiPMs underlying the differences with respect the PMTs and focusing on the application for which this thesis is dedicated.

The behavior of the performance of SiPMs as a function of the temperature will be discuss in detail in the next chapters.

2.2.1 Breakdown voltage

The first of the characteristic I want to describe is the breakdown voltage. This is the most important parameter to be defined for a SiPM because all the features are usually referred to this one.

The breakdown voltage (V_{bd}) is that particular value of the bias voltage for which the Geiger avalanche occurs. This means that for $V_{bias} = B_{bd}$ the electric field into the multiplication region is high enough to generate an uncontrolled avalanche and the current increase quickly. Thanks to the quenching resistance, after the discharge, the correct value of the potential inside that region can be restored and the current decreases.

Usually the working voltage of a SiPM is few volts above the breakdown and that value is commonly named *overvoltage* and defined as

$$V_{ov} = V_{bias} - V_{bd}. \tag{2.10}$$

For the commercial devices the breakdown voltage is between $V_{bd} \simeq 25\ V$ and $V_{bd} \simeq 110\ V$ at room temperature much lower than the bias voltage of a PMT that is above $1000\ V$.

2.2.2 Pulse shape

One of the most important features of a detector is its response to a physical process, in particular the shape of the pulse generated by an event. In the case of a SiPM, for some applications it is important to have a fast signal, especially for timing and trigger purposes.

To understand how a SiPM signal is generated is useful to introduce the equivalent circuits shown in figures 2.11 and 2.12 [68]. As developed by Mc Intrye and Haitz in '60s, a SiPM below the breakdown can be represented as a capacitor C_D in series to the quenching resistance R_q. In this situation, keeping the switch in the OFF position the capacitor can be charged to the

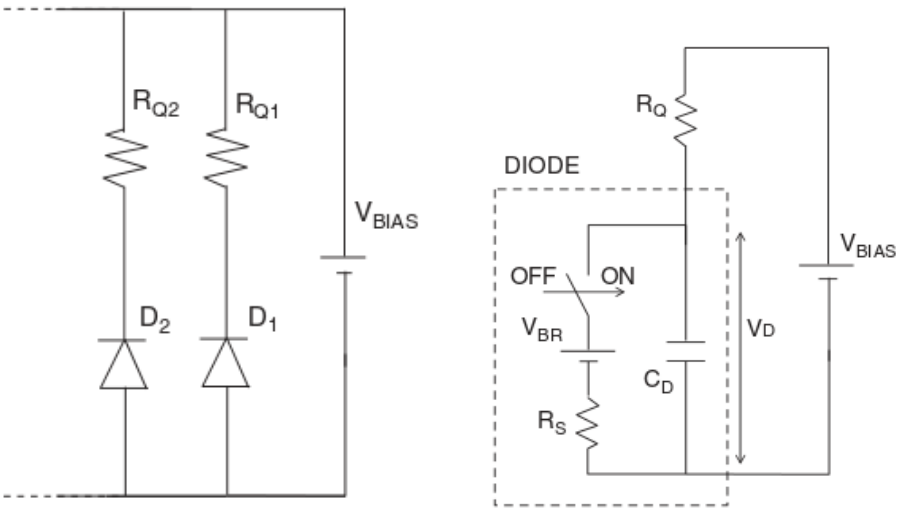

(a) (b)

Figure 2.11: Equivalent circuits of a SiPM. On the left, the APDs with the relative quenching resistors are shown. On the right a detailed view of the equivalent circuit of the APD is shown.

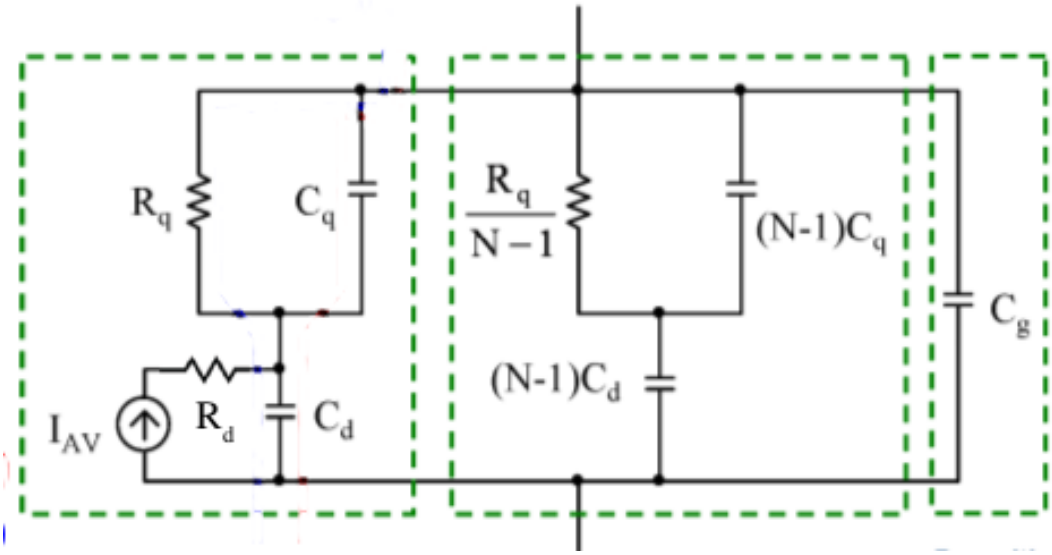

Figure 2.12: Detailed view of the equivalent circuit of a SiPM.

working voltage $V_{bias} > V_{bd}$. When a carrier pass through the multiplication region, with a turn-on probability P_{01} (described in the paragraph 2.2.4 an avalanche can occurs: this corresponds to close the switch. Now the capacitor can discharge through the resistance R_S from V_{bias} to V_{bd} with a time constant of

$$\tau_d^{rise} \sim R_S(C_D + C_Q) \tag{2.11}$$

that define the rise time of the device. So the current that cross through the diode goes from 0 to the asymptotic value:

$$\frac{V_{bias} - V_{bd}}{R_S + R_Q} = \frac{V_{ov}}{R_S + R_Q}. \tag{2.12}$$

The function of $I_D(t)$ during this fase is given by:

$$I_D(t) = \frac{V_{ov}}{R_S + R_Q}\left(1 - e^{-t/\tau_d}\right) \tag{2.13}$$

and, considering $T = 0$ the time when the avalanche occurs, the corresponding voltage is:

$$V_D(t) = V_{bd} + V_{ov}\, e^{-t/\tau_d}. \tag{2.14}$$

Since R_S is of the order of $k\Omega$, R_Q has to be of the order of few hundreds of $k\Omega$. In this way, the diode current is small enough that just for a statistical fluctuation it is possible to stop the carrier coming into the multiplication region and stop the avalanche. When the avalanche is stopped the switch is opened again, the capacitor C_D is recharged at the potential V_{bias} with time constants of

$$\tau_{fast}^{fall} = R_{el}C_{tot} \tag{2.15}$$

$$\tau_{slow}^{fall} = R_Q(C_D + C_Q) \tag{2.16}$$

where R_{el} and C_{tot} are the electronic impedance and the total capacitance of the system. This two equations represent the fast and the slow components of the signal respectively. Now the current return to 0:

$$I_D(t) \simeq \frac{V_{ov}}{R_s + R_Q} e^{-t/\tau^{fall}} \simeq \frac{V_{ov}}{R_Q} e^{-t/\tau^{fall}}. \tag{2.17}$$

During the discharge it is possible to calculate the signal as a function of time $V(t)$:

$$V(t) \simeq \frac{Q_{tot}}{C_Q + C_D}\left(\frac{C_Q}{C_{tot}} e^{-\frac{t}{\tau_{fast}}} + \frac{R_{el}}{R_Q}\frac{C_D}{C_Q + C_D} e^{-\frac{t}{\tau_{slow}}}\right) \tag{2.18}$$

where $Q_{tot} = (C_Q + C_D)\Delta V$ is the total charge produced by a cell during the avalanche.

2.2.3 Gain

The gain of a SiPM is of the order of 10^6, comparable to the PMT gain and it is defined as the charge produced by a single photon in electron charge units:

$$G = \frac{Q_{tot}}{q} = \frac{1}{q}\int_0^\infty I_D(t)dt \tag{2.19}$$

where $q = 1.602 \times 10^{-19}\ C$ is the electron charge, I_D is the diode current expressed by the equation 2.17. By inserting the equation 2.17 in the approximated form, into the equation 2.19 we obtain:

$$G = \frac{V_{ov}}{qR_Q}\int_0^\infty e^{-\frac{t}{R_Q C_D}}dt = \frac{C_D}{q}V_{ov} = \frac{C_D}{q}(V_{bias} - V_{bd}). \tag{2.20}$$

As shown the gain is proportional to the bias voltage, however the noise limits the working voltage to avoid to loose the linearity.

2.2.4 Photon detection efficiency

The photon detection efficiency (PDE) is the capability of a SiPM to detect a photon and to generate a pulse signal. It is defined as a product of three quantities:

$$PDE = QE(\lambda) \times FF \times P_{01} \tag{2.21}$$

where QE is the quantum efficiency, FF is the fill factor and P_{01} is the turn-on probability. All this quantities are described below.

The quantum efficiency, that is a function of the wavelength λ of the incoming photon, is the probability of a photon to generate an electron-hole pair into the space charge region able to reach the multiplication region (figure 2.13a).

The fill factor is the ratio between the active area, i.e. the sum of the area of each cell, and the total surface of the device. In fact, because of the quenching resistors, the metallic support of each cell and the trenches between the cells, i.e. a barrier that limits the cross-talks, the total surface is bigger than the active one (figure 2.13b). For instance the FF is of the order of 40-50%.

The P_{01} (figure 2.13c) is the probability that a free carrier coming into the multiplication region generates an avalanche.

2.2.5 Noise

In dark condition, when no photons can reach the device, a SiPM can generate spurious signals due to the impurities into the lattice. So, a noise signals rate, of the order of few kHz at room temperature has to be considered.

It is possible to recognize three kinds of noise:

- the *Dark Counts Rate* (DCR);
- the *optical cross-talks*;

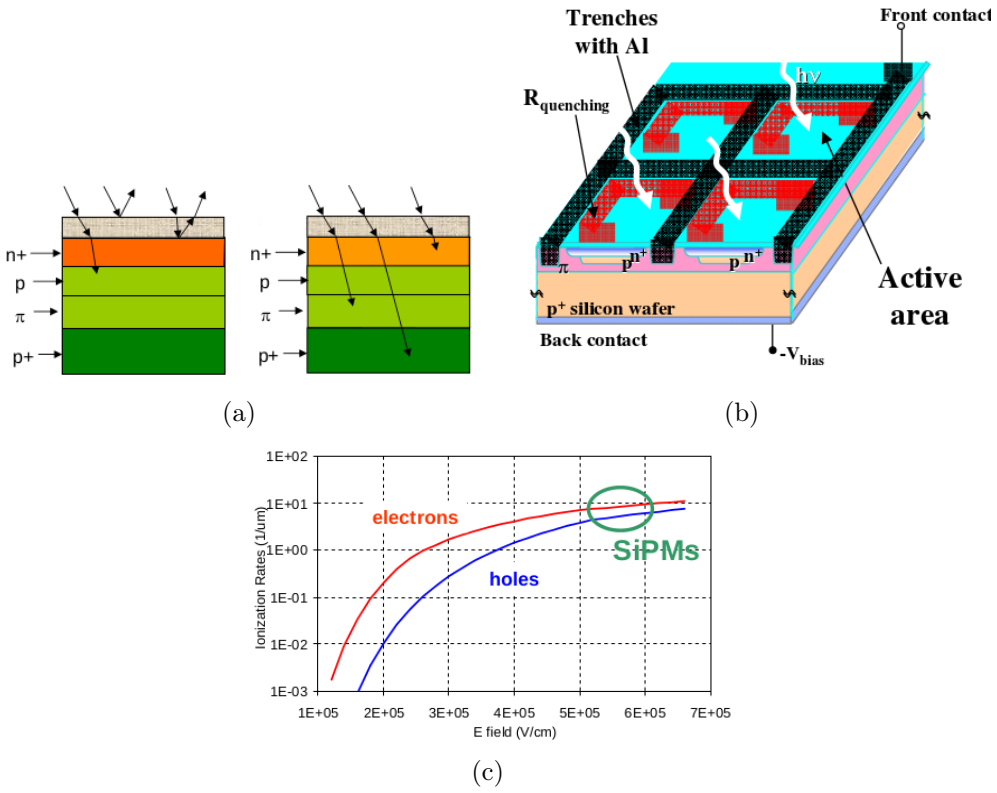

Figure 2.13: The three components of the PDE are shown: the quantum efficiency (a), the fill factor (b) and the P_{01} probability (c). See text for more details.

- the *afterpulses*.

In the following paragraphs all the noise types are discussed in detail.

Dark counts rate

Into the depleted region an electron-hole pair can be produced by thermal agitation mechanisms or a free electron can be generated due to the high electric field. If the generated carrier produces an avalanche, at the output of the device a pulse signal is produced with the same characteristics of a signal produced by a photon. For this reason, in principle, it is not possible to distinguish a dark count from a photon signal. Furthermore dark count events can have amplitudes twice or even several times higher than the amplitude of a single cell breakdown. The responsible effect is the optical crosstalk.

Optical cross-talk

During the avalanche there is a small probability of about 3×10^{-5}, that a secondary photon with energy $E > 1.14\ eV$ is produced. This photon is free

to escape from the fired cell and can cross one of the closest cells. In this case the secondary photon can generate a signal. So, since this is a prompt process, the total signal has twice the standard amplitude and can be confused as a signal produced by 2 photons.

Several models were suggested in the past for explaining the light emission, for example, bremsstrahlung and a multimechanism scenario, including indirect and direct interband and intra-band transitions. The optical crosstalk acts like shower fluctuations in an APD. It is a stochastic process and introduces an excess noise factor F as in a normal APD or in a PMT. Neglecting saturation effects and contributions from afterpulses and dark counts in the wide gate needed for the measurement of light from a scintillating crystal F can be approximated:

$$F \approx 1 + p_{ct}. \tag{2.22}$$

The probability p_{ct} is defined by the rate of dark count events with crosstalk (threshold 1.5 fired cells) divided by the total dark count rate (threshold 0.5 fired cells).

With a dedicated design, which has an additional junction and with grooves between the cells, which act as an optical isolation, the optical crosstalk can be reduced. Operation at relatively low gain is advantageous to reduce optical crosstalk, albeit with the disadvantage of reducing the PDE significantly. A quite convenient alternative method to suppress optical crosstalk is to insert narrow grooves between cells and fill them with an optical absorber. The disadvantage is the need for space reducing the active area, i.e. reducing the filling factor and, in turn, the PDE.

Afterpulses

The afterpulse is a kind of noise correlated to a primary signal generated by a photon or a dark signal.

The signal is produced by a secondary avalanche generated, during the primary multiplication, by a carrier released by a meta-stable energy band between the valence and the conduction bands. In fact, it is possible that during the avalanche a carrier is trapped into this meta-stable band and released with a delay of the order of nanoseconds. When this carrier is released into the multiplication region, the primary avalanche has been finished but the electric field is still restoring its nominal value. Because of this, the afterpulse signal is smaller than the one-photon signal. The probability $P(t)$ to have afterpulsing as a function of time is:

$$P(t) = P_{cap} P_{01} \frac{exp(t/\tau)}{\tau} \tag{2.23}$$

where P_{cap} is the probability for a carrier to be captured by a trap, P_{01} is the already known turn-on probability and τ is the lifetime of the trap.

Chapter 3

SiPM performances as a function of temperature

In the previous chapter, an introduction to the Silicon PhotoMultiplier (SiPM) operational principles have been described. In this chapter I will focus the description on the performance of different SiPM models as a function of temperature. The final goal of this research is to apply the SiPM technology to liquid argon Time Projection Chamber (LAr-TPC), therefore the main features we are interested in are the gain, the breakdown voltage, the noise and the time characteristic of the signal pulse.

3.1 Experimental apparatus

The first step to answer the question if SiPMs can be efficiently used in LAr-TPCs is to verify their performance at the liquid argon temperature. For this purpose I developed and refined an apparatus to measure several SiPMs as a function of temperature and some experimental setups to measure the time features of SiPM pulses and the quantum efficiency at different wavelengths. In this section I will describe all the used systems.

3.1.1 The cold head

Lets start describing the main system that allows to compare the performance of SiPMs as a function of temperature: the *cold head*. This system is used to test SiPMs of $3 \times 3\ mm^2$ and $1 \times 1\ mm^2$ in terms of breakdown voltage, quenching resistance, gain, noise and relative quantum efficiency. All the results and the comparison between the different models will be shown in the following sections. The system (figures 3.1 and 3.2) is composed by a cryogenic pump model Helix Cryo-Torr 8F terminated with a cylindrical copper head connected to a closed helium circuit. The thermodynamic cycle able for lowering the temperature is the so-called *Gifford Mac Mahon*, that using the helium expansion at constant pressure, cools down the copper cylinder. Above the cryogenic pump, a vacuum chamber connected through a CF200 flange

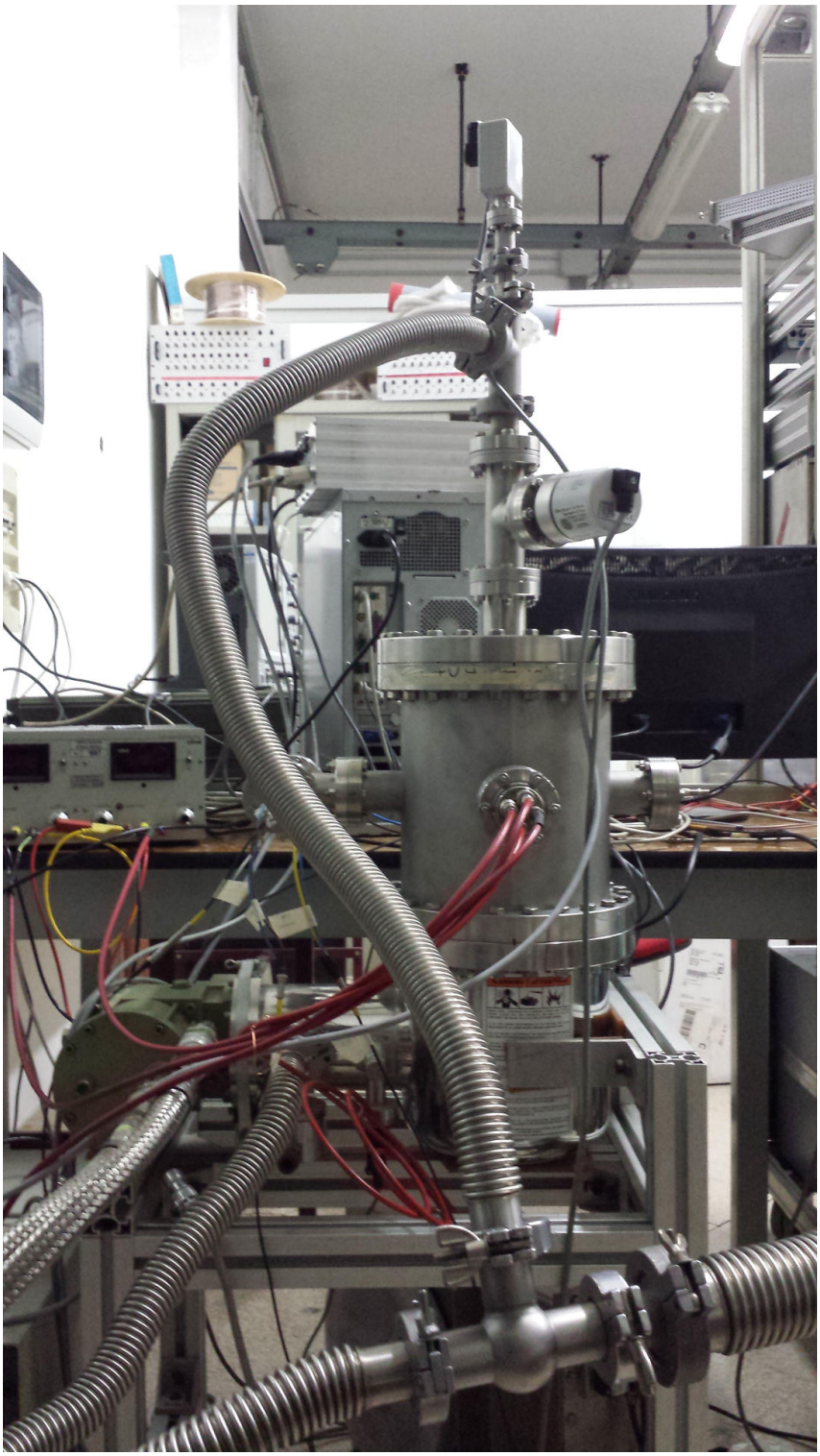

Figure 3.1: Photo of the cold head system placed at the INFN and University of Pavia laboratory.

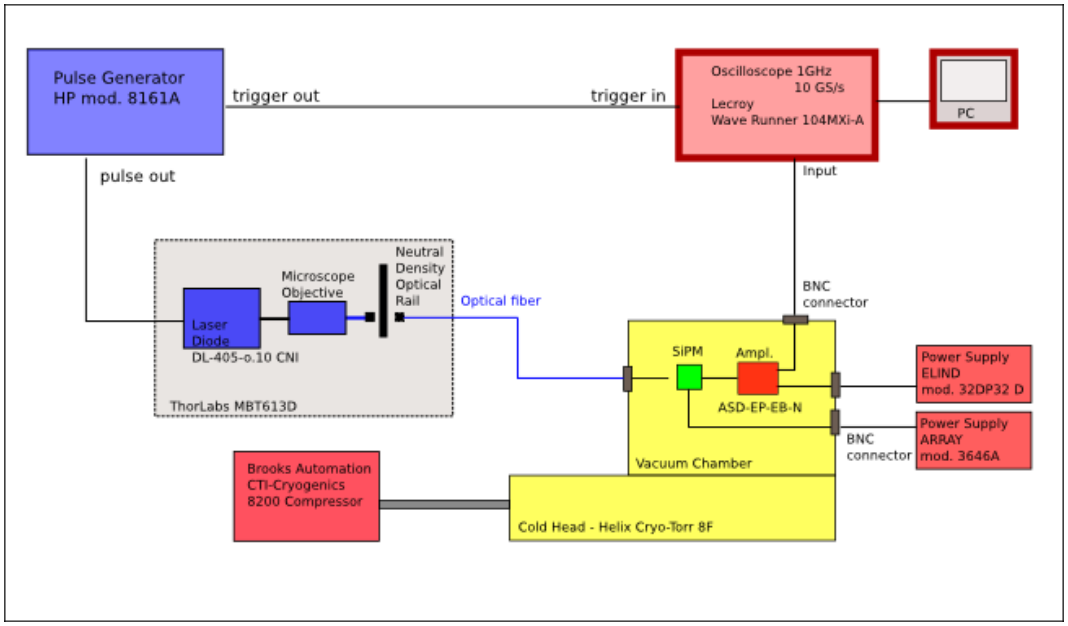

Figure 3.2: Sketch of the cold head apparatus. Power supplies, data acquisition system and pulse generator are shown.

has been mounted. Inside, a copper cylinder has been connected with the cold head. This is the part of the apparatus dedicated to housing the device under test. In particular, the last 10 cm of the cylinder can be screwed and unscrewed to facilitate the positioning of the device in a dedicated groove where the SiPM support can be fixed precisely (figure 3.3). Then a copper hat covers the device and a SMA-type optical connector is positioned in front of the active area of the device. This setup allows to uniformly illuminate the entire device. Three temperature sensors PT1000 were placed inside the chamber in contact with the cylinder as shown in figure 3.4: several tests have been performed to verify the cooling curve of the cylinder as a function of the distance from the basis, to correct the heat dispersion due to the cylinder length, the mechanical connections and so on. The SiPM support is made by a silicon layer with two metallic strips where the SiPM anode and cathode can be welded. On the other side, a pins connector is used to propagate the signals. In some cases the signal is directly analyzed, in other cases, before the analysis, the signal pass through a pre-amplifier. The pre-amplifier is an AdvanSiD trans-impedance pre-amplifier model ASD-EP-EB-N that has to be biased at $\pm 5\ V$, guaranteed by an ELIND 32DP32-D power supplier. To maintain its temperature around 300 K, the pre-amplifier is positioned few centimeters far from the cold head with an isolated support. The entire sets of cables for the biases, the sensors and the optical fiber comes into the vacuum chamber through few CF35 flanges. The light, as already mentioned, reaches the SiPM under test with a series of optical fibers. An HP 8161A pulse generator it is used to pilot a $\lambda = 405\ nm$ laser diode CNI DL-405-0.10 (an example of the pulse features are

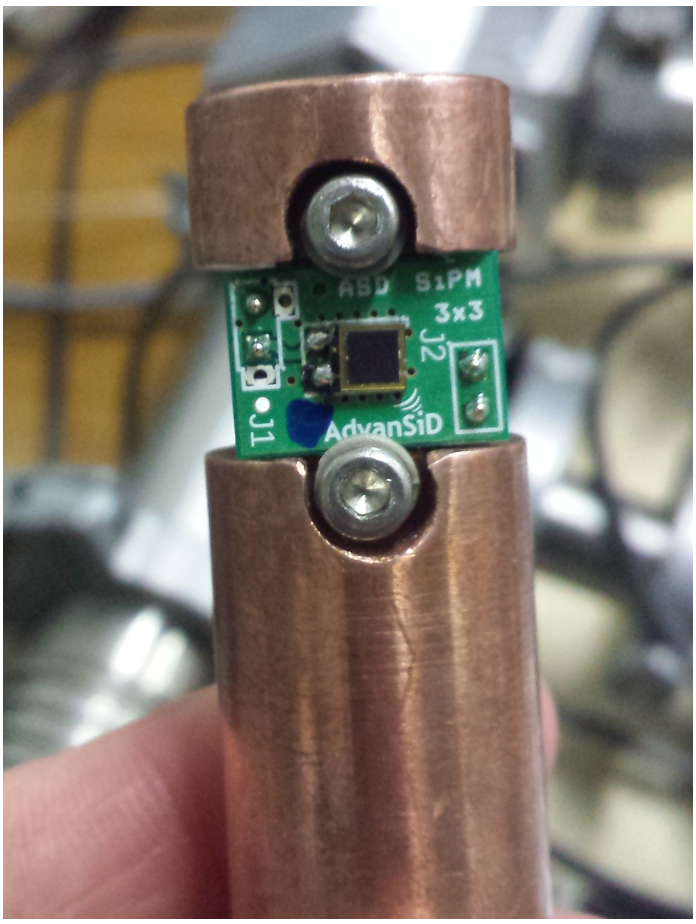

Figure 3.3: Photo of the final part of the cold head with the SiPM placement. In this case, an AdvanSiD 3×3 mm^2 NUV is placed in a dedicated support (socket). Two screws allow to keep the device under test in the correct position.

shown in table 3.1). A passive light attenuator can be used to set the amount of light required by the test.

The vacuum system

A vacuum system (figure 3.5) is used to prevent condensation phenomena, heat dispersion and heat propagation inside the chamber. Furthermore, an high vacuum level guarantees a better electrical isolation with respect to the standard pressure conditions. A rotative primary vacuum pump VARIAN model SH01001UNIV it is connected to a turbo-molecular V70 LP Macro Torr. The combination of these two pumps with the cryogenic system allow to reach,

Table 3.1: Main features of the laser source.

λ	HV	Width	Leading Edge	Trailing Edge	Period
405 nm	3.9 V	2 ns	1 ns	1 ns	5 ms

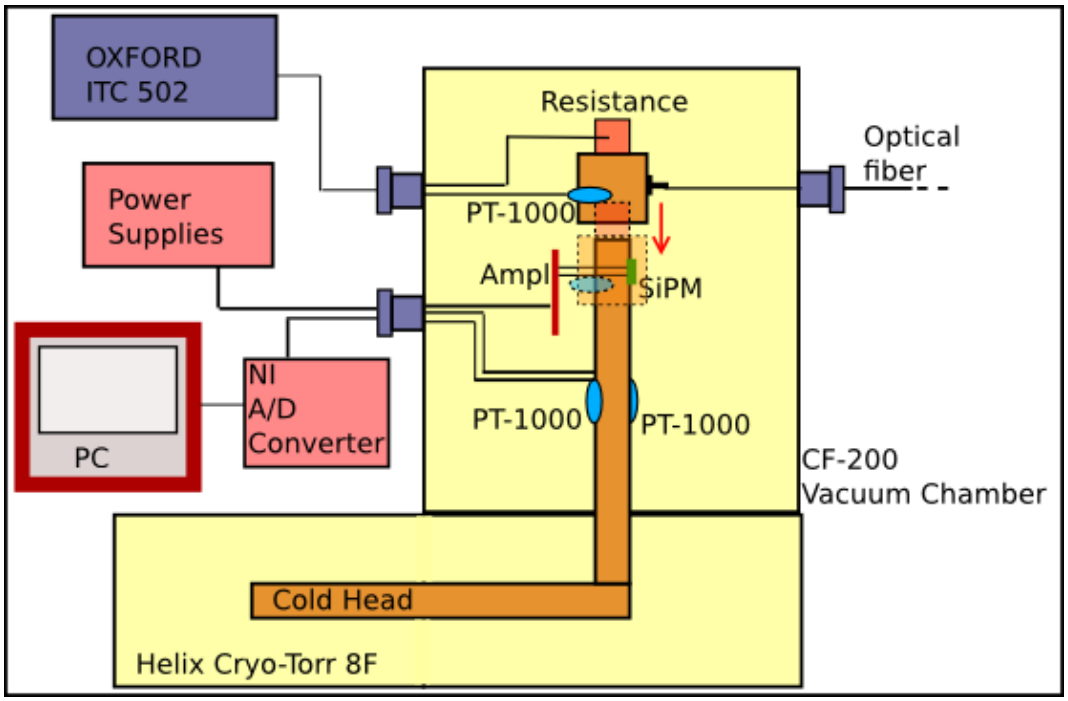

Figure 3.4: Detailed view of the inner part of the system. The temperature sensors, the SiPM, the pre-amplificator and the copper cap needed to place the optical fiber in front of the SiPM active surface are shown.

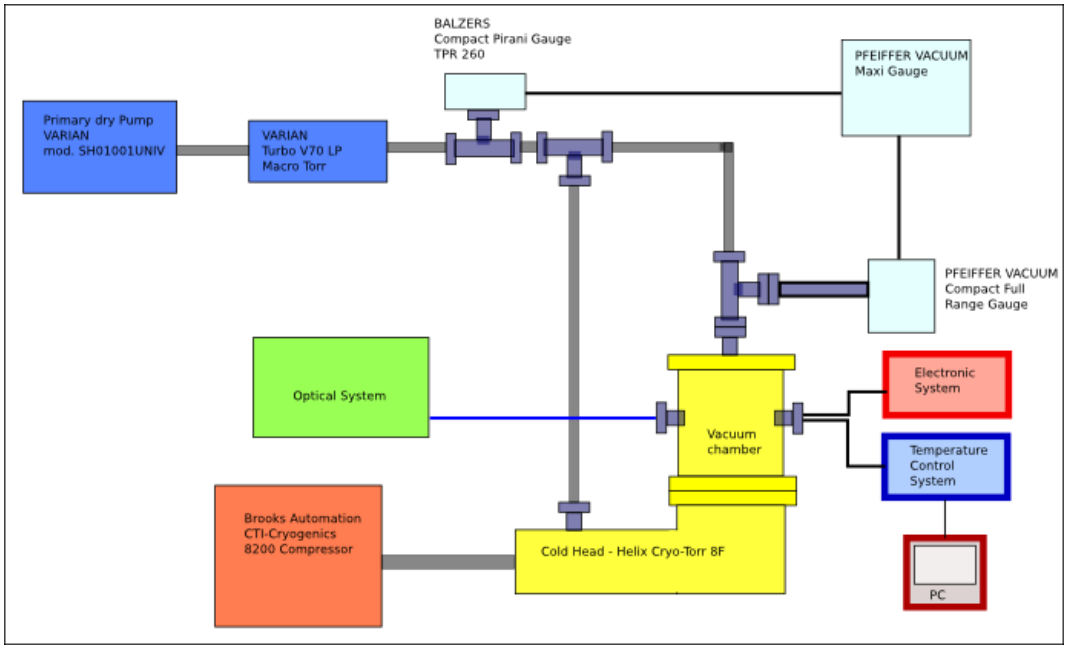

Figure 3.5: Sketch of the apparatus vacuum system.

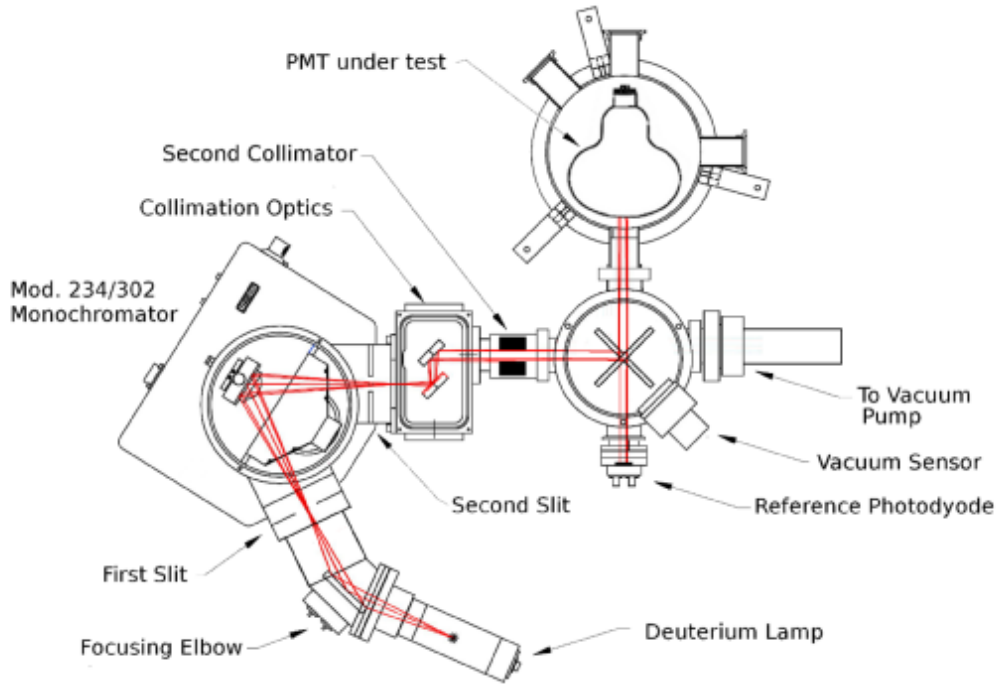

Figure 3.6: Scheme of the monochromator apparatus. In red the light trajectory from the lamp to the device under test or the reference photodiode is shown.

at low temperatures, a pressure of $p \sim 10^{-6}$ $mbar$. Two PFEIFFER Pirani TPR 260 and PFEIFFER PKR 251 vacuum gauges measuring the pressure inside the chamber and they are connected to PFEIFFER Maxi Gauge TPG 256A controller.

3.1.2 The VUV absolute Quantum Efficiency measurement system

The system shown in figure 3.6 allows to measure the quantum efficiency of a photo-device as a function of the wavelength and it is composed by:

- a Deuterium lamp McPHERSON mod-632 which features a front Magnesium Fluoride window (table 3.2) with the emission curve shown in figure 3.7;
- a focusing system which allows to focus the light to the monochromator. Focusing is realized by an UV reflecting mirror. In this way chromatic aberration effects are removed;
- a monochromator model McPHERSON 234/302 (table 3.3): the light gets into the monochromator through a first slit which allows to calibrate its intensity. A diffraction grating (1200 ridges/mm) and a second slit permit to select the light wavelength and to regulate its range amplitude;

Table 3.2: Characteristics of the monochromator apparatus.

Lamp type	Deuterium
Wavelength Range	115-380 nm
Power	30 W
Plasma size	1 mm diameter
Windows material	Magnesium Fluoride
Lifetime	1000 hours
Diffraction grating	1200 ridges/mm

Table 3.3: Optical characteristics of the monochromator system.

Focal length	$200 + 200$ mm
f/number	4.5
Resolution	0.05 nm
Dispersion	1.8 nm/mm
Accuracy	0.1 nm
Base vacuum	1×10^{-6} torr

- a scan controller McPHERSON 789A-3 to control the monochromator from a personal computer via a RS-232 connection;
- two collimators: the former is a reflecting collimator which stabilizes the light beam dimension and its divergence, the latter is composed by an hollow black cylinder (41 mm external diameter, 6 mm internal diameter, 30 mm length);
- a rotative mirror ACTON 1200-FS-2D that allows to select the delivering of the light beam toward one of the two contiguous chambers: the one containing the device under test or the one containing the calibrated photodiode for reference;
- a reference UV photodiode IRD (International Radiation Detector) AXUV-100G calibrated by the National Institute of Standard and Technology (NIST) as a function of wavelength. In figure 3.8 the light yield efficiency as a function of wavelength is shown. Data are given by NIST and the fit has been done with a polynomial equation;
- a vacuum chamber where it is possible to place the device under test that can be fixed to a rotating support to modify the incidence angle of light on the device surface;
- a vacuum system composed by a primary vacuum pump VARIAN SH0-100 connected to a turbo-molecular pump VARIAN Turbo V-70-LP and a EDWARDS Active Gauge AIM-S-NW25 to measure the vacuum level.

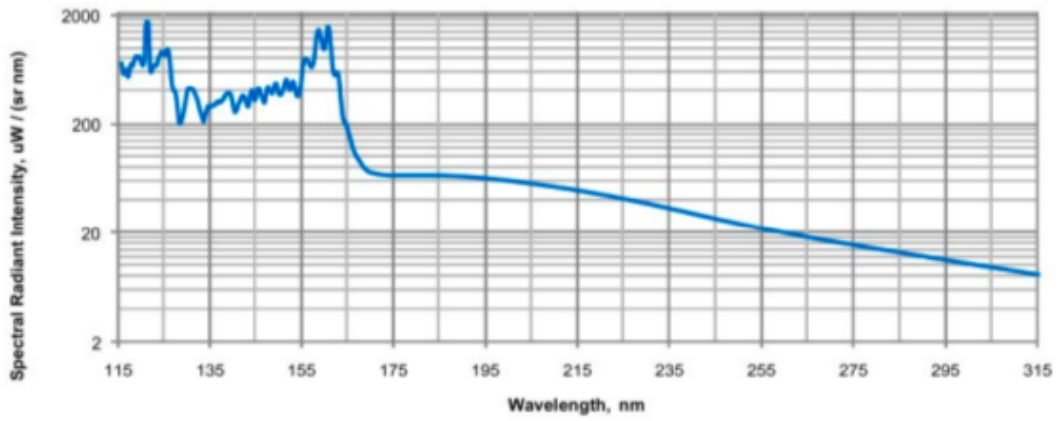

Figure 3.7: Spectrum of the intensity of the Deuterium lamp as a function of wavelength.

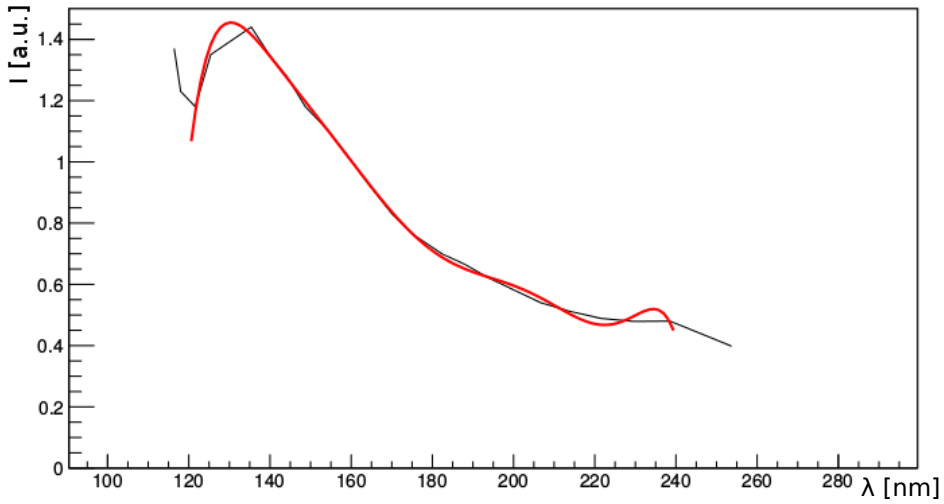

Figure 3.8: Current as a function of wavelength for the reference photodiode. The red line is a polynomial fit.

Beside the monochromator, a picoammeter Kerthley mod.617 connected via a GPIB connector with a computer allows to measure the current of the devices. The picoammeter and the monochromator are controlled with a Labview program which allows to acquire the current informations as a function of the wavelength. In figure 3.8 the current vs wavelength for the calibrated photodiode is shown. Furthermore, a polynomial fit is used to correct the measure performed with the devices under tests.

3.2 Test as a function of temperature

In this section, the description of the possible tests which can be performed as a function of temperature will be presented. The experimental apparatus used for these tests is the Cold Head described above. The setup and the configuration of the cold head have been changed during the three years of my Ph.D. to improve the performance, in particular to reduce the electronic noise, and to adapt the system to study different SiPM models and configurations (the different configurations will be described in details in chapter 4). In the following paragraphs the comparison between some SiPM models will be described analyzing the differences and highlighting the best features for our purposes.

3.2.1 Breakdown voltage and quenching resistance as a function of temperature

Working with SiPMs, the breakdown voltage is the main SiPM feature to be known, because of its dependence with the temperature. As mentioned in the paragraph 2.2.1 the breakdown voltage represents the "starting point" for a SiPM working region. At that voltage value an uncontrolled Geiger-like multiplication of carriers begins. From the experimental point of view, to measure the breakdown voltage, several techniques are possibles [64]. Usually, the SiPM under test is maintained in dark conditions and the I-V curve in reverse-mode bias is measured. In this way, the dark current, at room temperature, is high enough to be measured and used to calculate the breakdown voltage. At cryogenic temperature the dark current decreases drastically because it is due to thermal agitation of the lattice which is proportional to the temperature. So, the I-V curve in dark condition become almost useless to observe the breakdown voltage. For this reason I chose to measure the I-V curve under low light pulse intensity condition. To maintain the same experimental condition I chose to use the same light intensity at different temperatures, for each test. For this test, the experimental setup does not requires the amplification system of the signal, so, the pre-amplifier has been removed and the SiPM signal has been directly detected. The bias voltage and the signal can be transmitted with a single cable to reduce the noise. The picoammeter provides the bias and the GPIB connection with a computer allows to acquire data. A Labview program

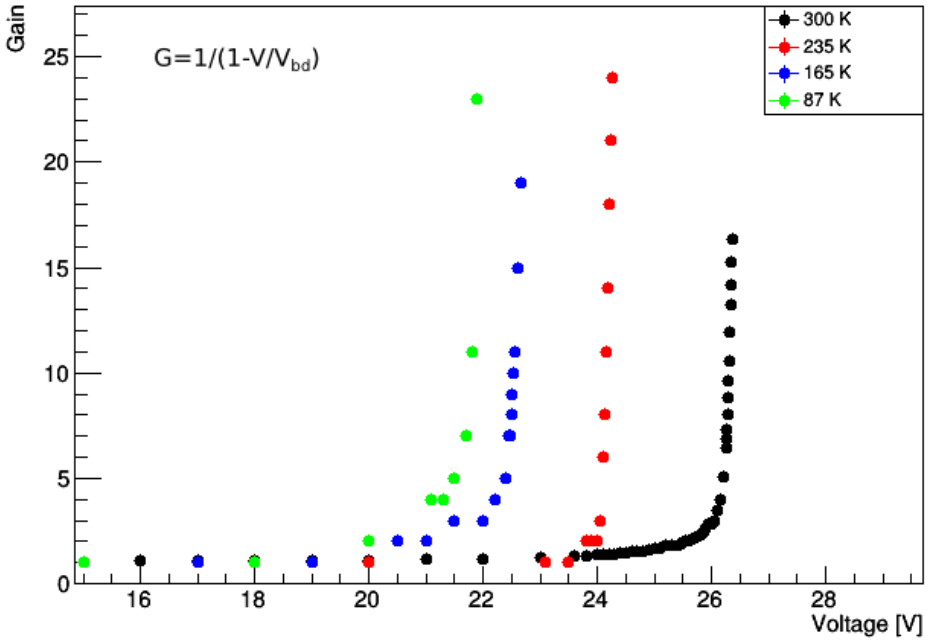

Figure 3.9: APD cells gain as a function of bias voltage at different temperatures for an AdvanSiD NUV SiPM model.

automatically measures both voltage and current as a function of bias, from $V = 0\ V$ up to few volts above the breakdown voltage. In the meantime, it can also monitor and record the temperature measured with the PT1000 sensors. The "stop" is calculated setting a current limit around few μA per cell. After that, I adopted an algorithm to calculate the breakdown voltage that is based on the calculation of the derivative of the logarithmic I-V curve and the search of a maximum of the second derivative. During the cooling down of the system, taking almost 4 hours to reach the temperature of 60 K, the Labview program measured every 10 minutes the I-V curve. Some of them are shown in figure 3.9 in the case of the SiPM model AdvanSiD NUV with an active area of $3 \times 3\ mm^2$. The breakdown voltages calculated from that curves, as a function of the temperature, are shown in figures 3.10 and 3.11. I used this setup to measured the breakdown voltages of several devices of different manufactures and different active surfaces. In particular, the most interesting results come from three devices: the AdvanSiD NUV and RGB technologies and the Hamamatsu s12571. During the first year of my Ph.D. I studied these devices both in the configuration of $1 \times 1\ mm^2$ and $3 \times 3\ mm^2$ in view of the realization of a SiPM test-array that will be better exposed in the following chapter. In table 3.4 the main features of the SiPM model I tested are shown. Even if I tested many other different SiPM models as Ketek, Excelitas and SenSL in terms of breakdown voltages, I chose to exclude them from the results exposed in this thesis because all of them were discarded for different

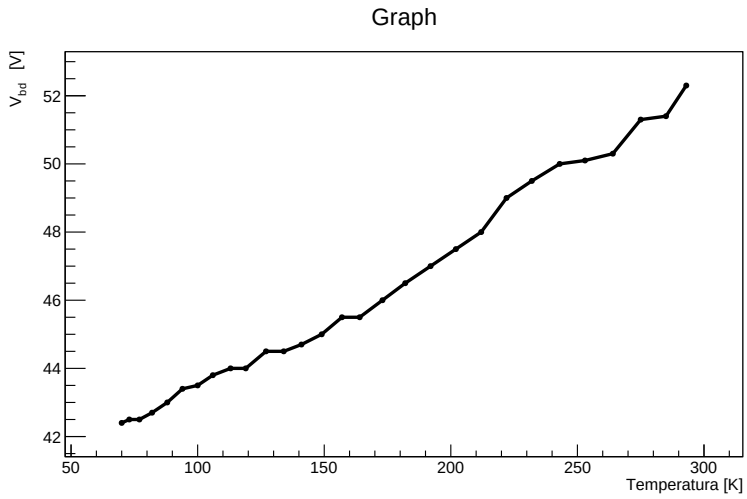

Figure 3.10: Breakdown voltage as a function of temperature for the Hamamatsu s13360 SiPM ($1 \times 1\ mm^2$).

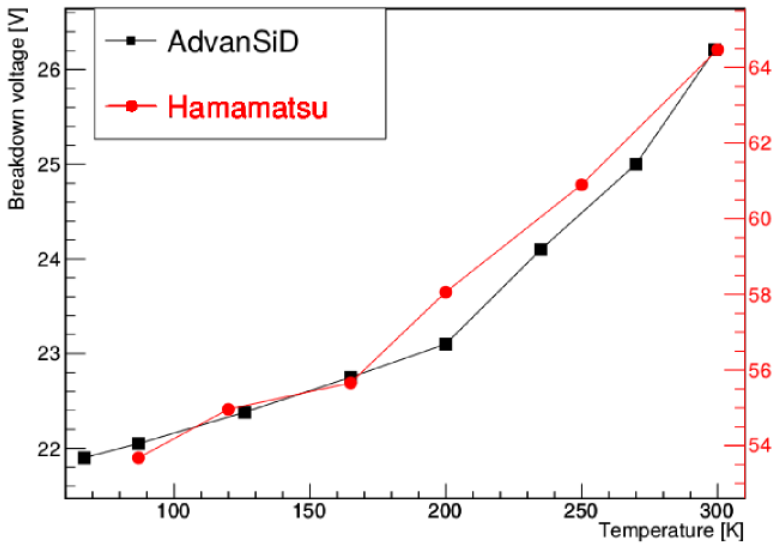

Figure 3.11: Breakdown voltages as a function of temperature for the Hamamatsu s12572 (red) and AdvanSiD NUV (black) SiPMs models. Both these devices have an active area of $3 \times 3\ mm^2$.

Table 3.4: Comparison between some characteristics of three SiPM models.

	ASD-NUV1S-P	ASD-RGB1S-P	HPK s12571
Active Area	$1 \times 1\ mm^2$	$1 \times 1\ mm^2$	$1 \times 1\ mm^2$
Cell size	$40\ \mu m$	$40\ \mu m$	$50\ \mu m$
Fill factor	60 %	60 %	62 %
Typical V_{bd}	$26\ V$	$27\ V$	$65\ V$
Temp. Coeff. ($300\ K$)	$26\ mV/°C$	$27\ mV/°C$	$60\ mV/°C$

reasons: the value of the breakdown voltage too high, the anode and cathode contacts hard to weld on the support and their higher cost. All these features are important to take under consideration in view of a realization of an array of SiPM in the configuration exposed in the following chapter. For this reason the AdvanSiD devices could be the better choice thanks to the low working voltage (below 30 V).

Quenching resistance

Few words about the behavior of the quenching resistance as a function of temperature are mandatory. The quenching resistor (R_Q) passively terminates Geiger discharge in a microcell. Its value affects the amplitude of a single photoelectron current pulse and, together with the junction capacitance, the recovery time. If the value of R_Q were to fall below a certain threshold, quenching would not have occurred, leaving the microcell in the state of a permanent Geiger discharge and insensitivity to light. The value of R_Q can be measured from the forward-bias I-V curve. As the bias increases, the current eventually becomes linearly proportional to the applied voltage because, as the resistance of the depletion region in the APDs approaches zero, only R_Q's limit the current (figure 3.12). Consequently, the slope of the linear section equals N_{cells}/R_Q, where N_{cells} is the total number of microcells. Fitting for the slope and knowing N_{cells} gives R_Q. The I-V curves obtained at different temperatures yield information on how R_Q varies with T. What I found, as shown in figure 3.13, is that R_Q increases at decreasing temperature, causing an increases of the recovery time. So, the lower is the temperature, the slower is the recovery time. This fact can, of course, generates problems for timing and triggering applications in which a fast signal allows to avoid pile-ups events.
Furthermore, the variation of R_Q is strongly dependent by its material. For polysilicon resistors the temperature decreasing causes an higher increase of the resistance at cryogenic temperature with respect to the metallic one. In this case, the Hamamatsu devices can be the best choice.

3.2.2 Gain as a function of temperature

The gain of a device plays a crucial role in low intensity photon experiments. SiPMs are semiconductor devices with gains of the order of 10^6. This property guarantees the capability to detect the single photon, like photomultiplier tube (PMT). However, the performance of PMTs in cryogenic condition change drastically, especially in terms of gain. For instance, the gain of the Hamamatsu R5912-mod, the ICARUS PMT model installed during the last refurbishing of the detector, in cryogenic condition decreases of about 70% of the value at room temperature. This behavior is caused by mechanical modification due to the different thermal conditions. To restore the original gain value it is necessary to increase the bias voltage of $\sim$ 300 V [65]. Because

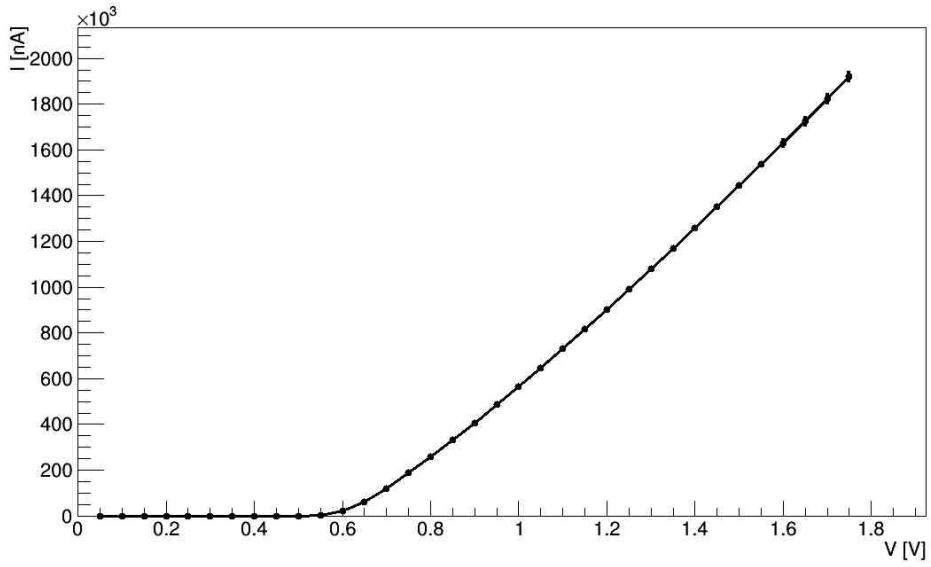

Figure 3.12: I-V curve of a Hmamatsu s12572-050P at room temperature acquired with direct bias to measure the quenching resistance.

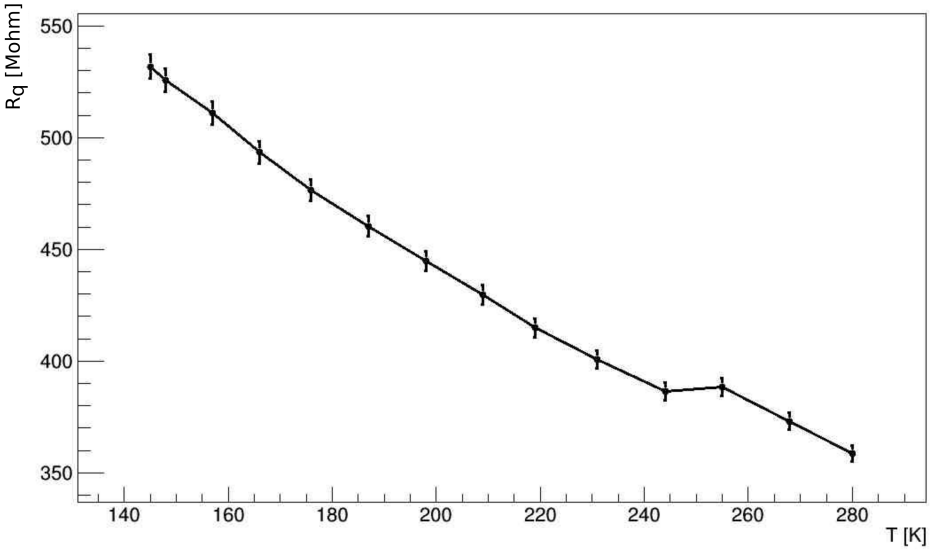

Figure 3.13: Quenching resistance as a function of temperature for an Hmamatsu s12572-050P.

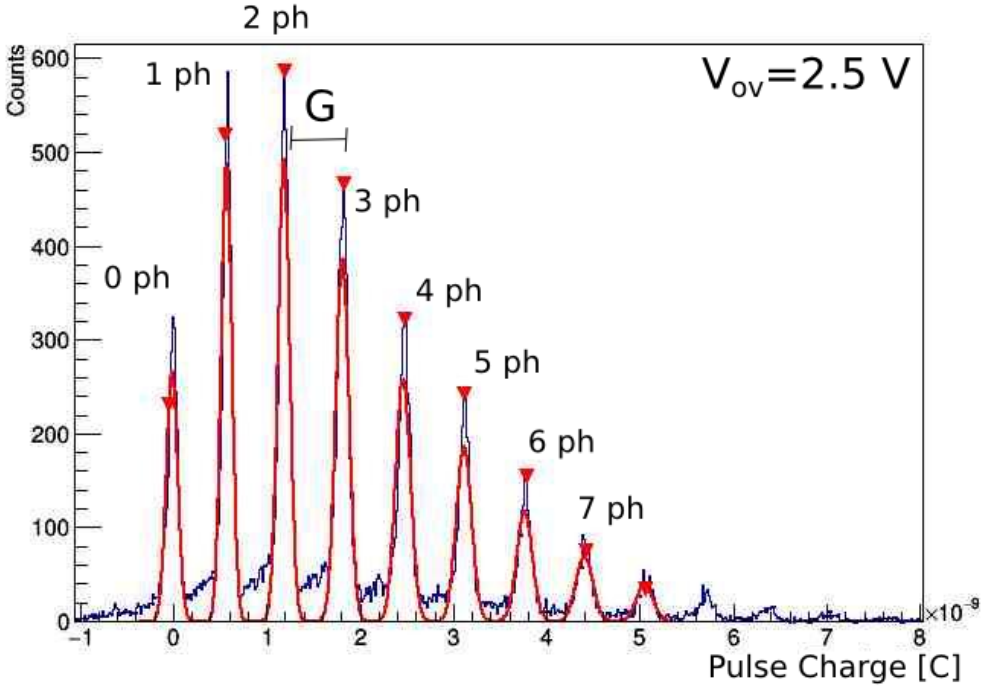

Figure 3.14: Charge spectrum obtained with the AdvanSiD ASD-NUV3S-P SiPM model of 3×3 mm^2 of active area, with about 10 thousand recorded waveform at $T = 300$ K.

of the multiplication avalanche in semiconductor-based photodetectors is produced by a different mechanism with respect to the PMTs one, as explained in the chapter 2, the SiPM gain value, at the same overvoltage, does not change with the temperature. This is clear observing the equation 2.20, where the temperature dependence is absent. Moreover, as explained in the previous paragraph, the breakdown voltage decreases at lower temperature so, to keep the same gain value expected at room temperature, the bias voltage will be lower. I verified the gain stability as a function of temperature for several SiPMs. For these measurements I used the Cold Head experimental apparatus described in the previous chapter. The SiPM under test was connected to the pre-amplifier, as explained in the paragraph 3.1.1, and recorded with an oscilloscope. I acquired thousands waveforms triggered with laser pulses at different overvoltages and for several temperature values. Data were then analyzed using the ROOT framework with a dedicated program. The light pulse intensity was setted to obtain few photons reaching the device under test. In this way, acquiring enough waveforms, it is possible to observe the typical SiPM spectrum where the photons peaks are well separated. As an example, figure 3.14 shows the spectrum obtained with the AdvanSiD ASD-NUV3S-P SiPM model of 3×3 mm^2 of active area, with about 10 thousand recorded waveform at $T = 300$ K. The spectrum shows the data entries as a function of the charge produced by the avalanche. The charge is obtained by integrating the voltage

pulse in the time interval of the entire pulse (as exposed by equation 2.20). This integration interval changes for different devices and with the temperature. In fact, as already explained, the temperature variations generate an increase of the quenching resistance and, as a consequence, the recovery time of the cell. Moreover, the longer is the signal, the harder is the correct evaluation of the charge. Electronic noise could also degraded the measurement. For this reason, a very clean signal is necessary. In our case, the electronic noise was around $V_{noise} = 1\ mV$ peak-to-peak at $T = 70\ K$. The spectra obtained shown a good separation between two consecutive peaks. Again, as shown in figure 3.14 it is possible to observe and study the photons interaction with the device. In particular, the first peak on the left represent the so-called *pedestal* (0ph in figure) and it is due to triggered waveforms which did not produced signals. The following peak (1ph) is generated by a single photon, the next one is generated by the interaction of two photons in different cells (2ph), the third one by three photons (3ph) and so on. The distance between two consecutive peaks is the charge produced by a single photon so, dividing it by the electron charge, the gain can be obtained. I would like to spend a couple of words about the structure of the peaks. The SiPM is a digital-like device i.e. the output is the multiple of the output of a single cell multiplied by the number of fired cells that produced a signal. This is, of course, the ideal situation; in the real case some factors produce gain variations:

- small mechanical and structural differences between the cells;
- electronic noise, uncorrelated dark counts, afterpulses and crosstalks;
- photons that interact in the deepest part of the multiplication region.

All these factors generate a Poisson distribution of each peak which can be approximated as a Gaussian shape centered at the photon charge. The width of the peak is due to the electronic noise of the device and of the experimental apparatus, which generate a constant contribution σ_{noise}, and the multiplication fluctuation of each cell which has a dependence of the square root of the number of photons:

$$\sigma_k^2 = k\sigma_1^2 \tag{3.1}$$

so,

$$\sigma_k = \sqrt{k}\sigma_1 \tag{3.2}$$

where σ_1 is the standard deviation of one peak and k is the k-th peak. The total variance is then:

$$\sigma_{tot}^2 = \sigma_{noise}^2 + k\sigma_1^2. \tag{3.3}$$

The shape of the spectrum can be represented as the convolution of the Poisson distributions of each peak and can be expressed as a function $f(x)$:

$$f(x) = A \cdot \sum_{k=0}^{\infty} \mathrm{P}(\mu, k) \frac{1}{\sqrt{2\pi}\sigma_{tot}(k)} e^{-\frac{[x-x(k)]^2}{2\sigma_{tot}^2(k)}} \tag{3.4}$$

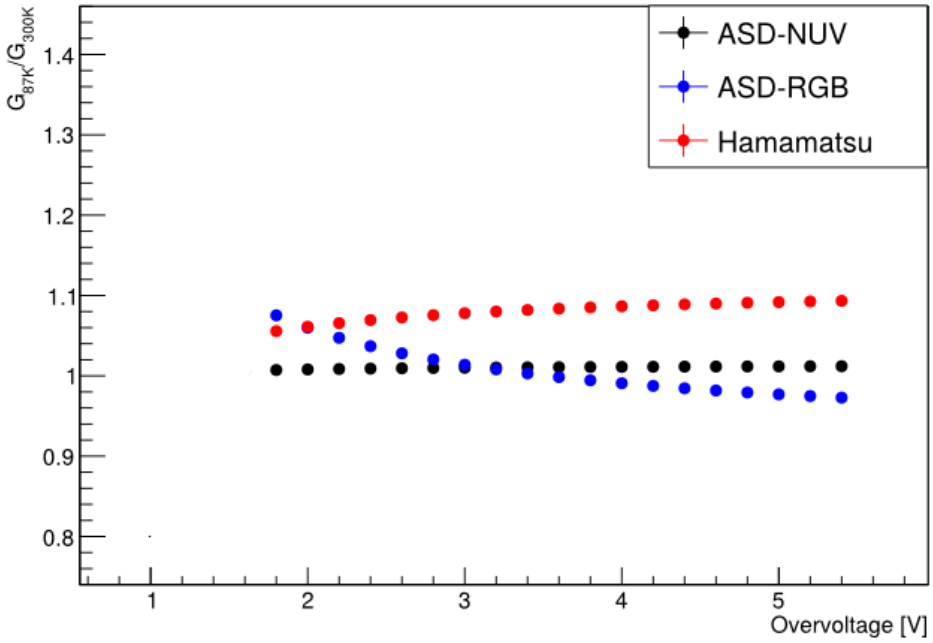

Figure 3.15: Gain ratios of different SiPM models as a function of overvoltage.

where A is a normalization constant equals to the total area of the curve, μ is the mean value of the Poisson distribution $\mathrm{P}(\mu, k)$, $x(k) = x_0 + k\delta$ is a step-function of the centroid coordinates of the k-th peak, in fact, x_0 is the centroid relative to the 0 photons peak (pedestal) and δ is the distance between the peaks. Furthermore, since the gain does not have any dependence on the temperature, it is constant at the different temperatures. In figure 3.15 the ratio between gain measured at 87 K and the gain measured at room temperature of different devices is shown. I want to underline that errors are smaller then the bullets. The small variation is due to uncertainties on the measure of breakdown voltage and temperature and also because of noise. It is important to underline that, especially in the AdvanSiD cases, since the increases of the quenching resistors generate an increases of the recovery time of the cell which require an integration time interval larger then the room temperature one. In particular, for the Hamamatsu device all the measurements are performed with an integration time lower than 100 ns. On the contrary, for the AdvanSiD ones the integration time interval changed from 100 ns at room temperature up to 300 ns or 400 ns at 87 K. In the last case, the electronic noise can generate a distortion of the measurement with a consequent distortion of the gain measurement. Anyway, all the measurements performed show a gain variation below of 10% for all the devices. Furthermore, gain measurements were performed for several devices at different temperatures from 300 K down to about 70 K and the results were compared. In figure 3.16 the gain vs overvoltage at 300 K for some SiPMs is shown. All the results are

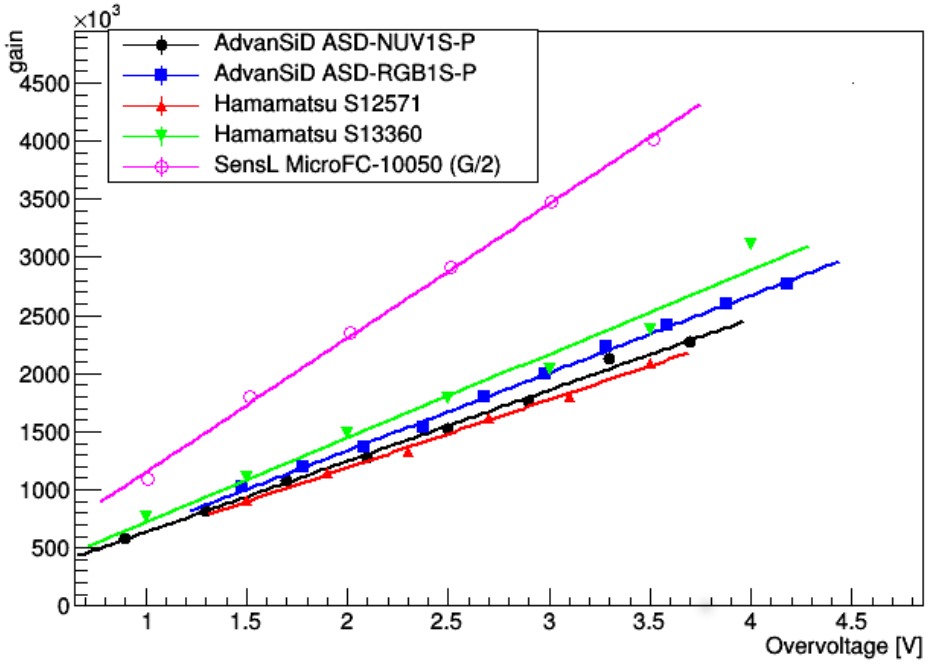

Figure 3.16: Gain measured for different SiPM models as a function of overvoltage. All these results are compatibles with the data sheets specifications.

compatible with the data-sheets values. Lines in figure are linear fits between the experimental data.

3.2.3 Noise

In this section I will expose in more detail the arguments presented previously in paragraph 2.2.5, especially from the experimental point of view. The evaluation and the measurement of spurious signals of the device is a fundamental aspect in experiments where the expected signal rate is low. As already mentioned, a SiPM presents two kind of noise signals: the correlated noise and the dark count rate (DCR). The DCR is generated by spurious signals produced by free carriers in the depleted region. Two main processes are responsible for dark counts, thermally generated e-h pairs and so-called field-assisted generation of free electrons which ca produce a DCR of few hundreds of kHz per mm^2 at $T = 300\ K$. Thermally generated free carriers can be reduced by cooling. There is a factor two reduction of the thermally generated dark counts every $8°C$ drop in temperature. Field-assisted generation without the help of a phonon (trap-assisted tunneling [66, 67]) has, compared to the thermal generation, a relatively small effect. It can only be reduced by operating the SiPM at a smaller electric field, thereby lowering the gain and reducing the PDE.

At first order, the thermal generation of carriers is proportional to the

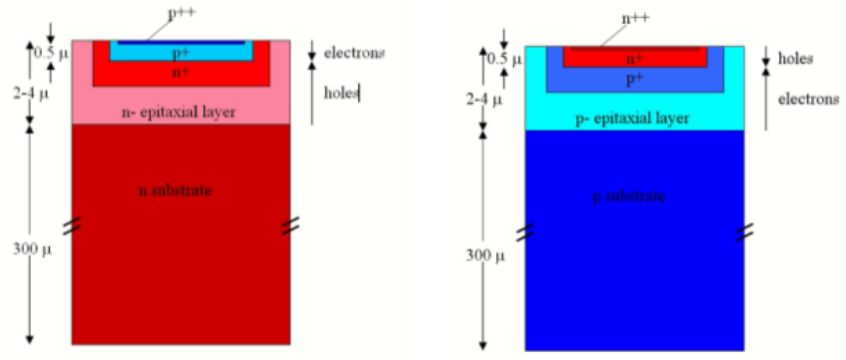

Figure 3.17: Scheme of p-on-n (left) and n-on-p (right) layers for a SiPM.

depleted volume, which, for every cell, is the area times the thickness of all the layers on top of the low-ohmic substrate. In the p-type layers, the electrons and, in the n-type layers, the holes drift towards the high field region of the junction. The electrons will trigger a breakdown with higher probability than the holes. In standard p-on-n type SiPMs, the thickness of the p-layer is normally much thinner than in the n-on-p SiPM (figure 3.17). Consequently, the lowest rate of dark counts can be expected for the p-on-n type SiPMs. Decreasing the temperature, these components drop drastically and, at the temperature of liquid argon (87 K), the rate is lower than 1 kHz. The correlated noise components, which are composed by after pulses and crosstalks, have a different behavior. At cryogenic temperatures, the rate of correlated noise is strongly dependent by the SiPM unction type. Because of the different kink of carriers which generate the avalanche, p-on-n SiPM and n-on-p SiPM have a different behavior, as described below. To measure the SiPM noise, I placed the SiPM under test into the cold head apparatus in dark conditions, i.e. without the laser pulses. Signals have been acquired with an oscilloscope and analyzed with a dedicated program to extract the different components. In this measurement I performed long-time recording, of the order of milliseconds triggering on the oscilloscope line, i.e. with no trigger. In this way I can well reconstruct the rates. Moreover I used an algorithm to analyze data described in [69]:

1. a delayed waveform (DLED) is calculated shifting the original waveform of few hundreds picoseconds (usually a bit less than the leading edge of the signal);

2. a difference between the two waveform is performed. This operation allows to delete the slow component of the signal and to highlight the fast peak;

3. the amplitude of each peak, measured from the starting point of the signal and the peak of amplitude is performed;

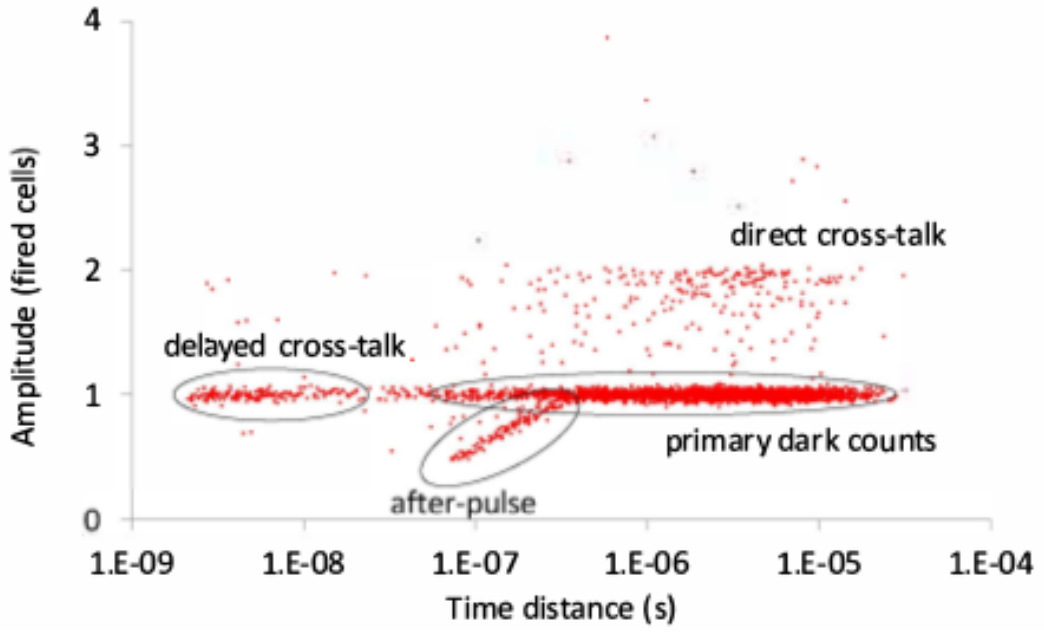

Figure 3.18: Scatter plot of the pulse amplitude as a function its distance from the preceding event at 7.2V over-voltage [69].

4. the temporal distance between each couple of consecutive peaks is measured;

5. plotting the peak amplitude vs the temporal distance a figure like 3.18 can be obtained.

The 3.18 is obtained by Fondazione Bruno Kesler (FBK) with a test SiPM with only few cells and it is useful to understand how recognize all the noise components. In the following some of the plots obtained analyzing data I acquired during my Ph.D. will be shown. Before that, I will focus the attention to the structure of the plot. A series of straight horizontal lines are visible and they are referred to the amplitude of the dark counts peaks. As expected, the density of points for signals produced by more then one-photon-like signals (n-ph) is lower and lower with respect to the one-photon-like signals (1-ph). In particular, the 1-ph points generate the so-called Dark Count Rate (DCR). The other lines from the 2-ph, are generated by synchronous signals produced by other cells with respect to the first one which produced the dark count. This is due, as explained before, by crosstalks effects. The last part to describe is the region close to the previous signal (with a temporal distance lower than about 30-40 ns and amplitude lower than 1-ph. This region is, of course, populated by afterpulses signals. Now I can expose the results obtained with the measurements using the cold head. I recorded waveforms with an oscilloscope 20 GSa/s sampling rate, 1 ms acquisition time. SiPM signals can be detected directly, without the amplification system, or with the usual pre-amplifier AdvanSiD ASD-EP-EB-N, at different temperatures from 300 K down to 70 K

Table 3.5: Typical dark count rate for different SiPM models at room temperature.

	Active area $[mm^2]$	Cell size $[\mu m]$	Cells number	DCR at 25°C kHz/mm^2
ASD-NUV1S-P	1×1	40	625	50 at $V_{ov} = 2\ V$
ASD-RGB1S-P	1×1	40	625	100 at $V_{ov} = 2\ V$
HPK s12571	1×1	50	400	100 at $V_{ov} = 3\ V$
HPK s13360	1.3×1.3	50	667	90 at $V_{ov} = 3\ V$

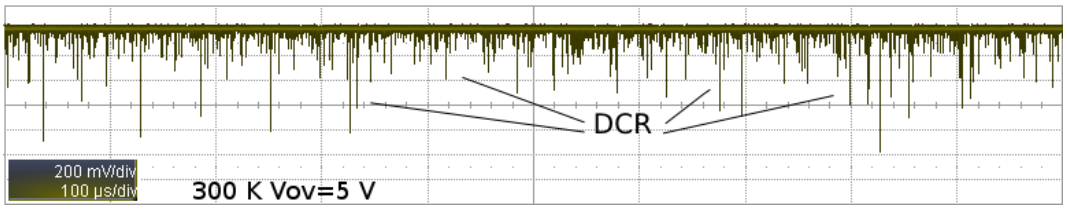

(a)

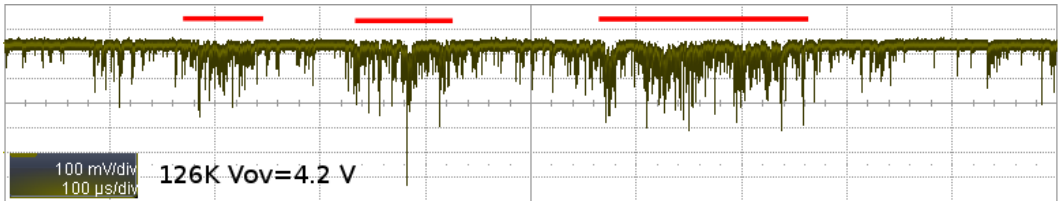

(b)

Figure 3.19: Waveforms of a SiPM model recorded at the same overvoltage ($V_{ov} = 5\ V$) at different temperatures: 300 K (a) and 120 K (b).

and at different overvoltages. Because of the rate of dark counts is proportional to the cells number, I used SiPMs with an active area of $1 \times 1\ mm^2$ ($1.3 \times 1.3\ mm^2$ for the Hamamastsu s13660), the smallest active area available for commercial devices. Furthermore, the cell size is 40-50 μm and, as consequence, the number of cells per device is around 400-600. Typical parameters of the tested devices are summarized in table 3.5. In figure 3.19, examples of recorded waveforms are shown. In particular, the waveform in figure 3.19a has been recorded at 300 K at $V_{ov} = 5\ V$, the figure 3.19b represents, on the contrary, the waveform of the same device at 120 K and at the same overvoltage. As clearly visible the two figures are completely different. The number of dark counts are dropped drastically at low temperature as expected. In figure 3.20, the comparison of DCR between some devices both at 300 K (figure 3.20a) and 87 K (figure 3.20b) is shown. The curves show that the noise signals increase as a function of overvoltage but at cryogenic temperature the values at low overvoltage are much smaller with respect the room temperature ones. It is important to underline that, at cryogenic temperatures, the correlated noise, at the same overvoltage, is higher then the value at room temperature. As a

consequence, at high overvoltage, the dark count rate at cryogenic temperature is higher than at room temperature. Furthermore, for the AdvanSiD RGB model, that is a n-on-p junction SiPM, the correlated noise does not increases as for the other devices and the noise is maintained low.

3.3 Other tests

Beside the characterization of SiPMs as a function of temperature performed with the cold head, during the three years of my Ph.D. some other tests have been made. In particular, the quantum efficiency evaluation in the VUV region and the radiation damages.

3.3.1 Quantum efficiency in VUV

The efficiency of SiPMs in the VUV region is an important parameter to know for application in liquid argon experiments. As mentioned in the first chapter of this thesis, liquid argon emits light in the near ultraviolet region, with an emission peak at $\lambda = 128\ nm$. Common devices are usually useless at this wavelength because of the window material. There are two main ways to adopt in this case:

1. using devices without window coverage;
2. covering the active surface with a *wavelength shifter*.

In the first case, some manufactures produce devices without the plastic window placed in front of the active area, keeping the photo-sensible region uncovered and free to detect photons directly. In this case VUV photons are not absorbed by the window so, they can interact in the multiplication region and produce signals. The second possibility is, probably, the most common choice, and it is the way I choose to follow for the pursuance of my Ph.D. project. This choice has been done also taking into consideration the previous experience acquired by the ICARUS group for the wavelength shifter deposit on PMTs surface.

Wavelength shifter deposit

Lets start describing the experimental apparatus used to deposit the wavelength shifter on the active surface of SiPMs. The technique is the same described in section 1.4.1, used for the ICARUS PMTs: the evaporation of TPB directly on devices active surface window. The experimental apparatus is composed by a vacuum chamber containing a Knudsen cell as shown in figure 3.21. An heater heat up the cell filled with about 1 g of TPB up to 210 $°C$ to evaporate the devices placed on the top of the chamber at 20 cm from the cell. In this way, I am able to deposit TPB on the surface of each array with

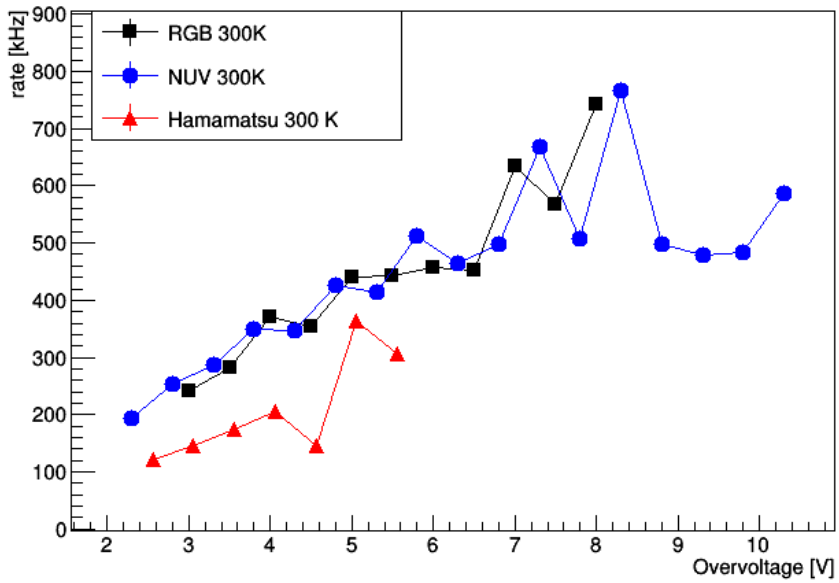

(a)

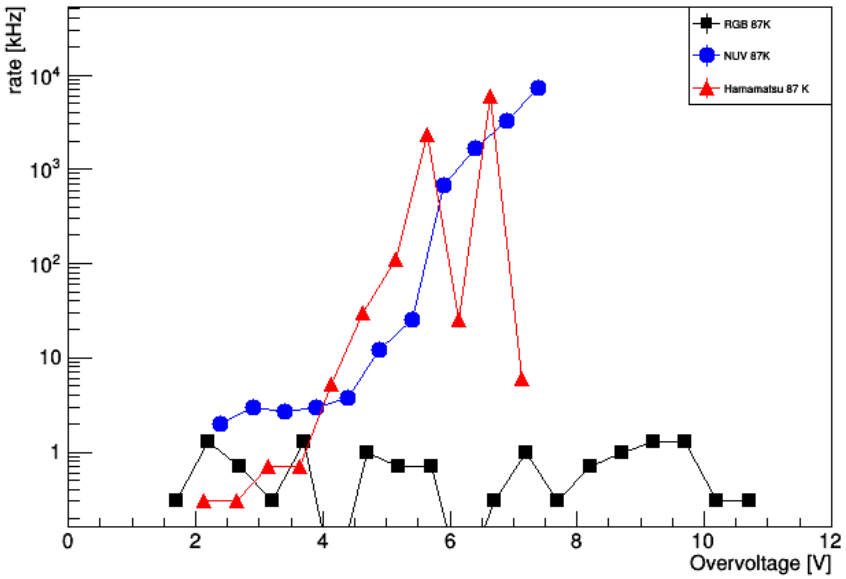

(b)

Figure 3.20: Dark count rates for different SiPM models as a function of overvoltage at 300 K (a) and at 87 K (b).

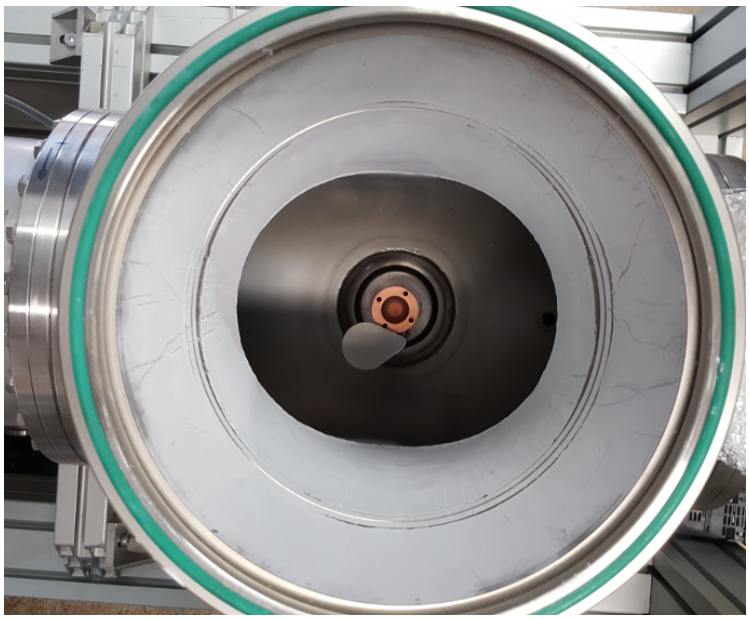

Figure 3.21: Photo of the knudsen cell of the evaporation system.

a density of $0.27 \pm 0.04\ mg/cm^2$, which is comparable with the value used for ICARUS PMTs.

Monochromator measurements

The monochromator system, described in the dedicated paragraph at the beginning of this chapter, allows to characterize different photodetectors. I used it to test single SiPM, SiPM arrays, photodiodes, PMTs and the custom SiPM arrays described in the following chapter. To perform the measurements I fixed the device under test on the dedicated support into the vacuum chamber, in front of the VUV beam light. The device in than biased with a picoammeter, the same used to bias the reference photodiode. A Labview program allowed to acquire both current and voltage informations coming from the device under test or from the reference photodiode. In the mean time the light wavelength can be changed automatically to scan the VUV light wavelength range between 120 nm and 220 nm. The current as a function of the wavelength for some devices under test and for the reference photodiode could be calculated using a Labview program. Thanks to the calibration curve (shown in the previous section) it is possible to calculate the quantum efficiency of each device under test.

3.3.2 Radiation hardness

Another test performed with SiPMs is a series of measurements devoted to evaluate their radiation endurance. In collaboration with the MEG II experiment [70–72] and thanks to the Chemistry department of Pavia University, I

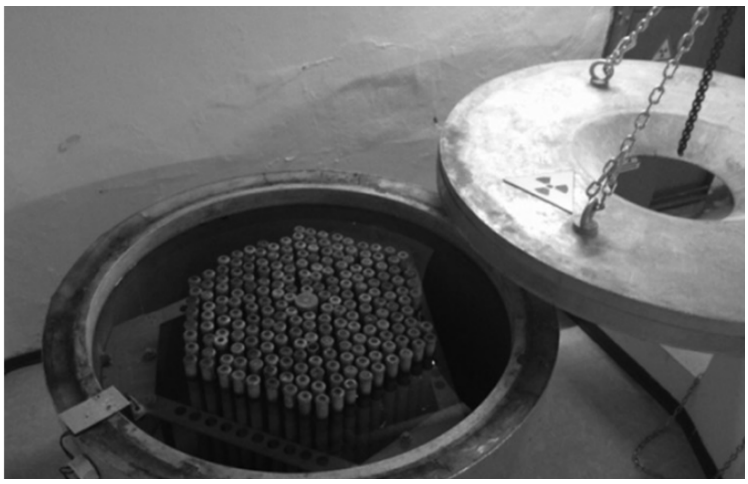

Figure 3.22: Photo of the SM1 facility.

could use the neutron flux generated by the thermal Sub-critical Multiplication complex (SM1) moderated with water [73]. The fuel is natural uranium in metallic form arranged in 206 Aluminum-clad fuel elements with an inner diameter of 2.8 cm and a length of 132 cm (figure 3.22). Fuel elements are assembled in a hexagonal prism geometrical configuration with a radial dimension of 114 cm and a height of 135 cm (figure 3.23). Located at the center of the SM1 core, a Pu-Be neutron source has an emission rate equal to $8.9 \times 10^6\ s^1$ over the full solid angle [74]. Even if two channels are readily available for irradiation, I always use Channel A (Ring 2). The neutron spectra expected from Monte Carlo simulations in different configurations, thermal and fast, at channel A are shown in figure 3.24 compared with the experimental data processed with the SAND II code [75]. The SAND II code is able to obtain neutron energy spectra by an analysis of experimental activation detector data.

The expected integrated neutron fluxes at position A in the thermal configuration, used in the irradiation, is $(5.9 \pm 0.2) \times 10^4\ n\ cm^2 s^1$ (including slow and fast neutrons). In order to support the devices under test a Cd box 0.55 mm thick. We evaluated that, at position A, the neutron flux inside the box is about $4 \times 10^4\ n\ cm^2 s^1$.

The irradiation consists in a controlled exposition to the neutron flux for several seconds/minutes at the SM1 facility. All measurements on SiPMs have been done at fixed temperature of $30°C$. Every 1000 s of irradiation (integrated dose of about $4 \times 10^7\ n\ cm^2$), each device has been characterized in term of I-V curve, breakdown voltage and noise. We have repeated this procedure several times up to a total exposition of $1 \times 10^4\ s$ (integrated dose of about $4 \times 10^8\ n\ cm^2$). I irradiated different SiPM models: the AdvanSiD ASD-NUV3S-P50 (used in MEG II experiment), the AdvanSiD ASD-NUV3S-P40 and ASD-RGB3S-P40, the Hamamatsu S12572-050P and the Excelitas C30742-33-050-X. The I-V curves have been measured using a picoammeter connected to a PC with an USB-GPIB converter and controlled with a Labview program.

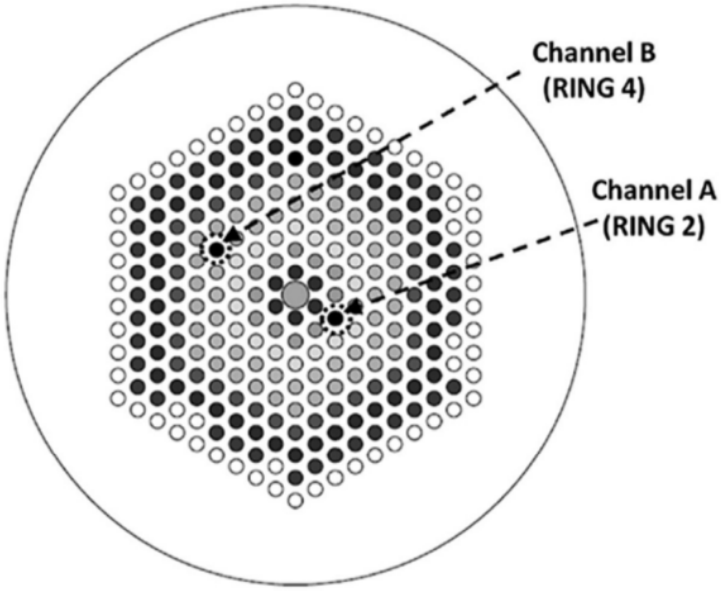

Figure 3.23: Scheme of the placement of each fuel element into the SM1 facility.

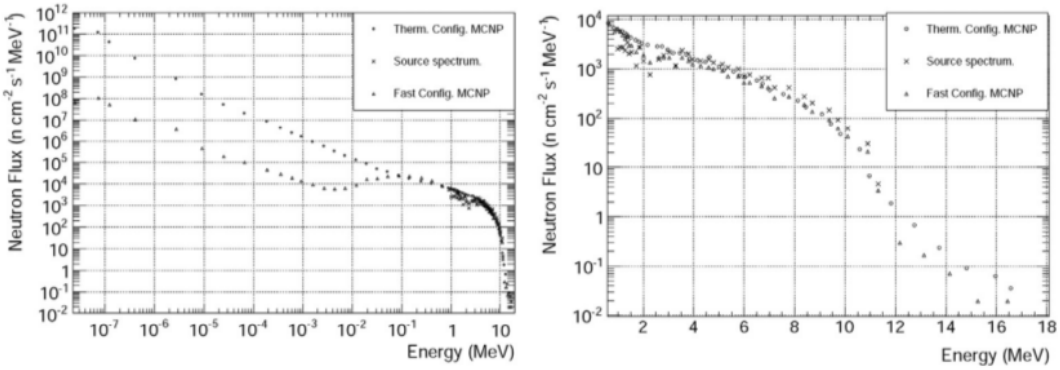

Figure 3.24: The neutron spectra expected from Monte Carlo simulations in different configurations, thermal and fast, at channel A into the SM1 facility.

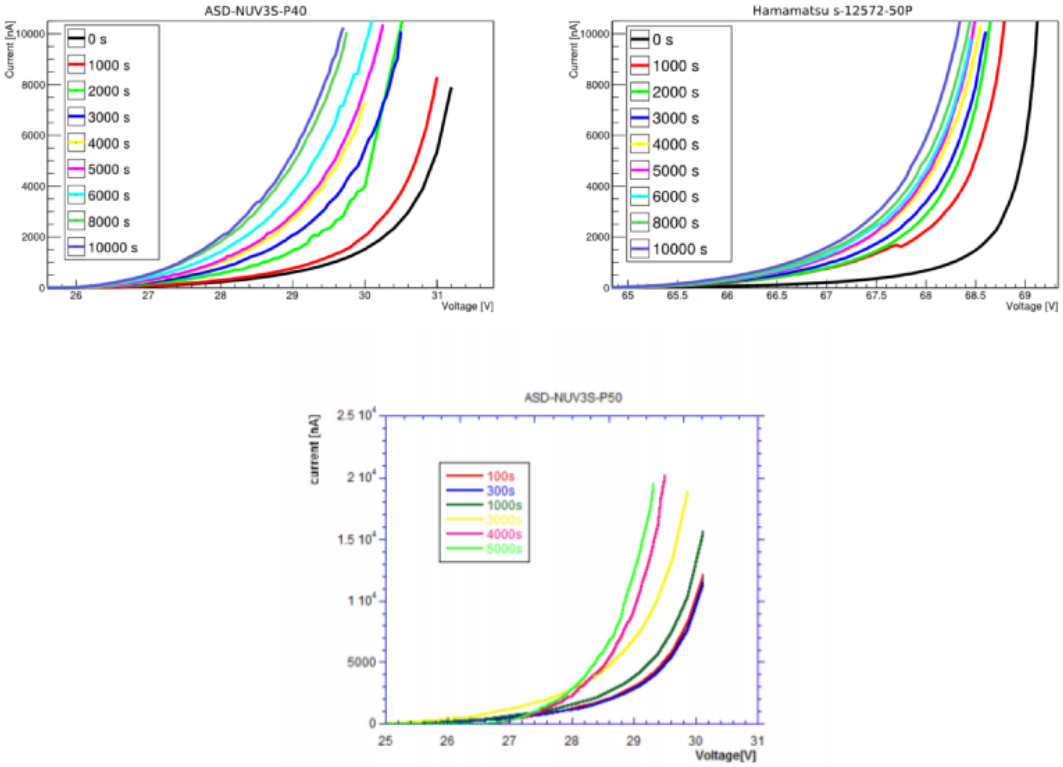

Figure 3.25: I-V curves for three different SiPM models at different radiation exposition time.

We recorded the I-V curves for all the devices before and shortly after each irradiation. Devices were irradiated once per day and measured two hours after the irradiation to allow for the decay of metastable nuclei. In a few cases measurements were performed from few minutes to several hours after the irradiation to evaluate the contribution from metastable nuclei but no effect was detected. For all devices the dark currents increase as the integrated doses increase. For example in figure 3.25, the I-V curves for various neutron doses for Hamamatsu and AdvanSiD ASD-NUV3S models are shown. For all the device under tests, the irradiation doses don't affect the breakdown voltages, as shown in figure 3.26 left. Also the quenching resistance of all devices is insensitive to the neutron dose (figure 3.26 right).

To evaluate the contribution of irradiation to the dark noise, I recorded at fixed overvoltage the current as a function of the different doses. In figure 3.27 the curves at $V_{ov} = 1\ V$, $V_{ov} = 2\ V$ and $V_{ov} = 3\ V$ for AdvanSiD ASD-NUV3S-P50, AdvanSiD ASD-NUV3S-P40, AdvanSiD ASD-RGB3S-P40 and Hamamatsu models are shown. For these devices the trend of the current is linear with respect the neutron dose for each value of over-voltage. There is no evidence of big differences between each SiPMs. Comparing the curves of AdvanSiD NUV devices, it is possible to observe that the current of the $50 \times 50\ \mu m^2$ cell size device (ASD-NUV3S-P50) is higher then the $40 \times 40\ \mu m^2$

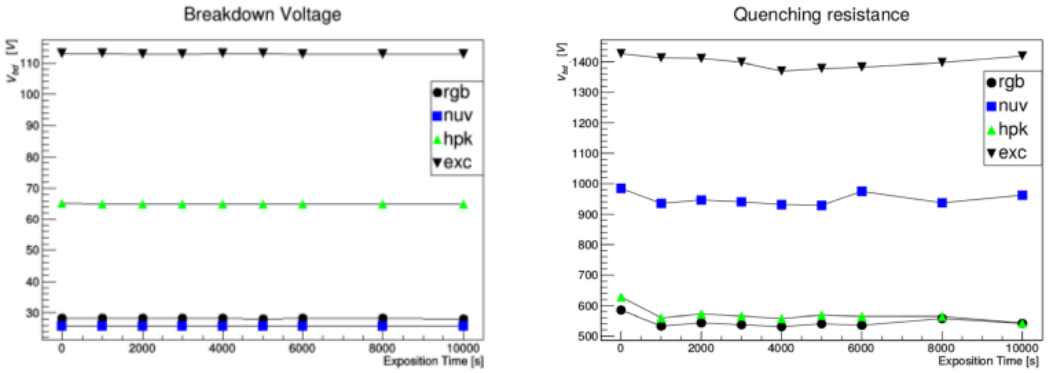

Figure 3.26: Breakdown voltage (left) and quenching resistance (right) as a function of exposition time for different SiPM models.

cell size device (ASD-NUV3S-P40). This is probably due to the correlated noise increases, in particular the after pulses.

3.4 Summary of the results

In this chapter all the measurements performed with single SiPMs have been presented. The goal of my Ph.D. research is to apply the SiPM technology into a LAr-TPC, in particular for neutrino search detectors. This kind of detector, as explained in the first chapter of this thesis, has usually huge active volumes and the idea to simply use single SiPMs in liquid argon can be hard to do. Using single SiPMs is, of course, possible but it requires a very large number of readout channels and a really complex analysis software. For this reason I developed multi-SiPMs test-arrays with common readout that will be described in detail in the next chapter. Thanks to the results presented in this chapter, I chose to continue my research focusing on three SiPM models:

- AdvanSiD ASD-NUV3S-P,
- AdvanSiD ASD-RGB3S-P,
- Hamamatsu s12572-050P,

because of these main features:

- the AdvanSiD models have a very low breakdown voltages which plays a crucial role in terms of power supplies requirements as shown in figure 3.11 of section 3.2.1;
- the Hamamatsu model has a very fast signal, faster than 70 ns which is perfect for triggering and timing applications [76–78];
- all the three models are cheaper with respect to the other tested models (around 2 euros per mm^2).

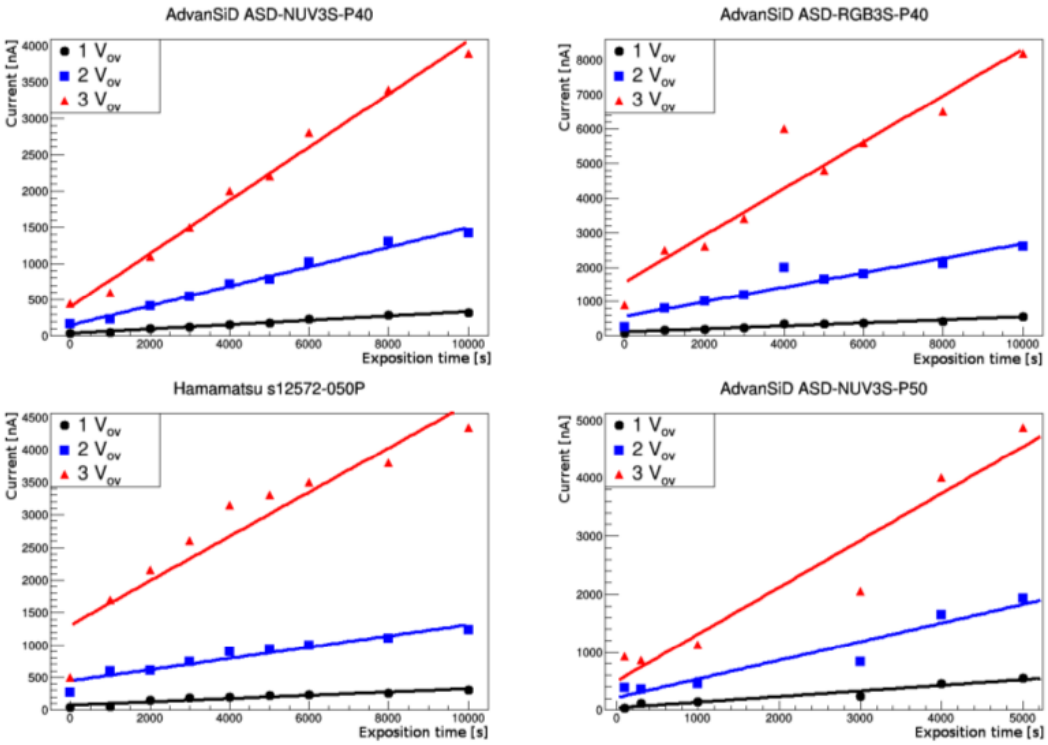

Figure 3.27: Dark count rates for different SiPM models as a function of exposition time at three different value of overvoltage.

In the following chapter I will describe the core of my research, the development of SiPM custom arrays able to work in liquid argon with performance comparable to the cryogenic PMTs.

Chapter 4

SiPM array with common bias and readout

In this chapter, the core of the research carried out during my three years of my Ph.D. is presented. The necessity to improve the performance and the detection sensitivity of LAr-TPCs is, nowadays, one of the main technological challenge in neutrino research. In particular, the possibility to apply a magnetic field into the active volume can allow recognizing the charge of the particle which produced the interaction. This permits to study neutrino and anti-neutrino interactions with high precision. As described in the first chapter of this thesis, the LAr-TPCs for neutrino experiments are usually composed of multi-wires planes and of photodetection system made by large area cryogenic PMTs. However, these devices become completely useless under the effect of a strong magnetic field. A possibility to replace the PMTs comes from the SiPMs technology. SiPMs are semiconductor-based photodetectors with high gain and fast signals as PMTs, but they are insensitive to magnetic fields. The main problem of SiPMs is the small active surface: commercial devices are usually smaller than $4 \times 4\ mm^2$. In this chapter I will discuss how it is possible to increase the active surface, keeping the typical performance of single SiPM, with a mixed parallel/series connections of several devices. Furthermore, I will present the results of tests performed both at room and cryogenic temperature and the last test with cosmic rays in LAr-TPC.

4.1 Realization of SiPM test-array

Increasing the active surface of a device is possible in different ways. I chose to build custom arrays of commercial SiPMs with common bias and common readout composed by 16 $3 \times 3\ mm^2$ devices each. This choice has been made taking into account the following reasons:

- the common bias and common readout is useful to keep as lower as possible the readout channels;

- commercial SiPMs has been selected from the measurements described in the previous chapter and taking into consideration the observations of paragraph 3.4;
- the number of SiPMs for each array has been fixed at 16 devices because it allows to study different electrical configurations with the same device (see paragraph 4.1.1).

We designed a custom double-face circuit in INFN and University of Pavia laboratories and, in collaboration with the Phoenix company, that realized the pcb support and Me-Vinco to weld the SiPMs on it, we built six arrays. The SiPM models I chose for this first series are: AdvanSiD ASD-NUV3S-P, AdvanSiD ASD-RGB3S-P and Hamamatsu s12572-050P. To select the best device, I measured the breakdown voltage, at fixed temperature, of about 200 SiPMs for each model, using a system allowing to measure 32 SiPMs simultaneously. After this test I chose 16 SiPMs with the same breakdown voltage to be mounted on one array.

4.1.1 Electrical configurations

As mentioned before, the double-face electrical circuit used to connect 16 SiPM together, allows to study different electrical connections. This is one of the main topics I studied, because connecting SiPMs in different series/parallel configurations change drastically the array performance. I first introduce a nomenclature to help the identification of the configuration. From now the structure:

$$N_1 s N_2 p \tag{4.1}$$

means that there are N_1 SiPMs connected in series (s) and N_2 SiPMs connected in parallel (p). For example, "2s8p" means that the array is configured with two SiPMs connected in series and each couple is connected in parallel with the others. To understand the differences between each configurations it is useful to refer the discussion to what has been said in paragraph 2.2.2. In particular to the to figures 2.11 and 2.12 and to the equations 2.11 and 4.3 that I rewrite for a better understanding:

$$\tau_d^{rise} \sim R_S(C_D + C_Q) \tag{4.2}$$

$$\tau_{slow}^{fall} = R_Q(C_D + C_Q). \tag{4.3}$$

From that figures it is clear what happens connecting some SiPM together. The capacitance of the system increases connecting in parallel some device, and so does the quenching resistance R_Q. As a consequence, both the leading edge and the trailing edge get worse; furthermore, the bias supply does not change. Vice-versa, the time features of the signal improve connecting some devices in series, but the bias increases proportionally to the number of devices in series. In table 4.5 the main differences between series and parallel connections are

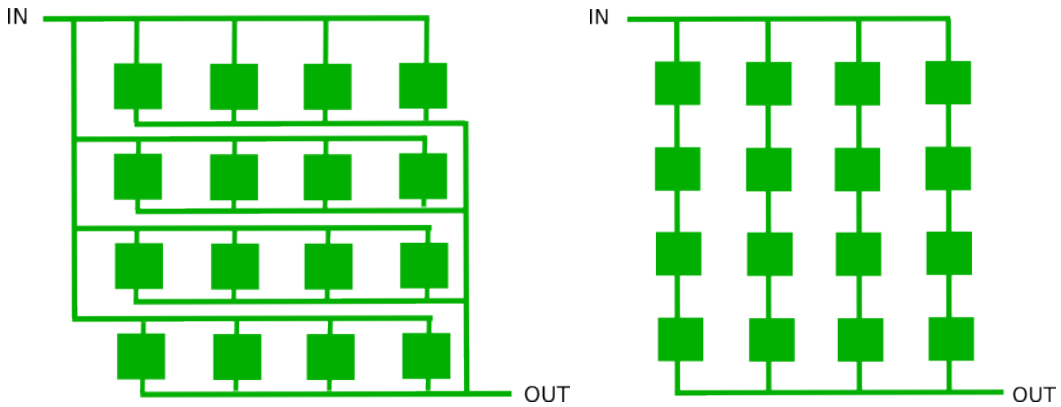

(a) (b)

Figure 4.1: Scheme of two possible electrical configurations of the SiPMs array: the 1s16p (a) and 4s4p (b).

shown. With simple modifications, the circuit we built allows to study different configurations:

- 1s16p (figure 4.1a),
- 2s8p,
- 4s4p (figure 4.1b),
- 8s2p,
- 16s1p.

The last configuration 16s1p has been soon discarded due to the too high bias voltage. For example, in the case of Hamamatsu device at room temperature the bias voltage should be around $V_{bias} = 1050\ V$. In this case the advantage of SiPMs to have lower bias voltage with respect to the PMTs is completely lost.

4.2 Tests on performance

In this section the tests performed with the SiPMs array will be presented. In particular, in the first test a comparison between the different models in terms of breakdown voltage, gain and time features was carried out, also for a lower number of SiPMs. Once the performance of series and parallel connections were well understood, I focused the tests on the entire array in different configurations. At the end, the best configuration has been chosen to connect some arrays together.

Table 4.1: Some characteristics of the AdvanSiD NUV model SiPMs array.

ASD-NUV	V_{bd} $[V]$	LE $[ns]$	TrE $[ns]$	Q [pQ]
1s4p	25.9	5.6 ± 0.2	280 ± 21	15.4 ± 2.6
4s1p	103.7	1.7 ± 0.1	59 ± 14	3.9 ± 0.6

Table 4.2: Some characteristics of the AdvanSiD RGB model SiPMs array.

ASD-RGB	V_{bd} $[V]$	LE $[ns]$	TrE $[ns]$	Q [pQ]
1s4p	28.4	16.7 ± 0.3	207 ± 9	42.3 ± 5.1
4s1p	113.7	1.8 ± 0.2	93 ± 5	12.9 ± 1.3

4.2.1 Preliminary test

To check the correct operation of each array, several test were performed immediately after their realization. I first verified the theoretical features I expected from parallel and series connections. To do this, simply inhibiting some electrical contacts, it is possible to obtain different configurations such as the circuits shown in figures 4.1. Keeping the same nomenclature introduced before, the 4s1p and 1s4p configurations were studied in terms of breakdown voltage, time features, amplitude and charge. The results are shown in tables 4.1, 4.2 and 4.3 for ASD-NUV3S-P, ASD-RGB3S-P and Hamamatsu s12572-050P arrays respectively. All these features show the expected behavior:

- concerning the breakdown voltage it is easy to understand that for parallel configuration the bias does not change but, for the series configuration increases proportionally to the number of devices connected, in this case 4. So, the breakdown is four times higher than both the single SiPM and the 1s4p configuration.

- This is true also for the charge, but in reverse way. So, the series configuration has a charge (i.e. a gain) four times lower then the parallel configuration and single SiPM.

- The time features, as described in the previous paragraph, change because of the capacitance and resistance modifications. In this case it is more difficult to know exactly the modification-factor because the equations 2.11 and 4.3 are referred to an equivalent-circuit-model which is an approximation of the real case.

This test were performed using different groups of four SiPMs and different light conditions. Also, the temperature was not monitored and some fluctuations of the values are expected due to this. However, the goal of this first test was to check mainly the mechanical structure, resistance and "changeability" of the circuit.

Table 4.3: Some characteristics of the Hamamatsu model SiPMs array.

HPK s12572	V_{bd} $[V]$	LE $[ns]$	TrE $[ns]$	Q [pQ]
1s4p	64.1	3.2 ± 0.5	162 ± 4	7.4 ± 0.5
4s1p	256.3	1.1 ± 0.4	43 ± 1	1.8 ± 0.1

4.3 First test in LAr-TPC

The tests described in the previous paragraph were made at room temperature to verify the mechanical and electrical features of each array. The following step was to verify if they can support the thermal stress due to the high variation of temperature when immersed in liquid argon. To check this fundamental point I used a small LAr-TPC at CERN and described in detail in the following paragraph, recording cosmic rays signals. Before doing that, I prepared the arrays to operate in liquid argon, thus covering the active surface with TPB with the same technique described in the previous chapters. In this case the evaporation system allowed to cover up to six arrays together (figure 4.2) with a TPB density of 0.271 ± 0.042 mg/cm^2.

4.3.1 Experimental apparatus

Tests have been carried out by collecting data with cosmic rays with a 50 liters liquid argon time projection chamber located into the building 182 at CERN. The chamber has an active volume of $(33 \times 33 \times 47)$ cm^3, it is placed inside a stainless steel cylindrical vessel 100 cm high, with a radius of 30 cm and 3 mm wall thickness (figure 4.3). The active volume corresponds to 71 kg of liquid argon. Charged particles passing through the detector active volume produce ionization electrons in the liquid which drift vertically towards the anode by means of a constant electric field $E = 500$ V/cm. The anode consists of two orthogonal wire planes mounted at a distance of 4 mm. Each stainless steel wire has a diameter of 100 μm, the distance between the wires is 2.54 mm and each plane is made up of 128 wires. The cathode and the additional field-shaping electrodes are copper strips with 5 mm thickness positioned on a vetronite support applying printed board techniques. The distance between two adjacent strips is 10 mm. The ionization electrons drift through the first wire plane which is an induction plane, whilst are stopped by the second wire plane, so called collection plane, which acts like a charge collector (figure 4.4).

Behind the wires planes, as shown in figure 4.4, the photodetection system is placed. It is composed by a cryogenic 8 inches windows diameter PMT Hamamatsu R5912-mod positioned at the center and fixed to two vetronite planes to keep it in the correct position. The bottom one has a central hole of 12 cm diameter and it is surrounded by the six SiPM arrays (figure 4.5). The arrays are fixed to a support, screwed to the vetronite plane, which contain the electrical circuit and the connectors for the anode and cathode. Bias and signal

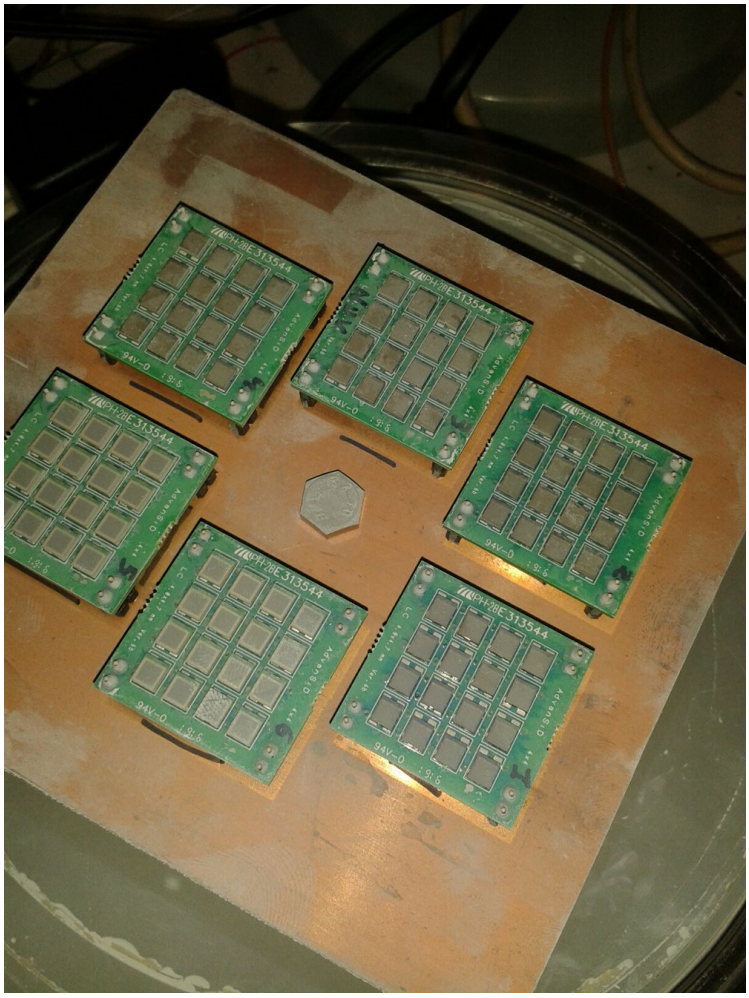

Figure 4.2: Photo of the SiPMs array after the TPB evaporation session on the active surfaces.

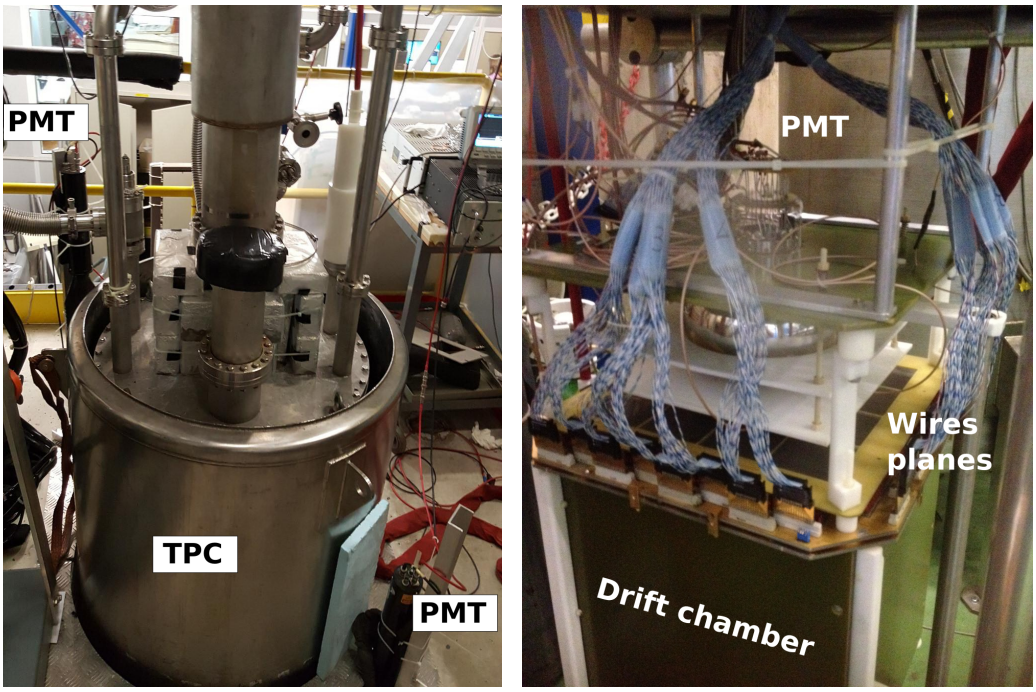

(a) (b)

Figure 4.3: Photos of the experimental apparatus at CERN (a) and the detailed view of the 50 liters LAr-TPC (b).

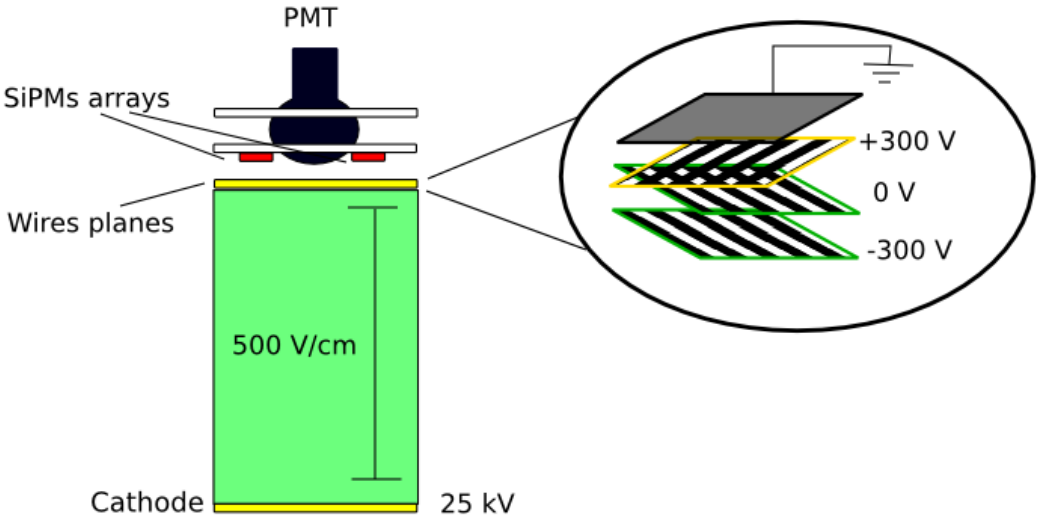

Figure 4.4: Scheme of the LAr-TPC with a detailed view of the wires planes and the photodetectors.

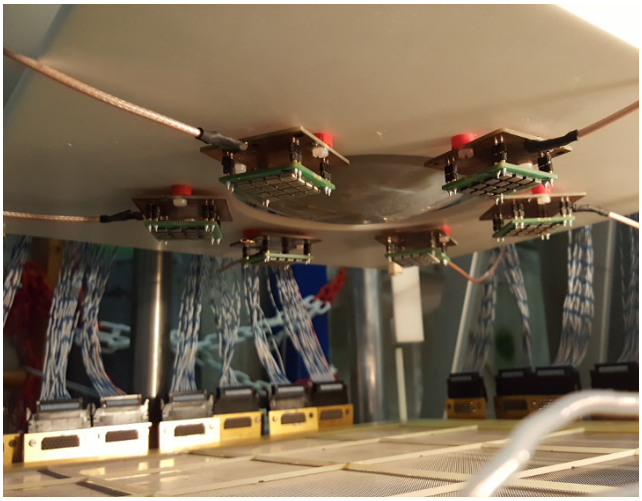

Figure 4.5: Photo of the photodetectors into the LAr-TPC at CERN. the six SiPMs arrays and the PMT are in the final position.

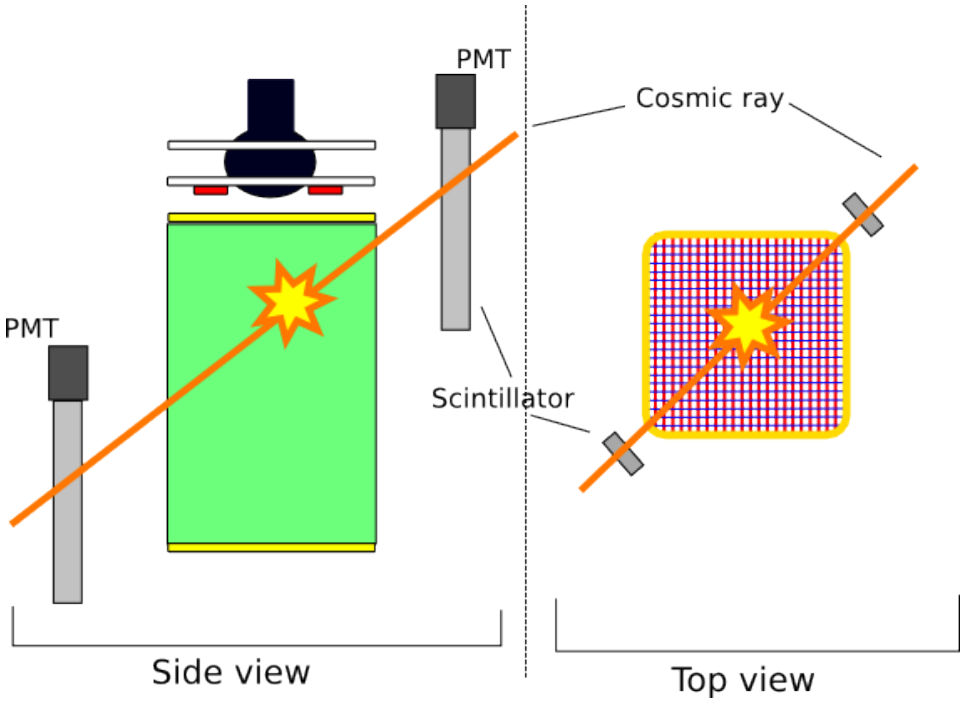

Figure 4.6: Scheme of the trigger system used for the tests with the 50 liters LAr-TPC at CERN.

pass through an RG316 coaxial wire up to a decoupling circuit placed outside the cold system. Furthermore, two external plastic scintillators read by PMTs allows to build a trigger system (figure 4.6). As described above, the active volume of the chamber is located inside the stainless steel cylinder. The upper face of this structure is an UHV flange housing the vacuum and the high voltage feeds-through, the liquid argon filling structure and the readout electronics. The cylinder is enclosed in a dewar 120 cm high and with 70 cm inner diameter for thermal insulation. This structure is filled with ultra-pure liquid argon up to a level not exceeding 60 cm of height, corresponding to about 160 liters. The purification circuit collects the argon gas evaporating from the liquid, passes it through an Oxysorb filter and a condenser and finally reintroduces it as a liquid at the bottom of the inner vessel. The apparatus for condensing vapor is built of a 18 m long serpentine tube housed in a 80 liters liquid argon bath in order to cool and re-liquefy the ultra-pure argon gas. This bath is placed 2 m above the detector vessel in its own cryogenic dewar and it is also used as a cooling fluid for the entire detector system. The total liquid argon usage of the system is 3.5 liters per hour and is fully balanced by the recirculation system. A cylindrical tank (30 cm in diameter, 50 cm high) is added in parallel to the gas argon circuit in order to remove from the system the contaminated argon gas generated by the evaporation on the warm inner surfaces during the first phase of the vessel filling. The filling procedure starts with obtaining a vacuum level of around 10^{-5} *mbar* inside the detector vessel by means of a turbo-molecular pumping system. The procedure continues with the start of the cooling of the detector and recirculation vessels and of the additional tank, by filling partially the corresponding dewars with commercial liquid argon taken from a storage container. From the same storage container the liquid argon is used to fill the inner detector passing through the recirculation/purification system. An argon gas phase is produced through evaporation of the liquid by contact with the warmer walls of the detector vessel. This gas is sucked and re-condensed into the additional tank, contributing to keep the filling pressure relatively low. The duration of the filling procedure takes about 2 hours at pressure not larger than 0.5 Bar. When the detector volume is filled, the additional tank is excluded from the circuit and the thermodynamic recirculation process is allowed to begin. The residual liquid argon, contained in the detector dewars, is allowed to evaporate. The only dewar which is then continually refilled is the recirculation system one. All operations like opening and closing of valves and pressures or levels flows controls, are carried out manually during the filling process. After the completion of the filling procedure, a steady state phase with data taking can start.

4.3.2 Data taking and results

The data acquisition system is composed by two separated systems for PMT and SiPMs respectively. The PMT electronics set-up is composed by a CANBERRA 2005 charge preamplifier and an ORTEC 570 amplifier. Signals pass

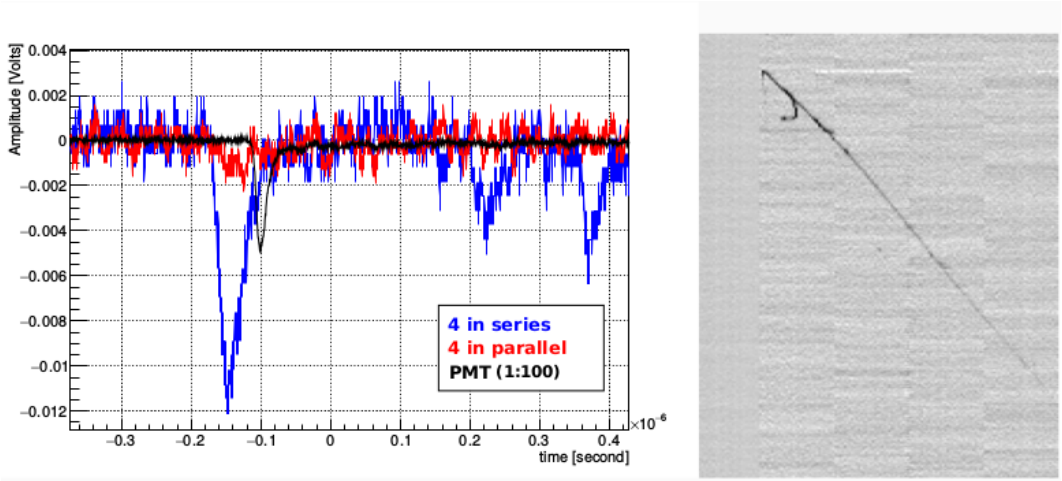

Figure 4.7: Recorded waveforms for the Hamamatsu SiPMs arrays in series and in parallel, the PMT signal and the relative muon track recorded by the wires system.

through an pulse shaper and splitted. One signal is read by an oscilloscope, the other is used by the multiwires readout system. Each couple of the three different SiPMs arrays models are configured with two different electrical connections. To test the performance of each connection I choose to use the 1s4p and the 4s1p connections. Furthermore, the bias voltage was guaranteed by picoammeters and a decoupling circuit allows to separate the bias from the signal. Waveforms were recorded with the same oscilloscope used for the PMT. As first, the two external scintillators are used to build up a cosmic rays trigger. Cosmic rays pass through the LAr-TPC and generate a scintillation light recorded from the SiPMs arrays and the reference PMT. The external scintillators are placed to select cosmic rays almost parallel to the floor, more precisely, with an angle of about 20°. In this way it is possible to reduce the showers contribution to the recorded signals and to select only the cosmic rays, mainly muons, produced inside the LAr-TPC. I recorded 70 cosmic rays events in which the SiPMs signals are in coincidence with the PMT ones and the wires. In figures 4.7, 4.8 and 4.9 some examples of waveforms are shown. In particular, in figure 4.7 a cosmic muon track recorded with the coincidence with the Hamamatsu 1s4p and 4s1p connections is shown. It is important to note that the difference between the PMT and SiPMs arrays signals is due to the big difference between the total active area, about 300 times bigger for the PMT. In figure 4.8 an example of a shower recorded with the Hamamatsu arrays is shown. In figure 4.9 the comparison between the different models all in 1s4p configuration is shown. Unfortunately, because of the small active area and the distance between each array, it is not easy to compare each event. However, even if the data collection it is not so big, it is possible to summaries the results of each device as follow:

- the AdvanSiD NUV arrays present good photon detection efficiency (eval-

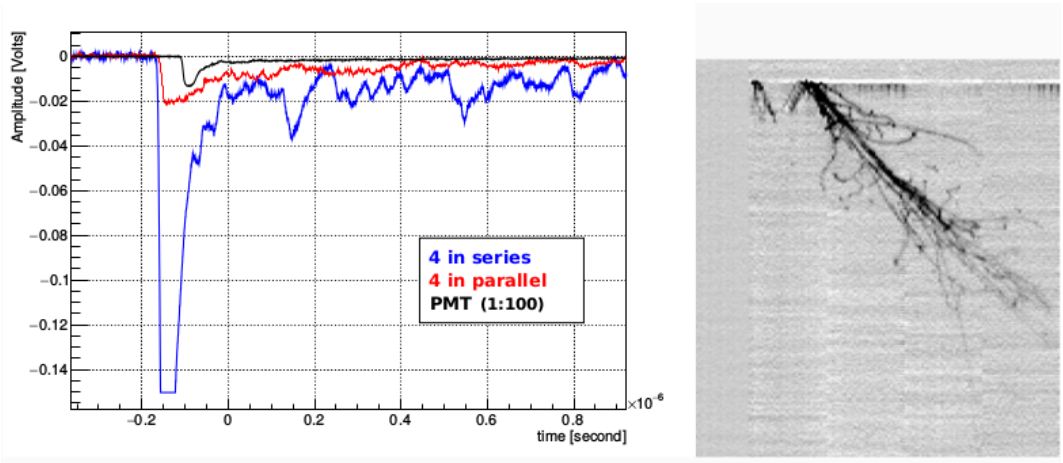

Figure 4.8: Recorded waveforms for the Hamamatsu SiPMs arrays in series and in parallel, the PMT signal and the relative muon track recorded by the wires system in case of very high signals due to a triggered shower.

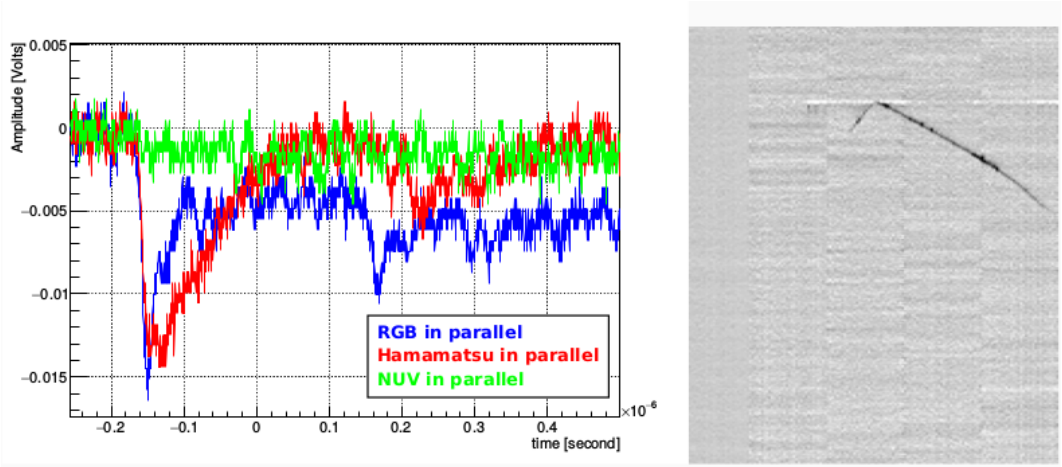

Figure 4.9: Recorded waveforms for the different SiPMs arrays in parallel configuration and the relative muon track recorded by the wires system.

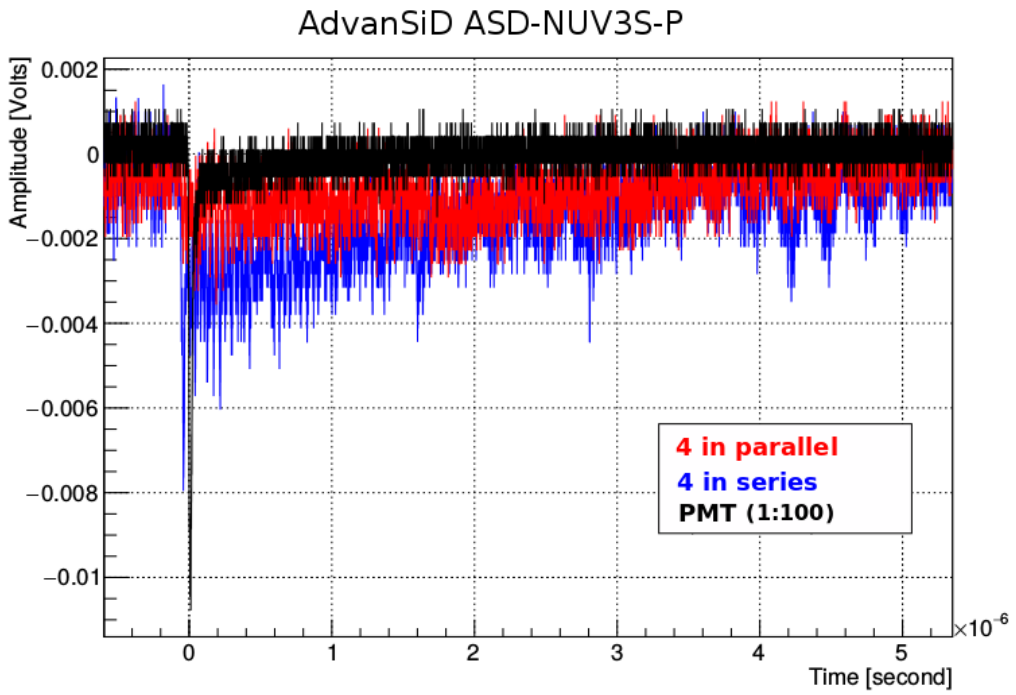

Figure 4.10: Detailed view of the waveforms for the AdvanSiD NUV SiPMs arrays in different configurations and the reference PMT.

uated comparing the amount of recorded signal with respect to the other SiPM models) and excellent working voltage, below 25 volts for the 1s4p configuration and around 95 volts for the 4s1p one. However they have high noise and very slow signals, with a recovery time of about 5 μs (figure 4.10).

- the AdvanSiD RGB arrays have good working voltage, around 28 volts and 110 volts for the 1s4p and 4s1p configurations respectively but the quantum efficiency is extremely low, because the peak of efficiency of these device is at $\lambda = 550\ nm$, far from the emission peak of TPB ($\lambda = 420\ nm$). Furthermore, also these devices have a long recovery time around 4 μs (figure 4.11).

- the Hamamatsu arrays have higher working voltage with respect to the AdvanSiD models (about 46 volts and 195 volts for 1s4p and 4s1p configurations repectively), however the recovery time is below 200 ns (figure 4.12).

Thanks to this test it is possible to conclude that, considering the three SiPM models arrays, the Hamamatsu has the best performance to work in liquid argon because of its fast recovery time and low noise rate. Furthermore, as shown in table 4.4, the SiPMs arrays leading edge is of the order of the PMT one, in particular for the series configurations.

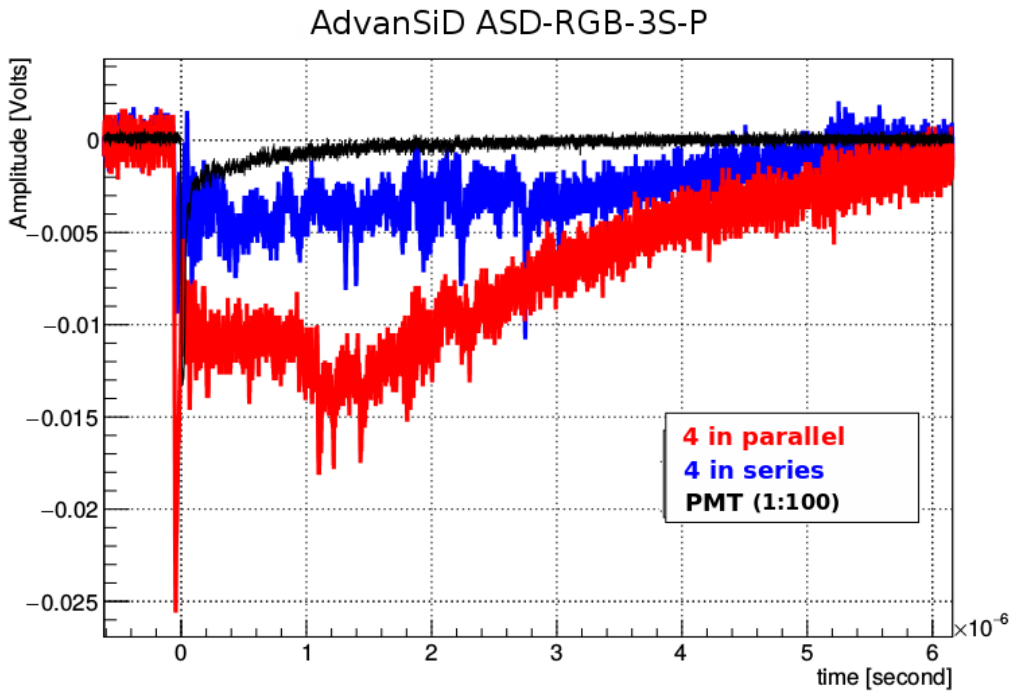

Figure 4.11: Detailed view of the waveforms for the AdvanSiD RGB SiPMs arrays in different configurations and the reference PMT.

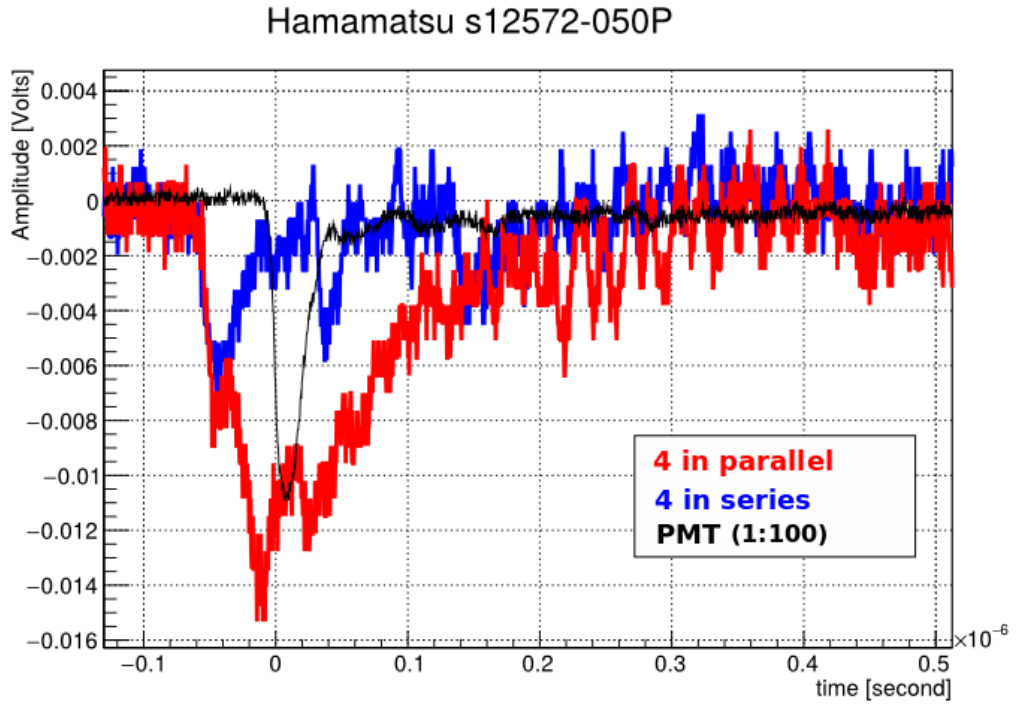

Figure 4.12: Detailed view of the waveforms for the Hamamatsu SiPMs arrays in different configurations and the reference PMT.

Table 4.4: Leading edges for the SiPMs arrays in different configurations.

	Parallel	Series
ASD-NUV	16 ns	13 ns
ASD-RGB	18 ns	13 ns
Hamamatsu	19 ns	12 ns
PMT	5-6 ns	

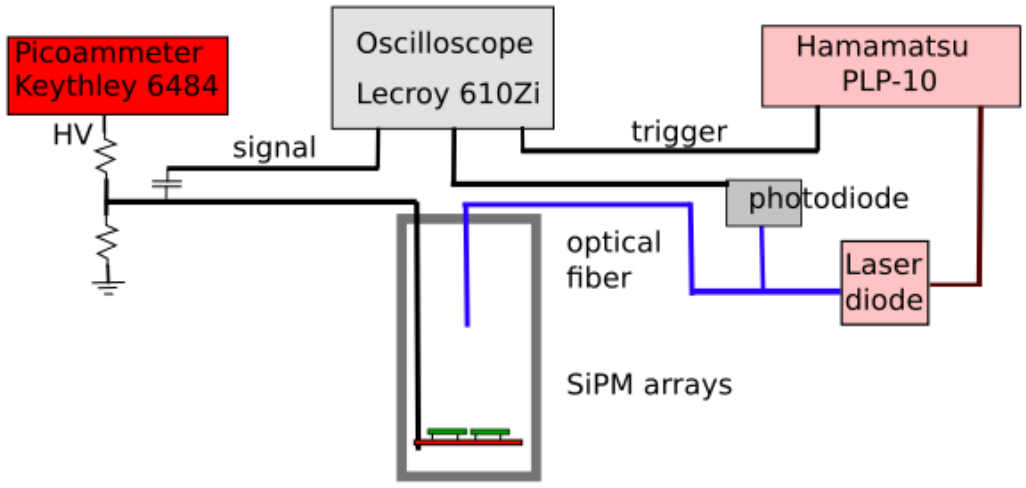

Figure 4.13: Experimental apparatus for the measurement of the time features of SiPMs arrays.

4.4 Increases of active surface and time features

The test performed at CERN allowed to establish the best SiPM model to use for our purposes. At this point I focus the tests especially for the Hamamatsu model. The next step is, of course, to increase the active area of the SiPMs array and to choose the best configuration. As described before, the configurations of each SiPMs array is completely customizable, but only few of them were studied. In particular, from the previous tests it is clear that SiPMs in series allow to improve the time features of signals but the working voltage increases and the signal amplitude decreases. For this reason the best solution is to keep the SiPMs arrays in 4s4p configuration. However, it is useful to compare different configurations to understand the performance modifications due to the different electrical connection. In particular, at this point, one of the most important feature to know is the time characteristic of the array. For this reason I built an experimental setup dedicated to study this feature. The system, shown in figure 4.13, is composed by a small dewar containing the SiPMs array placed at the center of a support fixed to a polystyrene cap. The cap allows to reduce as much as possible the ambient light and to keep all the system in the correct position. Furthermore, an optical fiber, fixed

into a small tube positioned at the center of the cap, is used to illuminate the device under test. This optical fiber is connected to a fast laser diode (Hamamatsu PLP-10: $\sim 60\ ps$ FWHM, 10^7 photons per pulse). A fast photodiode (Thorlabs High-speed photodetector model SV2) allowed to monitor the light intensity. Signals were recorded with a Lecroy WaveRunner 610Zi, 20 GSa/s oscilloscope and the bias of the device under test is guaranteed by a picoammeter. Data were acquired with the device enlightened by the same number of photons in order to evaluate the different behavior of each model when illuminated in the same conditions. For this test the three SiPMs models in 4s4p and 1s16p configurations were studied. Few thousands of waveforms were acquired at different overvoltages in both the configurations and for each model. A program allowed to measure the leading and trailing edges (LeE and TrE respectively), the peak amplitude (V_{max}), the mean charge ($\bar{Q}$) of signals and the time resolution ($\sigma\Delta t$). This last parameter has been defined as the standard deviation of the temporal distance between the array signals and the photodiode ones. In figures 4.14 and 4.15 the leading edge and the amplitude as a function of overvoltage are shown. Results (for instance, table 4.5 shows at fixed overvoltage the recorded data) show for each array, as deeply discussed in the previous sections, the expected modifications due to the different configurations. It is important to compare these results between the different models. In particular, even if the leading edge of the Hamamatsu array is quite worse with respect to the AdvanSiD arrays, the trailing edge is much better for the former than the latter at least of a factor two. For what concern the time resolutions, all the devices have a $\sigma\Delta t$ much lower with respect to the time features of the signal.

4.4.1 The hybrid circuit

All the tests shown so far illustrated the differences between each SiPM model. In particular, for the application I am interested in, the Hamamatsu model has the best compromise between bias voltage and time features, performance stability and costs. Furthermore, because of the good performance obtained with the our array PCB circuit, I chose to increase the total active area of the device connecting some arrays together. This is the best solution to evaluate the capability to record signals with an active area as larger as possible without building a dedicated array. Then, in this way, there is not the necessity to use other SiPMs, reducing the costs. Of course, the question on "how some SiPMs arrays can be connected together" is again the main topic. Also in this case I keep the same nomenclature introduced at the beginning of the chapter but, to well recognize if the configuration is referred to a single array or to a multi-array, I chose to use lowercase letters for a SiPMs connections into a single array and uppercase letters for arrays connections in a multi-array device. So, connecting for arrays together, there are three possibilities:

- 1S4P (which is equivalent to a single "big" array in 4s16p configuration);

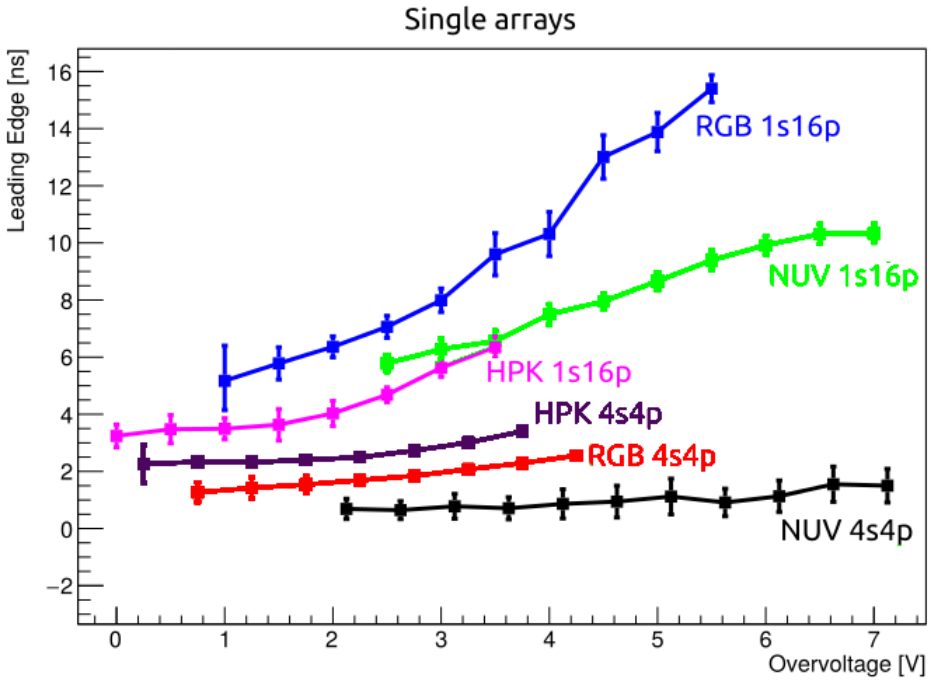

Figure 4.14: Leading edge of different arrays in different configurations as a function of overvoltage.

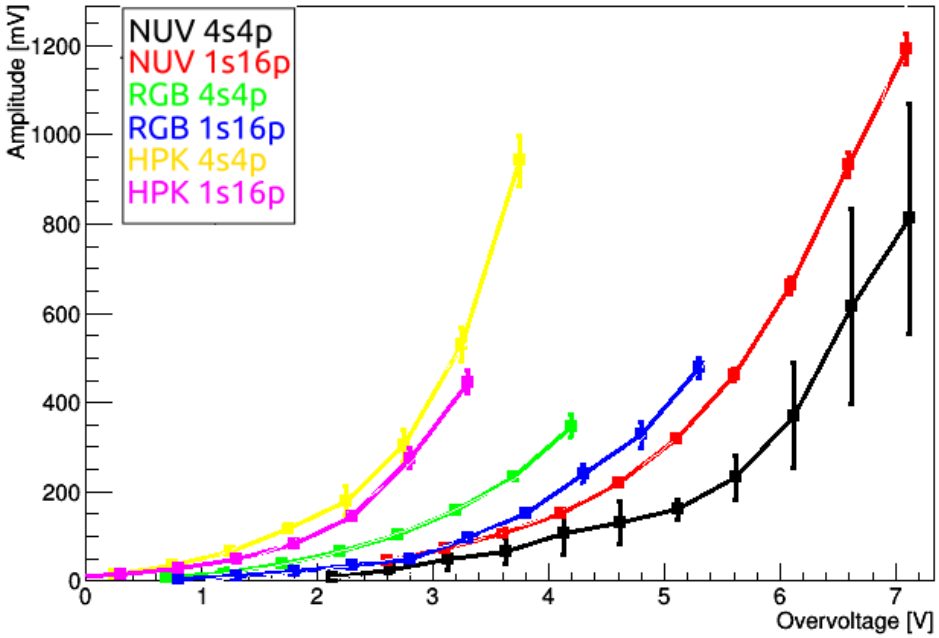

Figure 4.15: Amplitude of different arrays in different configurations as a function of overvoltage.

Table 4.5: Time performance of single arrays in different configurations at $V_{ov} = 3\ V$. The mean charge is the integral of the signal. The time resolution is the standard deviation of the temporal distance between the signals of the array and the photodiode.

	ASD-NUV3S-P		ASD-RGB3S-P	
	4s4p	1s16p	4s4p	1s16p
V_{bd} [V]	97.5	24.9	113.2	28.2
LeE [ns]	0.9 ± 0.5	7.5 ± 0.4	1.8 ± 0.2	8.0 ± 0.4
TrE [ns]	181 ± 2	741 ± 10	202 ± 3	927 ± 16
V_{max} [mV]	131 ± 49	152.7 ± 4.9	103 ± 5	50.1 ± 2.1
$\bar{Q}$ [pC]	332 ± 8	1226 ± 34	280 ± 8	642 ± 24
$\sigma\Delta t$ [ps]	10.4	878	25.6	95.3

	HPK s12572-050P	
	4s4p	1s16p
V_{bd} [V]	259	65.2
LeE [ns]	2.3 ± 0.4	4.7 ± 0.3
TrE [ns]	74.8 ± 3.8	572 ± 11
V_{max} [mV]	233 ± 41	144.4 ± 7.8
$\bar{Q}$ [pC]	198 ± 8	926 ± 42
$\sigma\Delta t$ [ps]	229	292

- 2S2P (equivalent to a 8s8p configuration);

- 4S1P (equivalent to a 16s4p configuration).

At this point of this thesis it is clear that all these configurations have some advantages and disadvantages: the 1S4P configuration has the lower bias voltage but the worst recovery time; on the contrary, the 4S1P configuration has the best performance but a working voltage around 1000 V. An alternative, in this case, can be used. By adding some passive components into the electrical connections between each array, it is possible to obtain an hybrid circuit with the advantages of both the series and parallel configurations. In figure 4.16 the hybrid circuit connections between four device is shown. The behavior of this circuit is easy to understand. Because of the bias voltage is a continuos voltage, the capacitors have "infinite impedance" and the path followed is shown in figure 4.17a. On the contrary, for the pulsed signals produced by photons, the path followed is shown in figure 4.17b. As clearly visible, from the pulse signal point of view the circuit is in series but for the bias it is in parallel. The biggest advantage of an hybrid configuration is the possibility to obtain a fast output signal by keeping the bias voltage low, thus increasing the total active area of a single readout channel of the device to 576 mm^2, corresponding to 64 commercial SiPMs of $3 \times 3\ mm^2$ each.

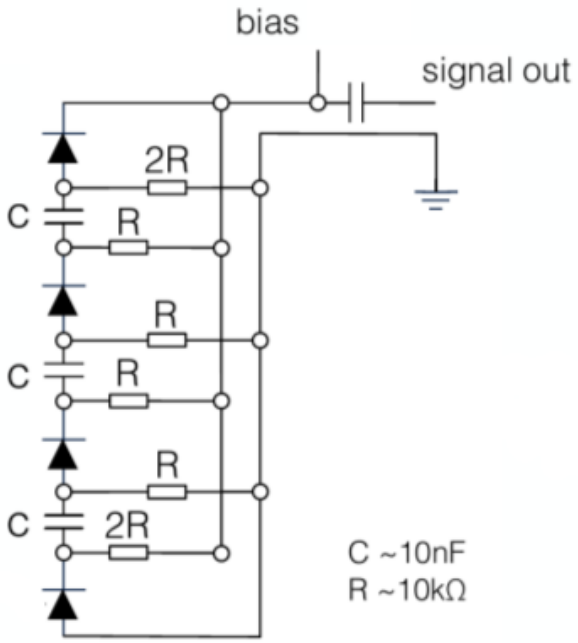

Figure 4.16: Hybrid circuit to connect four devices.

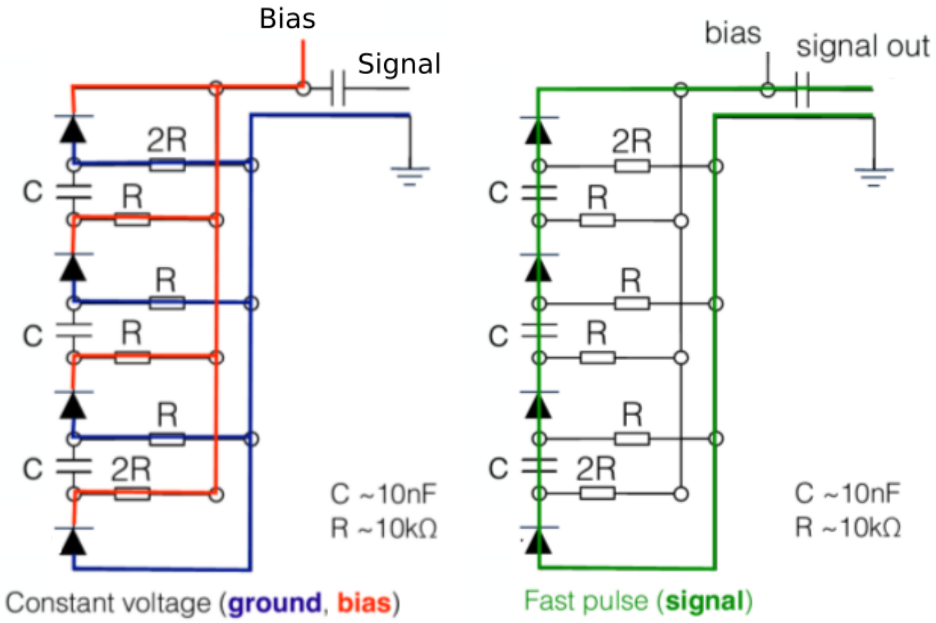

(a) (b)

Figure 4.17: Detailed view of the hybrid circuit in case of bias (a) and signal (b).

Table 4.6: Time performance of 4 Hamamatsu arrays in different configurations at $V_{ov} = 3\ V$.

	HPK S12572-050P		
Configuration	1S4P	2S2P	hybrid 4S1P
Breakdown Voltage [V]	259	519	259
Leading Edge [ns]	3.92 ± 1.20	2.75 ± 0.05	0.96 ± 0.02
Trailing Edge [ns]	152.7 ± 14.2	67.9 ± 0.7	54.2 ± 0.5
Amplitude [mV]	438 ± 26	486 ± 12	755 ± 3
Mean Charge [pC]	759 ± 19	366 ± 9	519 ± 5
Time resolution [ps]	814	327	15

4.5 Additional test in liquid argon

The new device, obtained by connecting four SiPMs arrays together, has one single cable for bias and signal. In this way the number of readout channel is drastically reduced with respect to the case of a system composed by single SiPMs. This device represents the final point to evaluate the capability of a system composed by single readout channel SiPMs arrays to work as photodetector in LAr-TPC. To evaluate the performance of this array, a series of tests both at room temperature and at 77 K were performed. Then, a couple of this devices were tested at CERN in liquid argon to compare the performance with the ICARUS PMTs.

4.5.1 Time features

To evaluate the time features of this array, the experimental apparatus described at the beginning of section 4.4 and shown in figure 4.13 has been adapted for this measurement. This test has been performed especially to study the behavior of the hybrid configuration of the electrical circuit. I compare the performance of different configurations:

- 1S4P;
- 2S2P;
- hybrid-4S1P.

In table 4.6 the performance of these three configurations, for Hamamatsu s12572 arrays, in terms of time features, amplitude and charge of signal are shown. It is important to underline that, in this case, the test performed with the hybrid configuration was made in a different time with respect to the other measurements, so, even if the amount of light is as similar as possible, small difference are presents. However, the main goal of this test is to show that, in general, the performance of the hybrid configuration are better then the "normal" ones. In particular, the time features of the signal is much better for the hybrid configuration. For this reason I choose to test the hybrid-4S1P

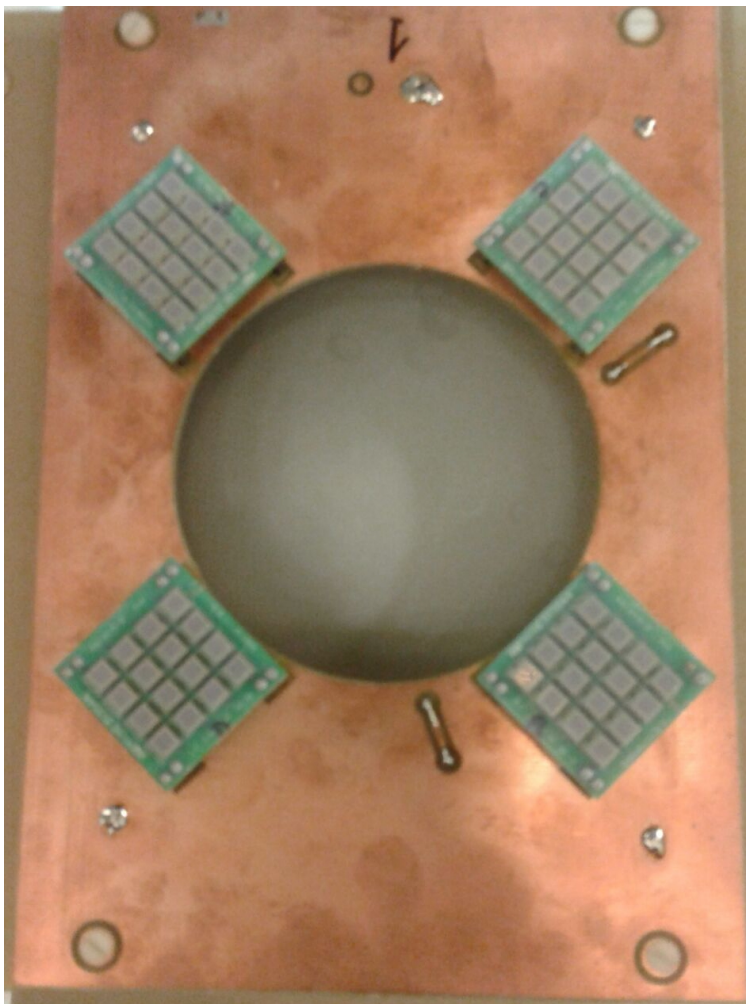

Figure 4.18: Photo of the SiPMs array placement around the hole in which the PMT active surface will be placed.

configuration in a liquid argon to compare its performance with a cryogenic PMT.

4.5.2 Comparison between the SiPMs arrays and the ICARUS PMTs

The last test I carried out, to evaluate the performance of a SiPMs array in liquid argon, is a direct comparison between this device and the PMT normally used into the LAr-TPC. For this reason I built up a setup at CERN composed of a big dewar of about 10 m^3 filled by liquid argon. The SiPMs array used for this test is composed by four SiPMs arrays (Hamamatsu s12572) placed as shown in figure 4.18 and connected with a hybrid-4S1P configuration. This particular SiPM arrays setup has been chosen to place the PMT at the center and keep all the devices as closest as possible from the each others. A cryo-

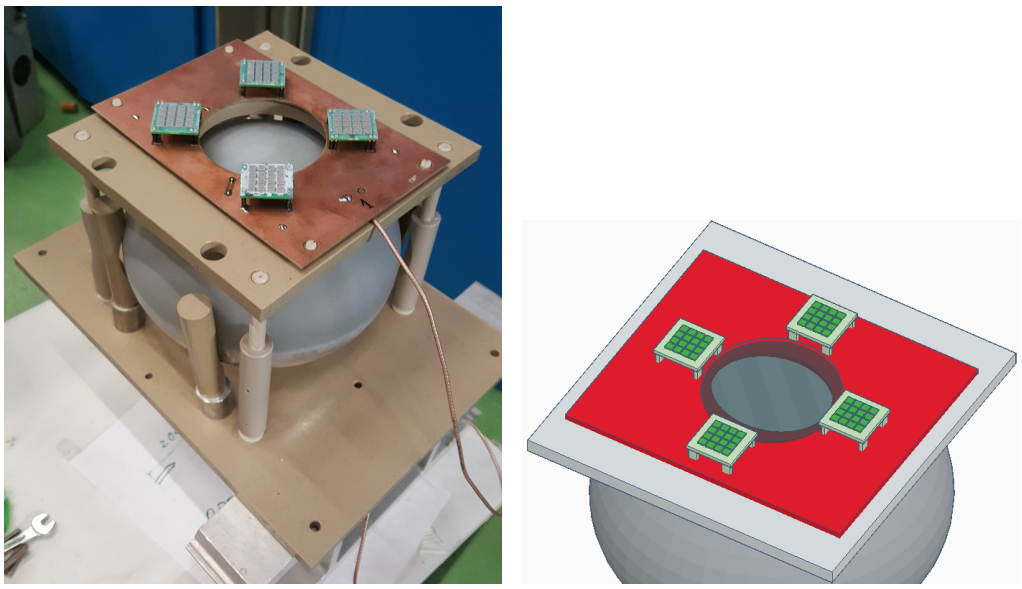

(a) (b)

Figure 4.19: Photo and drawing of one of the two identical modules composed by a SiPMs array and a PMT, for the test in LAr at CERN.

genic PMT model Hamamatsu R5912-mod, the same used by the ICARUS experiment for the SBN program at Fermilab, was placed behind the SiPMs support and fixed to a vetronite support as shown in figures 4.19. As it can be seen, the hole of a SiPMs array is smaller than the total PMT active area, in particular, with a diameter of 8 cm. This choice is due to a mechanical limitation of the PMT supports and it is useful to keep all the devices as closest as possible. Then, two of these modules are placed at the end caps of a column of 20×20 cm^2 cross section and 1 m high, completely immersed into the liquid argon bath. Two external plastic scintillator bars read by PMTs, placed outside the dewar as shown in figure 4.20, are used as a trigger for the cosmic rays. The two scintillator bars have an inclination of about 7 $^\circ$ with respect to the horizontal line. In this way, even if the rate of cosmic muons is small (around 0.5 Hz), the vertical spread of scintillation light produced into the active volume inside the column is strongly reduced and, as a consequence, also the time spread to detect that light is reduced. It is now clear the role of the column: reduce the active volume in which the scintillation light can be detected. Furthermore, I placed the scintillator bars in a such way that the middle of the muon tracks was 30 cm far from the bottom module for an event selection described in the following paragraph.

4.5.3 Data taking and results

The data acquisition system is very similar to the one used in the previous measurement performed at CERN and described in the section 4.3. In this case

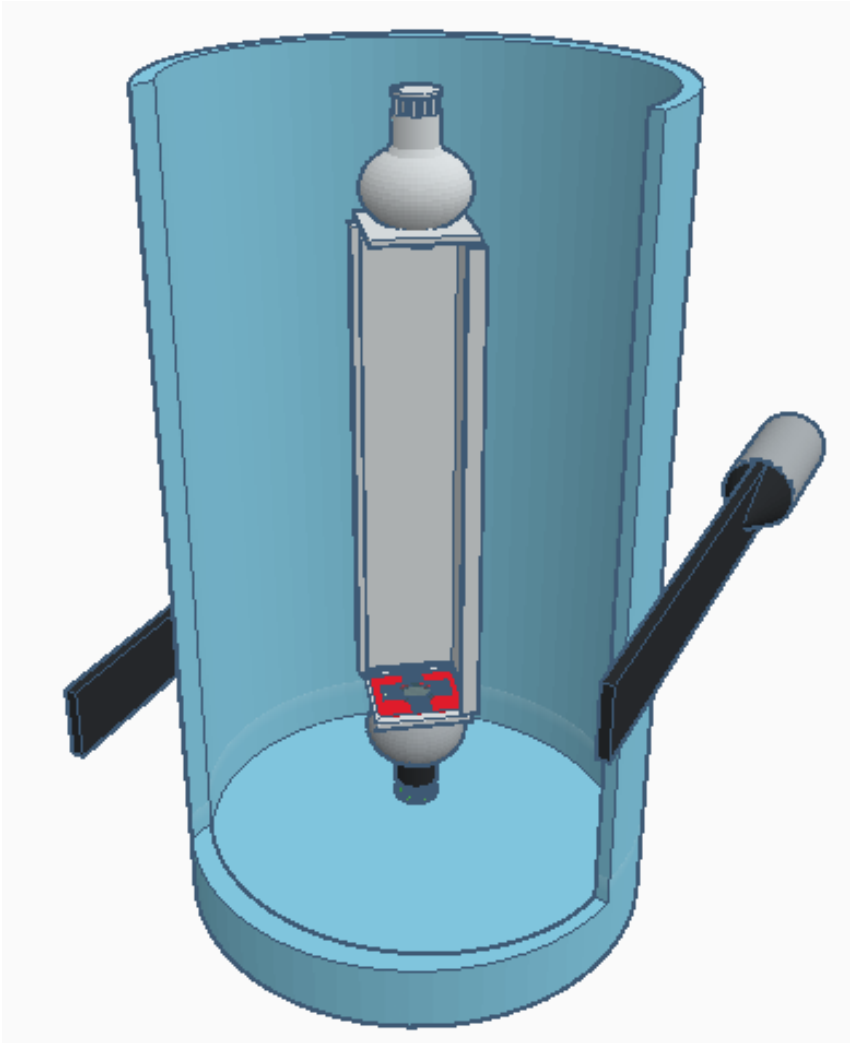

Figure 4.20: Drawing of the experimental setup for the test in LAr at CERN.

the SiPMs arrays are biased using two different picoammeters model Keythley 6487 that allow to record both the devices. The decoupling circuit and the PMT amplification chain is the same of the previous test and, in the PMTs case, it is the same that will be used for the SBN program at Fermilab. I started the data acquisition two days after the liquid argon filling to be sure that the PMTs gain became stable at 87 K. Furthermore, since the automatic liquid argon recirculation and purification systems were not present, I had to refill the dewar once a day; a level sensor was used to monitor the liquid argon level. The external scintillator bars were placed almost horizontal, as described before, to limit the vertical spread of liquid argon scintillation light. Furthermore, even if they could be moved on the vertical axis to change the coordinates of the interaction region of cosmic muons, I chose to keep them in positions for which the average interaction point was closer to the bottom module. In particular I placed the external scintillator bars in a way to have the interactions point at 30 cm far from the bottom module and, as a consequence, 70 cm from the top one. This choice has been done to reject the cosmic rays showers: when a shower occurs, it is possible that some secondary particles cross the scintillator bars concurrently, triggering the system. Of course, this situation has to be discarded because the particles tracks crossing the liquid argon are mainly vertical and the reconstruction of the correlation between the devices become hard to do. By placing the average interaction point closer to the bottom module I could reject all the events in which the signals of the top module is recorded before the bottom ones, thus rejecting almost all the cosmic ray showers. I compare the performance of the devices in terms of amplitude and time features, in particular for the leading edge, for each module. Even if the effective PMT active area has been reduced, as already described, for mechanical reasons, it is 8.7 times bigger then the SiPMs array. For this reason, to have the best comparison as possible, the amplitude is expressed for unit of area (in mm^2. In figure 4.21, two waveforms recorded with the PMT and the SiPMs array are shown. As visible, the main features are very similar, even if the SiPM recovery time is a bit longer. In figure 4.22 the comparison between the amplitudes of signals recorded event-by-event is shown. On the left the ratio between the SiPMs array and the PMT amplitudes for a unit of area for the top module is shown, on the right the same ratio for the bottom module. The average values of the ratios for the two modules, after a Gaussian fit of the data (the red lines in the figures), are $R_{top} = 3.8$ and $R_{bottom} = 2.7$. The difference between the two values is due to the different gain of the two PMTs. In fact, both the SiPMs arrays were biased at $V_{ov} = 4\ V$ and, because of the SiPM gain depends only on the overvoltage, the two SiPMs arrays had the same gain and thus the same amplitude. On the contrary, the two PMTs were both biased at 1500 V because of the voltage supply was the same, but had a different gain, because of the decrease fluctuation of the latter with the temperature. On the contrary, for what concern the leading edge (LE), we found that the value is the same for the detectors of each module. The average

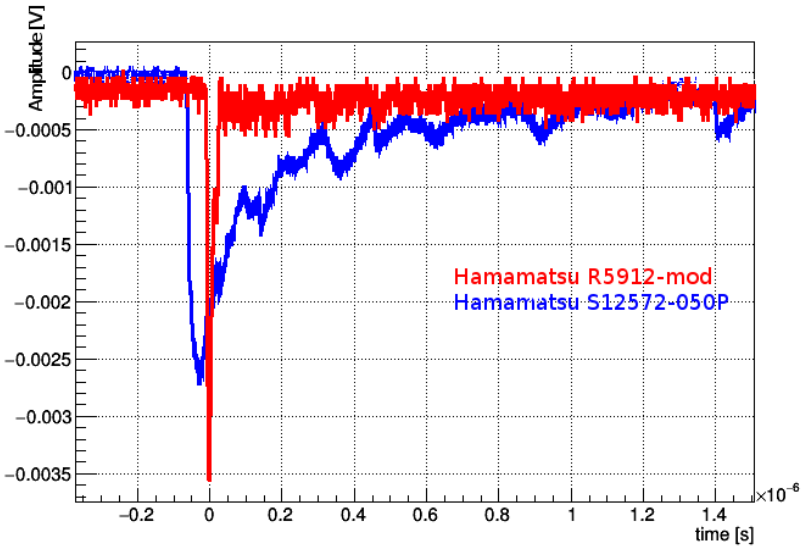

Figure 4.21: Comparison between the signals recorded with the PMT and the SiPMs array.

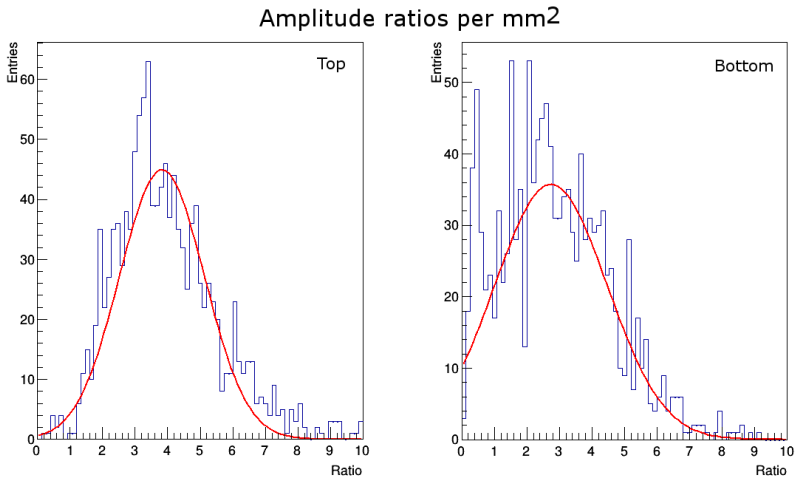

Figure 4.22: SiPMs array and PMT amplitude ratios for the top module (a) and the bottom module(b), calculated event by event. Gaussian fits are shown with the red lines.

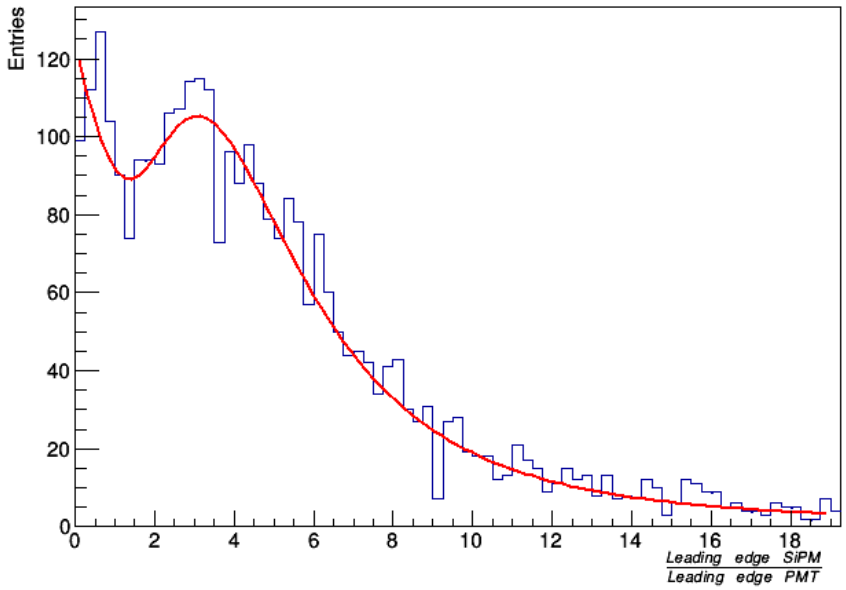

Figure 4.23: SiPMs array and PMT leading edges ratio of the two modules The red line a gaussian and exponential fit is shown.

ratio between the values is (figure 4.23)

$$\frac{SiPM_{LE}}{PMT_{LE}} = 3.9. \tag{4.4}$$

This means that the SiPMs arrays have a bit slower leading edge, even if the amplitude for unit of area is bigger with respect to the PMT one. From this test it is possible to conclude that the SiPMs arrays have the performance required by a scintillation light photodetector system in liquid argon. Future developments of this research can improve the performance, thus reaching the standard necessary for the future experiments.

Conclusions

The LAr-TPCs are, nowadays, one of the most interesting detectors to study the neutrino interactions and rare events physics phenomena, as, for example, the proton decay and dark matter. Thanks to the capability of these detectors to have a track reconstruction with high spacial resolution and high sensitivity, the main experimental programs devoted to this field of study are spending their resources on this technology. The Short Baseline Neutrino program (SBN) placed at Fermilab that is in the commissioning phase and, at the moment of the drafting of this thesis (summer 2018), the last missing detector, the ICARUS T600, has been put into its final placement, ready to start the data acquisition. Also future experiments, as the DUNE program (Deep underground Neutrino Experiment), a long baseline neutrino experiment programmed for the 2020's will use LAr-TPCs as detectors.

With this idea I started to study the possibility to replace the photodetectors usually used in LAr-TPCs, large area cryogenic PMTs, with a semiconductor-based photodetector with performance similar to the PMT ones. The SiPMs are the best choice for this, but because of their small active area they require lot of study. I chose to focus my research on the possibility to increase the active area, limiting the readout channels. I started testing some SiPM models to evaluate the performance, both at room and cryogenic temperatures, using a system able to make a full characterization as a function of the temperature (the cold head). I found that, as expected, the breakdown voltage of each device decreases with a typical temperature coefficient and that the working voltage is below 26 V for AdvanSiD devices and below 60 V for Hamamatsu ones. Furthermore, the gain, of the order of 10^6, does not change with temperature as for the PMTs, for which the gain at cryogenic temperature decreases of a factor 3 with respect to the room temperature value. The main problem is the noise that requires to work at low overvoltage to maintain low the dark counts.

After that I found which detectors can be used to develop a first series of arrays made by 16 SiPMs each: the AdvanSiD ASD-NUV3S-P, the AdvanSiD ASD-RGB3S-P and the Hamamatsu s12572-050P.
Furthermore, a study on the electrical configuration between each array has

been done to improve the array performance. This feature has played a fundamental role during my studies and it required more attention in comparison to the SiPM models. In fact, each configuration has different properties that affect the performance of the device. I built a matrix composed by 16 SiPMs with five different series/parallel configurations.

Thanks to the possibility to make tests at CERN, I could evaluate the performance of SiPMs arrays in almost-real experimental conditions. To do that, I placed the arrays into a small LAr-TPC and I recorded few cosmic rays events. The analysis of the results allow to confirm that the different configurations play a fundamental role for the performance of the device. So, I studied in detail the different configurations, especially in terms of leading edge of signal which is of few ns.
In the end, to increase again the active area I tried to use an hybrid circuit allowing to have the best performance as possible. This hybrid configuration, as described, consist in a particular combination of resistors and capacitors added to the circuit used to connect different arrays to obtain the performance of a series connection keeping low the working voltage.

I concluded the series of tests at CERN, with a direct comparison between the SiPMs arrays and the cryogenic PMTs which will use in the ICARUS LAr-TPCs.
From this test I found that, in terms of amplitude the SiPMs arrays have signals higher with respect to the PMTs in the same working conditions. However the time performance, especially for the leading edge, require more studies, even if the values found are of the same order of magnitude (the leading edge of the SiPMs array is 3 times the PMT one).

In conclusion, the results I obtained during my research allow to affirm that the idea to use a SiPMs array with common bias and readout to reduce as much as possible the readout channels and to increase the total active area, can play a fundamental role in the photodetector systems development for LAr-TPCs for the next generation experiments.

Bibliography

[1] S. L. Glashow, Nucl. Phys. 22, 579 (1961).

[2] S. Weinberg, Phys. Rev. Lett. 19, 1264 (1967).

[3] A. Salam, *Proc. of the 8 th Nobel Symposium on Elementary particle theory, relativistic groups and analyticity*, Stockholm, Sweden, 1968, edited by N. Svartholm, p.367-377, (1969).

[4] C.Giunti, C.W.Kim, Fundamentals of neutrino physics and astrophysics, 2007.

[5] B. Pontecorvo, Sov. Phys. JETP 6, 429 (1958). Sov. Phys JETP 7, 172 (1958).

[6] S. M. Bilenky and B. Pontecorvo, Sov. J. Nucl. Phys., 24, 316âĂŞ319 (1976).

[7] S. M. Bilenky and B. Pontecorvo, Phys. Rep., 41, 225 (1978).

[8] S. M. Bilenky and B. Pontecorvo, Nuovo Cim. Lett., 17, 569 (1976).

[9] S. Eliezer and A. R. Swift, Nucl. Phys., B105, 45 (1976).

[10] H. Fritzsch and P. Minkowski, Phys. Lett., B62, 72 (1976).

[11] C. Patrignani et al. (Particle Data Group), Chinese Physics C, 40, 100001 (2016).

[12] A. Falcone *Studies and tests for the new light collection system of the ICARUS T600 detector* PhD thesis - University of Pavia, Pavia, Italy, November 2015.

[13] L. Wolfenstein. Neutrino oscillations in matter. Phys. Rev. D, 17:2369-2374, May 1978.

[14] S.P. Mikheev and A. Yu. Smirnov. Resonant amplification of neutrino oscillations in matter and solar neutrino spectroscopy. Nuovo Cim., C9:17âĂŞ26, 1986.

[15] C. Rubbia. *The liquid argon time projection chamber: A new concept for neutrino detectors.* 1977. CERN-EP-INT-77-08.

[16] P. Cennini et al. (ICARUS Collaboration), Nucl. Instr. and Meth. A, 345, 230 (1994).

[17] F. Arneodo et al. (ICARUS Collaboration), Nucl. Instr. and Meth. A, 449, 36 (2000).

[18] P. Cennini et al. (ICARUS Collaboration), Nucl. Instr. and Meth. A, 432, 240 (1999).

[19] F. Arneodo et al. (ICARUS Collaboration), Nucl. Instr. and Meth. A, 498, 293 (2003).

[20] C. Rubbia et al. (ICARUS Collaboration), JINST 6 P07011 (2011).

[21] P. Benetti et al. (ICARUS Collaboration), Nucl. Instr. and Meth. A, 332,395 (1993).

[22] Benetti, P. et al.; Nucl. Instr. and Meth. A574 (2007), 83.

[23] Leo, W.R.; Techniques for Nuclear and Particle Physics Experiments (1987).

[24] Lindhard, J. et al.; Mat. Fys. Medd. Dan. Vid. Selsk. 33, n. 10 (1963).

[25] Lindhard, J. et al.; Mat. Fys. Medd. Dan. Vid. Selsk. 33, n. 14 (1963).

[26] S. Kubota et al., Phys. Rev. B , 20, 3486 (1979).

[27] T. Doke et al., Nucl. Instr. and Meth. A, 291, 617 (1990).

[28] M. Suzuki et al., Nucl. Instr. and Meth. A, 327, 67 (1993).

[29] S. Kubota et al., 1978, Phys. Rev. B , 17, 2762 (1978).

[30] S. Amoruso et al. (ICARUS Collaboration), Nucl. Instr. and Meth. A, 523, 275 (2004).

[31] C. Amsler et al., JINST, 3, P02001 (2008).

[32] A. Zani, Advances in High Energy Physics, 2014, 205107, (2014).

[33] C. Rubbia et al. *Searching for short baseline anomalies with the LAr-TPC detector at shallow dephts*, arXiv:1408.6431.

[34] C. Athanassopoulos et al. (LSND Collaboration), Nucl. Instrum. and Meth. A, 388, 149 (1997).

[35] A. Aguilar et al. (LSND Collaboration), Phys. Rev. D 64, 112007 (2001).

[36] G. Drexlin et al. (KARMEN Collaboration), Nucl. Instrum. and Meth. A, 289, 490 (1990).

[37] B. Armbruster et al. (KARMEN Collaboration), Phys.Rev. D65, 112001 (2002).

[38] A. Aguilar-Arevalo et al. (MiniBooNE Collaboration), Nucl. Instr. and Meth. A, 599, 28 (2009).

[39] A. Aguilar-Arevalo et al. (MiniBooNE Collaboration), Phys.Rev.Lett. 102, 101802 (2009).

[40] A. Aguilar-Arevalo et al. (MiniBooNE Collaboration), Phys.Rev.Lett. 105, 181801 (2010).

[41] W. Hampel et al. (GALLEX Collaboration), Phys.Lett. B420, 114 (1998).

[42] J. Abdurashitov et al. (SAGE Collaboration), Phys.Rev. C59, 2246 (1999).

[43] C. Giunti and M. Laveder, Phys.Rev. C83, 065504 (2011).

[44] K. Nakamura et al. (Particle Data Group), J.Phys.G G37, 075021 (2010).

[45] T. Mueller et al., Phys.Rev. C83, 054615 (2011).

[46] G. Mention et al., Phys.Rev. D83, 073006 (2011).

[47] Gariazzo, S. et al., Light sterile neutrinos, arXiv:1507.08204v1.

[48] R. Acciari et al., A Proposal for a Three Detector Short-Baseline Neutrino Oscillation Program in the Fermilab Booster Neutrino Beam, arXiv:1503.01520.

[49] A. Falcone et al. *Comparison between large area photo-multiplier tubes at cryogenic temperature for neutrino and rare event physics experiments*, Nucl. Instr. and Meth. A787, 55-58 (2015).

[50] X. Berlman, *Handbook of Fluorescence Spectra of Aromatic Molecules*, Academic Press, New York (1965).

[51] M. Bonesini et al. *Realization of a high vacuum evaporation system for wave-length shifter deposition on photo-detector windows*, Journal of Vacuum Science & Technology B 36, 01A101 (2018).

[52] M. Bonesini et al., *An innovative technique for TPB deposition on convex window photomultiplier tubes*, arXiv:1807.07123 submitted to JINST.

[53] P. Benetti et al. (ICARUS Collaboration), Nucl. Instr. and Meth. A, 505, 89 (2003).

[54] R. B. Darling, *Micro Fabrication Photolithography*, EE-527, pp 1.31.

[55] W. M. Burton et al., *Fluorescence of Tetraphenyl-Butadiene in the Vacuum Ultraviolet*, Applied Optics Vol 12, No. 1 (1973).

[56] A.Ankowski et al., Characterization of ETL 9357FLA photomultiplier tubes for cryogenic temperature applications, Nucl. Instrum. and Meth. A 556 (2006) 146-157.

[57] H.O.Mayer, Dark rate of a photomultiplier at cryogenic temperatures, [arXiv:0805.0771v1 (nucl-ex)].

[58] D. Renker, *Geiger-mode avalanche photodiodes, history, properties and problems*, Nucl. Instr. and Meth. A 567 (2006) 48âĂŞ56.

[59] F. Zappa, et al., ESSCIRC (2002).

[60] P.P. Antich, et al., Nucl. Instr. and Meth. A 389 (1997) 491.

[61] V. Saveliev, V. Golovin, Nucl. Instr. and Meth. A 442 (2000) 223.

[62] S.M. Sze. Physics of Semiconductor Devices. Wiley, 1969.

[63] W. Shockley and W. T. Read. Statistics of the recombinations of holes and electrons. Phys. Rev., 87:835âĂŞ842, Sep 1952.

[64] V. Chmill et. al., *Study of the breakdown voltage of SiPMs*, Nucl.Instrum.Meth. A845 (2017) 56-59.

[65] G.L. Raselli et. al., 2016 IEEE Nuclear Science Symposium, Medical Imaging Conference and Room-Temperature Semiconductor Detector Workshop (NSS/MIC/RTSD).

[66] G.A.M. Hurkx et al., A new recombination model for device simulation including tunneling , IEEE Trans. Electron. Dev. 39 (1992) 331.

[67] G.A.M. Hurkx et al., A new analytical diode model including tunneling and avalanche breakdown, IEEE Trans. Electron. Dev. 39 (1992) 2090.

[68] C.Piemonte et. al. *Recent Developments on Silicon Photomultipliers produced at FBK-irst*, 2007 IEEE Nuclear Science Symposium Conference Record.

[69] C.Piemonte et. al. *Development of an automatic procedure for the characterization of silicon photomultipliers*, 2012 IEEE Nuclear Science Symposiwn and Medical Imaging Conference Record (NS S/MIC).

[70] M. De Gerone et al., *Development and commissioning of the Timing Counter for the MEG Experiment*, IEEE Trans. Nucl. Sci. 59 (2012) 379, arXiv:1112.0110.

[71] M. De Gerone, F. Gatti, W. Ootani, Y. Uchiyama, M. Nishimura, S. Shirabe et al., *Design and test of an extremely high resolution Timing Counter for the MEG II experiment: preliminary results*, 2014 JINST 9 C02035 [arXiv:1312.0871].

[72] M. De Gerone et al., *A high resolution Timing Counter for the MEG II experiment*, Nucl. Instrum. Meth. A 824 (2016) 92.

[73] D. Alloni et al., *Neutron flux characterization of the SM1 sub-critical multiplying complex of the Pavia University*, Prog. Nucl. Energ. 67 (2013) 98.

[74] M.E. Anderson and W.H. Bond Jr., *Neutron spectrum of a plutonium-beryllium source*, Nucl. Phys. 43 (1963) 330.

[75] http://www.rist.or.jp/rsicc/app/sand_2.htm.

[76] Hamamatsu S12572 datasheet, www.hamamatsu.com

[77] AdvanSiD ASD-NUV3S-P datasheet, http://www.hamamatsu.com

[78] AdvanSiD ASD-RGB3S-P datasheet, http://advansid.com